NANO-STRUCTURES FORMATION ON InP(111) SEMICONDUCTOR SURFACES BY ION BEAM IRRADIATION

A THESIS SUBMITTED TO THE

HOMI BHABHA NATIONAL INSTITUTE

FOR THE DEGREE OF

DOCTOR OF PHILOSOPHY IN SCIENCE

(PHYSICS)

By

DIPAK PARAMANIK

INSTITUTE OF PHYSICS,

BHUBANESWAR 751 005, INDIA.

JULY, 2008

CERTIFICATE

This is to certify that the thesis entitled **Nano-structures formation on InP(111) semiconductor surfaces by ion beam irradiation** which is being submitted by *Dipak Paramanik* in fulfillment of the degree of **Doctor of Philosophy** of the **Homi Bhabha National Institute (HBNI), India** is a record of the research work, carried out by him under the guidance of *Prof. Shikha Varma* at the *Institute of Physics, Bhubaneswar*, since July 2003. To the best of our knowledge, the results presented in this thesis have not been submitted by anybody for the award of any other degree.

Signature of the candidate	Signature of the supervisor
(Dipak Paramanik)	(Prof. Shikha Varma)

To My Parents

Acknowledgements

It gives me a great pleasure to place on record my indebtedness to my thesis adviser Prof. Shikha Varma. During the last 5 years of my Ph.D. studies, it was Prof. Varma who inspired me to look deeper into details of each problem and taught me the way of approaching new physics problems and to realize the beauty of scientific research and sharpen my scientific temper. I feel privileged to have worked under such an enthusiastic and capable scientist, teacher and mentor. Her encouraging statement ” *Don’t tell me the problem, tell me the solution* ” ever enlivened my zeal during the hardest time of my career. I am most thankful to her for giving me total freedom in my academic and social life.

I must thank the people in our group Dr. Soma Dey, Mr. Santosh Choudhury, Mr. Subrata Majumdar, Mr. Smruti Ranjan Sahoo and Dr. M.V. R. Rama Rao. They have been great colleagues and friends, and our discussions have been interesting and fruitful. They have helped me in numerous ways both in and out of the laboratory.

During the course of my research work I had the opportunity to collaborate with Prof. Asima Pradhan, Prof. S. N. Sahu, Prof. A.K. Pal, Prof. C. Jacob, Prof. T. Som, Prof. K. K Nanda, Dr. Jhashaketan Nayak, Dr. Satchidananda Ratha and Dr. S. N. Sarangi. Thanks to all of them for many fruitful discussions.

I thank all the faculty members of the Institute from whom I have benefited in some way or the other.

A special thanks is due to Prof. Ajit Mohan Srivastava for his help and encouragement and of course for all his great dinners.

I wish to acknowledge the timely help provided by the technical staffs in the ion

beam laboratory.

I would like to thank the library and administrative staff for their timely support.

Thanks to all my friends in the Institute for having made my stay in the Institute a memorable one.

I would also like to thank my all the teachers from School to University who have helped me in many ways to reach upto this stage.

Finally and most importantly, it goes without saying that this work would have been impossible without the support, encouragement and affection of my mother Mrs. Shashikala Paramanik, brother Mr. Bhisam Paramanik and sister Mrs. Chandana Paramanik, my uncles and other family members. It is their unflinching faith in me that has led me to deliver my best.

Date : (Dipak Paramanik)

List of Publications/Preprints

Published and communicated in journals:

***[1]** Morphological evolution of InP nano-dots and surface modifications after keV irradiation,
D. Paramanik, S.N. Sahu and S. Varma, *J. Phys. D: Appl. Phys.***41***, 125308 (2008)*

***[2]** Scaling Studies of Nano-dots on InP(111) Surfaces after MeV Implantation,
D. Paramanik, and S. Varma, *J. Nanosci. and Nanotech.(in press)*

[3] High temperature grown transition metal oxide thin films: tuning physical properties by MeV N^+ ion bombardment, R. Sivakumar, C. Sanjeeviraja, M. Jayachandran, R. Gopalakrishnan, S.N. Sarangi, D. Paramanik, and T. Som, *J. Phys. D: Appl. Phys.***41***, 125704 (2008)*

***[4]** Studies of InP nano dots formation after keV Ar+ irradiation,
D. Paramanik, and S. Varma, *Nucl. Inst. and Meth.B* **266***, 1257 (2008)*

[5] Boron phosphide films prepared by co-evaporation technique: synthesis and characterization,
S. Dalui, S. Hussain, D.Paramanik, S. Varma and A. K. Pal, *Thin Solid Films* **515***, 4958 (2008)*

*[**6**] Studies of self-organized Nanostructures on InP(111) surfaces after low energy Ar^+ ion irradiation,
D. Paramanik, S. Majumdar, S.R. Sahoo and S. Varma, *J. Nanosci. and Nanotech.(in press)*

[**7**] Temperature dependent changes in structural and magnetic properties of heavy ion irradiated nanoscale Co/Pt multilayer,
T. Som, S.Ghosh, M. Mader, R. Grotzschel, S. Roy, D. Paramanik, A. Gupta, *New. J. Phys.* **9**,*164 (2007)*

[**8**] BSb films: Synthesis and Characterization, A.K. Pal, S. Dalui, S. N. Das, S. Hussain,
D. Paramanik, S. Varma.,*J. Crys. Growth.***305**, *149 (2007)*

*[**9**] Raman Scattering Characterization and Electron Phonon Coupling Strength for MeV implanted InP(111),
Dipak Paramanik and Shikha Varma, *J. Appl. Phys.* **101**,*023528 (2007).*

[**10**] MeV N^+ -ion irradiation effects on alpha-MoO_3 thin films, R. Sivakumar, C. Sanjeeviraja, M. Jayachandran, R. Gopalakrishna, S.N. Sarangi, D. Paramanik, and T. Som, *J. Appl. Phys.***101**,*034913 (2007).*

[**11**] Formation of gold nanoparticles in ploymethylemethacrylate by UV irradiation, Mazid Kazemian Abyaneh, D. Paramanik, S. Varma, S.W. Gosavi, and S.K. Kulkarni. *J. Phys. D: Appl Phys.* **40**,*3771 (2007).*

*[**12**] Raman Scattering Studies of InP nanostructures created by MeV Sb ion Implantation,
Dipak Paramanik and Shikha Varma, *J. Nanosci. and Nanotech.* **07**, *2197 (2007).*

[**13**] Modification of WO_3 thin films by MeV N^+ion beam irradiation,
R. Sivakumar, C. Sanjeeviraja, M. Jayachandran, R. Gopalakrishna, S.N. Sarangi,

D. Paramanik, and T. Som, *J. Phys: Condens. Matter* **19** *186204 (2007).*

***[14]** Nanoscale Defect Formation on InP(111) Surfaces after MeV Sb Implantation, Dipak Paramanik, Asima Pradhan and Shikha Varma, *J. Appl. Phys.* **99**, *014304(2006).*

***[15]** Pattern Formation on InP(111) surfaces after Ion Implantation, Dipak Paramanik and Shikha Varma, *Nucl. Instr. Meth. B.* **244**, *69 (2006).*

***[16]** Surface Roughening and Radial Separation Distribution Studies on InP(111) Surfaces after MeV Sb^{2+} Implantation,
Dipak Paramanik and Shikha Varma, *Nucl. Instr. Meth. B.* **244**, *81 (2006).*

[17] Shape Transition of Nanostructures created on Si(100) surfaces after MeV Implantation,
D. Paramanik , S.Dey, V. Ganesan and S. Varma, *Nucl. Instr. Meth. B.* **244**, *74 (2006).*

[18] Surface characterization and electronic structure of HgTe nanocrystalline thin films. S. Rath, D. Paramanik, S. N. Sarangi, S. Varma, and S. N. Sahu, *Phys. Rev. B* **72**, *205410 (2005).*

[19] Formation and shape transition of nanostructures on Si(100) surfaces after MeV Sb implantation,
Soma Dey, Dipak Paramanik, V.Ganesan and Shikha Varma, *Appl. Surf. Sci.* **253** , *1116 (2006).*

[20] High frequency characterization and continuum modeling of ultrathin high-k ZrO_2 gate dielectrics on strained-Si, M.K. Bera, S. Chakraborty, S. Saha, D. Paramanik, S. Varma, S. Bhattacharya and C.K. Maiti, *Thin Solid Films,* **504**, *183 (2006).*

[21] Leakage current characteristics and energy band diagram of $Al/ZrO_2/Si_{0.3}Ge_{0.7}$ hetero-MIS structures,
S. chakraborty, M.K. Bera, G.K Dalapati, D. Paramanik, S. Varma, P.K. Bose, S. Bhattacharya and C.K. Maiti, *Semicond. Sci. Technol.* **21***, 467, (2006).*

[22] Composition and Optical Characteristics of Electrochemically Synthesized GaAs Nanocrystals,
J. Nayak, S. Varma, D. Paramanik and S. N. Sahu, *Int. J. Nanosci.* **281***, 3(2004)*

[23] CVD growth and characterization of 3C-SiC thin films,
A Gupta, D. Paramanik, S. Varma and C Jacob, *Bull. Mater. Sci,* **27***, 445 (2004).*

Conference proceedings:

***[1]** Time evolution of Nano-dots on InP(111) surfaces by 3 keV Ar ion Sputtering,
D. Paramanik, S.Mazumdar, S.R. Sahoo and S. Varma, *Mat. Res. Soc. Symp. Proc.* **1020***,GG04 (2007)*

***[2]** Developing Nano-patterns on InP(111) surfaces after keV irradiation, S.Majumder, Dipak Paramanik, S.R.Sahoo , Shikha Varma, *DAE Solid State Physics Symposium,*
December 26-31,2006, Barkatullah University, Bhopal, India.

***[3]** Formation and distribution of nano-structure on InP(111) surfaces due to 1.5 MeV Sb^{2+} ion implantation,
Dipak Paramanik and Shikha Varma, *International conference on Optoelectronic Materials and Thin films for Advanced Technology, October 24-27, 2005, Cochin University, Kerala, India.*

*[**4**] SPM study of ion implantation induced nanostructures on InP(111) surfaces,
D. Paramanik and S. Varma, *Solid State Physics 50, 257 (2005), DAE Solid State Physics Symposium, December 5-9, 2005, Bhaba Atomic research Center, Mumbai, India.*

[**5**] Temperature dependence of interface properties and conduction mechanism of ultrathin high-k ZrO_2 gate dielectrics deposited on strained Si/Si-Ge hetero layers,
M.K. Bera, S. Chakraborty, S. Saha, D. Paramanik, S.Varma, S. Bhattacharya and C.K. Maiti, *International Conference on Electronic and Photonic Materials, Devices and Systems, January 4-6, 2006, University of Calcutta, Kolkata, India.*

*[**6**] Evolution of Surface Structures and Surface Roughness after of InP(111) after MeV implantation,
D.Paramanik and S. Varma, *DAE Solid State Physics Symposium, December 26-31, 2004, Guru Nanak Dev University, Amritsar, India.*

*[**7**] Nanoscale Structure formation on InP(111) surfaces after MeV Implantation,
Dipak Paramanik and Shikha Varma, *International Symposium on Advanced Material and Processing, December 6-8, 2004, Indian Institute of Technology, Kharagpur, India.*

*[**8**] Surface studies on InP(111) after MeV implantation,
Dipak Paramanik and Shikha Varma, *Indo-US Workshop on Nano-Scale Materials: From Science To Technology, April 5-8, 2004, Puri, India, NOVA publications, pp-232, NY, USA.*

(*) indicates papers on which this thesis is based.

Synopsis

With the fast growing interest in nanotechnology, fabrication of regular arrays of semiconductor nanostructures with controlled size and height is of great importance. These nanoscale pattern hold promise in applications as varied as optical devices, templates for liquid crystal orientation, and strain-free patterned substrates for hetero-epitaxial growth of quantum dots or wires. Fabrication of nano-dots through self-organization, induced by ion irradiation processes, has attracted special interest due to the possibility of production of regular arrays of dots on large areas in a single technological step. The pattern formation occurs due to the competition between curvature dependant ion sputtering that roughens the surface and its smoothening by different relaxation mechanisms.

During this patterning, however, along with nano dot fabrication the surface also undergoes structural modifications due to ion irradiation. Although these surface modifications have not received much attention, they are important for understanding the parameters influencing the formation of nano-dots as well as their evolution. Ion irradiation can, however, also lead to modifications in the nature of the surface as well as its stoichiometry which can effect the self assembly crucially.

In this thesis, I present the results of investigations on the formation of nanostructures on InP(111) surfaces after low energy (3 keV) Ar ion irradiation and high energy (1.5 MeV) Sb ion irradiation. The thesis discusses the formation of nano-dots, their evolution as a function of fluence, their size and height distributions, related surface modifications as well as the surface exponents. I have primarily utilized the techniques of Scanning Probe Microscopy (SPM), Raman scattering and X-ray Photoelectron Spectroscopy (XPS) for these measurements.

In the first part of the thesis, a detailed investigation on the temporal evolution and the coarsening behaviour of InP nano dots in conjunction with the structural modifications occurring on the InP(111) surface have been presented. The dots have been fabricated by 3 keV Ar^+ ion sputtering under off-normal geometry but in the absence of rotation. These nano-structures are produced over a wide temporal range of sputtering time spanning from 5 min to 80 min, with a low ion flux of 1×10^{13} $ions\ cm^{-2}\ s^{-1}$. A detailed investigation of these nano-structures has been done by SPM. The average size and height of the nano-structures varies in the range of 10 to 100 nm and 5 to 40 nm, respectively, for different sputtering times. A high density of nano-dots, with narrow size and height distributions, is found for 10 minutes of sputtering. These nano-dots exhibit a weak short range ordering. The nano-structures develop in the early stages of sputtering and coarsen in size and height with increasing time upto a critical time (t_c). Beyond t_c (= 40 min), however, an inverse coarsening and fragmentation of the nano-dots is seen. During this nano dot formation, by ion beam irradiation, the surface undergoes several modifications. The value of rms surface roughness increases upto t_c but decreases for longer sputtering durations. To understand the nature of the surface modifications and to compare these observations with the existing theoretical models, roughness exponent (α) and the growth exponent (β) have been measured using SPM images. Raman Scattering results show that during the coarsening of nano-dots, in addition to other modifications, the surface also experiences an increased tensile stress. For higher sputtering durations, surface amorphization is observed. This leads to the inverse-coarsening and fragmentation of the dots. Consequently, relaxation in the stress, by Raman scattering results, as well as smoothening of surface, by SPM technique, are observed.

The technique of X-ray Photoelectron Spectroscopy (XPS) has been utilized to understand the chemical stoichiometric modifications occurring on the InP surfaces during 3 keV ion irradiation. Results show the shift of In(3d)and P(2p) core levels towards the higher binding energy. These shifts have been related to the nano-dots formation. Moreover, an excess In concentration compared to P atoms is also seen for 10 min of sputtering. This leads to In -rich zones on the surface. These In- rich zones act as nucleation sites for the formation of nano-dots on the surface. The decrease in In/P ratio at higher sputtering durations causes the fragmentation of the nano-dots.

In the second part of the thesis, investigations have been made to understand the surface modifications, formation of nano-structures and their evolution as a function of ion fluence after 1.5 MeV Sb^+ ion implantation. These implantations, with the fluences varying from $1 \times 10^{11}\ ions/cm^2$ to $1 \times 10^{15}\ ions/cm^2$, were carried out by utilizing the 3 MV tandem pelletron facility at Institute of Physics, Bhubaneswar. After implantation, several nano-structures, related to the damage on the InP(111) surface have been observed. Morphology of the ion irradiated InP(111)surfaces, the height and size distributions of nano-structures and their evolution have been investigated by SPM. SPM images have been utilized to investigate rms surface roughness, Power Spectral Density (PSD), radial separation distribution, the growth exponent and the roughness exponent. The rms roughness of InP(111) surfaces show two behaviors as a function of ion fluence. Although rms roughness increases upto a critical fluence it decreases for higher fluences. Raman scattering results show that the InP surface undergoes a crystalline/amorphous transition at the critical fluence. PSD analysis of the ion beam modified surfaces demonstrate that the diffusion processes lead to surface smoothening at high ion fluences. Radial separation distributions of the nano-structures display a scaling behavior and further show that the nanostructures are not uniformly distributed but exhibit clustering at $r \approx \langle R \rangle$ where$\langle R \rangle$ is the average separation between the nano-structures.

During implantation, the lattice atoms are displaced, creating defects, and disordered regions in the process. With increasing lattice disorder, the phonon coherence length is reduced and k = 0 selection rule is relaxed, giving rise to measurable shifts and asymmetric broadening of the Raman peaks. The first and second order Raman scattering phonon spectra have been utilized to investigate the lattice modifications in InP(111) substrate after implantation with 1.5 MeV Sb^{2+} ions. The evolution of both transverse optical (TO) and longitudinal optical (LO) modes as a function of ion fluence were analyzed. At the fluence of $1{\times}10^{11}$ $ions/cm^2$, modifications in first order as well as second order modes demonstrate the initiation of some damage in InP(111) lattice. Once this occurs, a coexistence of nanocrystalline regions and amorphous zones is observed which leads to the confinement of phonons. An estimation of the phonon coherence length has been done by applying the Phonon Confinement Model (PCM) to the first order Raman peak. Existence of a completely amorphous lattice is noticed for a fluences of $1{\times}10^{14} ions/cm^2$ and higher. The evolution of LO-phonon plasmon coupled (LOPC) mode, L^-, has also been studied as a function of ion fluence. The effect of implantation on the electron phonon coupling in InP(111) by utilizing the second order Raman modes were also investigated here. It was found that the strength of coupling reduces as the size of nano-crystalline zones, in the implanted lattice, decrease.

Thus, in this thesis the patterning of InP(111) surfaces, has been carried out by low energy(3 keV) and high energy(1.5 MeV) ions. The formation and evolution of the nano-structures have been investigated as a function ion fluence. The related surface modifications have also been studied here.

The thesis is organised in six chapters. Chapter-1 provides a brief introduction on the mechanism of ion-solid interactions and the pattern formation on InP(111) surfaces after ion irradiation. Chapter-2 describes the experimental techniques utilized during the course of investigations presented in this thesis. The main results of the thesis are presented in chapter 3-5. The formation and evolution of nano-dots created on InP(111) surfaces via 3 keV Ar ion irradiation are discussed in chapter-3. The modifications to the surface, variations in surface roughness, the related exponents etc., after keV irradiation, are also discussed in this chapter. Chapter-4 discusses the patterning of InP(111) surfaces after MeV irradiation. The evolution of nano-structures, the modification of the surface and the scaling exponent, after MeV irradiation, are also discussed here. The lattice modification in InP(111), after MeV irradiation have been studied in chapter-5 by utilizing the first and second order Raman scattering phonon spectra. Chapter-6 is the summary of all the results presented in this thesis.

Contents

CERTIFICATE **ii**

Acknowledgements **iv**

List of Publications/Preprints **vi**

Synopsis **xi**

1 Introduction **1**

- 1.1 Introduction 1
  - 1.1.1 Basics of Ion-Solid interaction 4
  - 1.1.2 Nuclear Energy loss 6
  - 1.1.3 Electronic Energy loss 8
  - 1.1.4 Ion Range 10
  - 1.1.5 Implantation 10
  - 1.1.6 Surface Modification due to MeV ion irradiation 12
  - 1.1.7 Sputtering 12
  - 1.1.8 Surface patterning by ion beam sputtering 13
  - 1.1.9 Morphological evolution of the surface after ion beam sputtering 15
  - 1.1.10 Scaling Theory 17

2 Experimental techniques **26**

- 2.1 Ion irradiation techniques 26

2.1.1 MeV ion irradiation-implantation 26
2.1.2 keV ion irradiation-sputtering 29
2.2 Sample characterization techniques 30
2.2.1 Scanning Probe Microscopy(SPM) 30
2.2.2 X-ray Photoelectron Spectroscopy (XPS) 36
2.2.3 Raman spectroscopy 39

3 Nano-Pattern formation and Surface Modifications after keV Irradiation on InP(111) 48
3.1 Introduction 48
3.2 Experimental 50
3.3 Results and Discussion 51
3.3.1 Roughness and scaling exponent studies of the nano-patterned surface 57
3.3.2 Raman scattering studies of the nano patterned surfaces . . . 61
3.3.3 Studies of stoichiometry of the ion irradiated nano-patterned surface by XPS 63
3.4 Summary and Conclusion 67

4 Nano pattern formation and surface modification by 1.5 MeV Sb ion irradiation on InP(111) 71
4.1 Introduction 71
4.2 Experimental 73
4.3 Results and Discussion 74
4.3.1 Surface Roughening and Radial Separation Distribution Studies 81
4.3.2 Studies of surface evoluation due to ion irradiation via the scaling parameters 87
4.4 Summary and conclusions 91

5 Raman Scattering Characterization and Electron Phonon Coupling Strength for MeV implanted InP(111) 94

5.1 Introduction 94

5.2 Experimental 96

5.3 Results and Discussion 97

5.4 Summary and Conclusion 110

6 Summary and Conclusion 114

List of Figures

1.1 Basic materials modification processes (a) implantation; (b) damage; and (c) sputtering, Adapted from Ref.[34] 5

1.2 Variation of stopping power, nuclear energy loss S_n and electronic energy loss S_e for Sb ions in InP target estimated using SRIM2006 simulation code[40] 7

1.3 Schematic defining the ion range parameters R_T, R_P, ΔR_P, and ΔR_L used to characterise the ion implanted distribution. Adapted from Ref. [49] 11

1.4 Two-dimensional profile of the distribution of energy deposition, Eq (1.11). σ and μ are the transversal and longitudinal widths of the Gaussian, respectively. The reference considered in the text are also shown. Adapted from Ref. [34] 14

1.5 Sketch of deposited energy for two different profiles. The energy deposited at O is larger than at O'. This induces more erosion in surface valleys than in crests, which produces a morphologic instability in the system. Adapted from Ref. [34] 15

2.1 Schematic diagram of the 3 MV tandem Pelletron accelerator along with various beamlines. 28

2.2 Schematic diagram for low energy ion erosion. 29

2.3 A schematic diagram of atomic force microscopy 32

2.4 Inter-atomic force vs. distance 33

2.5 Multi mode SPM in our laboratory 35
2.6 Schematic diagram of core level x-ray photoelectron emission process. 37
2.7 Schematic diagram of the XPS System in our laboratory. 38
2.8 Energy level diagram demonstrating Raleigh and Raman (Stokes and Anti-Stokes) scattering of photons. 40
2.9 **(a)** Dispersion curves of InP in the direction of (111) axis. **(b)** Confinement of phonon due to finite size **L** of the crystallite of InP. Adapted from Reference[16, 17]. 42
2.10 Theoretical Raman spectra for bulk crystalline InP (c-InP) and nanocrystalline InP (nc-InP) where $\Delta\omega$, Γ, Γ_a and Γ_b are shown. The evolution of Raman line-shape, as a function of decreasing coherence length, L is shown. Note the apparent downward shift in peak position which accompanies the skewing of the Raman peak as L decreases. Line shapes have been obtained using eqn. 2.14. 44
2.11 Schematic block diagram of the Raman setup with 180^0 scattering configuration 45
3.1 500×500 nm^2 SPM images of InP surfaces for the virgin sample (a), as well as after sputtering it for 5 min (3×10^{15} $ions/cm^2$)(b), 10 min (6×10^{15} $ions/cm^2$)(c), 20 min (12×10^{15} $ions/cm^2$)(d), 30 min (18×10^{15} $ions/cm^2$)(e), 40 min (24×10^{15} $ions/cm^2$)(f), 60 min (36×10^{15} $ions/cm^2$)(g), and 80 minutes(48×10^{15} $ions/cm^2$) (h). 52
3.2 Size (a) and height (b) distributions of the nanostructures formed after sputtering. 53
3.3 Mean size (a) and mean height (b) of the nanostructures formed at different sputtering time. t_c represent the critical time (discussed in the text) 54
3.4 SEM image showing $3\mu m \times 2.7\mu$m pattern of self assembled nano dots formed after 40 min of sputtering. 55

3.5 Auto-correlation pattern after (a) 10 min sputtering from 150 $nm \times$ 150 nm SPM image and (b) 40 min sputtering from 1000 $nm \times 1000$ nm SPM image. 56

3.6 Variation of rms surface roughness and spatial wavelength are plotted as a function of sputtering time and fluence (top axis). 57

3.7 A typical PSD spectrum and the corresponding wavelength(λ) for 40 min sputtering has been shown here. 58

3.8 Showing the log-log plot rms roughness σ versus sputtering time t. The value of β was extracted from a linear fit of the log-log plot of σ vs t. 59

3.9 Showing the rms roughness σ versus scan length L at different sputtering time. The solid lines represent the best power law fit $\sigma \sim L^{\alpha}$ with $\alpha = 0.77$ 60

3.10 Raman Spectra of virgin InP and 3keV sputtered InP surfaces after sputtering for (a)5 min, (b) 10 min, (c) 20 min, (d) 30 min, (e) 40 min, (f) 60 min, and (g) 80 minutes. 62

3.11 High Resolution XPS of Indium (3d) region is shown for (a)virgin as well as after the irradiation for (b) 2 min, (c) 5 min, (d) 10 min, (e) 20 min, (f) 30 min, (g) 40 min, (h) 60 min and (i) 80 min. In($3d_{5/2}$) and In($3d_{3/2}$) regions are marked in the figure. 63

3.12 High Resolution XPS of Indium (3d) region is shown for (a)virgin as well as after the irradiation for (b) 2 min, (c) 5 min, (d) 10 min, (e) 20 min, (f) 30 min, (g) 40 min, (h) 60 min and (i) 80 min. 64

3.13 Ratio of areas of In(3d) and P(2p) features for the virgin InP as well as after sputtering it for various sputtering times or fluences (top axis) 65

4.1 10 $\mu \times 10$ μ SPM images of InP surfaces for the virgin sample as well as after implantation with 1.5 MeV Sb ions at a fluence of (a) 1×10^{11} $ions/cm^2$, (b) 1×10^{12} $ions/cm^2$, (c) 1×10^{13} $ions/cm^2$, (d) 1×10^{14} $ions/cm^2$, (e) 5×10^{14} $ions/cm^2$. and (f) 1×10^{15} $ions/cm^2$ 75

4.2 Size distributions of the surface structures after 1.5 MeV Sb implantation with fluences of (a) 1×10^{11} $ions/cm^2$, (b) 1×10^{12} $ions/cm^2$, (c) 1×10^{13} $ions/cm^2$, (d) 1×10^{14} $ions/cm^2$, (e) 5×10^{14} $ions/cm^2$. and (f) 1×10^{15} $ions/cm^2$ 76

4.3 Height distributions of the surface structures after 1.5 MeV Sb implantation with fluences of (a) 1×10^{11} $ions/cm^2$, (b) 1×10^{12} $ions/cm^2$, (c) 1×10^{13} $ions/cm^2$, (d) 1×10^{14} $ions/cm^2$, (e) 5×10^{14} $ions/cm^2$. and (f) 1×10^{15} $ions/cm^2$ 77

4.4 InP surface SPM images (a) 1×1 μm^2, (b)0.5×0.5 μm^2 and (c) 0.2×0.2 μm^2 after implantation at fluence of 1×10^{13} $ions/cm^2$. Images (d) 1×1 μm^2, (e)0.5×0.5 μm^2 and (f) 0.2×0.2 μm^2 are after implantation at fluence of 5×10^{14} $ions/cm^2$. 79

4.5 InP surface SPM images and SPM-section analysis of (a) 1×1 μm^2 image for 1×10^{11} $ions/cm^2$ (b) 1.0×1.0 μm^2 image for 1×10^{12} $ions/cm^2$ (c) 0.4×0.4 μm^2 image for 1×10^{12} $ions/cm^2$ (d) 1×1 μm^2 image for 1×10^{13} $ions/cm^2$ (e) 1×1 μm^2 image for 5×10^{14} $ions/cm^2$ (f) 0.5×0.5 μm^2 image for 1×10^{15} $ions/cm^2$. (L is the lateral dimension and H is the height of the nanostructure labelled with arrows) 80

4.6 The rms surface roughness (σ) of the Sb implanted InP(111) surfaces, measured using SPM, is plotted as a function of Sb ion fluence. Data for the virgin sample is also shown. 82

4.7 Plots of power spectral density (PSD) function vs spatial frequency q of InP surfaces for the virgin sample as well as after implantation of InP(111) with 1.5 MeV Sb ions at various fluence. 84

4.8 Scaled radial distribution function for finding the surface-nanostructure separated by a distance r from a given nanostructure. The radial distribution is shown for all fluences. The solid line is given by $1 - \left(\frac{K_0(r/\sqrt{D\tau})}{K_0(r_0/\sqrt{D\tau})}\right)$ where K_0 is the modified Bessel function of order zero, and $D\tau \sim 1/4\pi N$, with $\sqrt{N} \sim 1/\langle R\rangle$ [5]. The error bars denote the standard error in measurement 85

4.9 The log-log plot of rms roughness as a function of ion fluence is shown at various length scans (L) of $10\mu m$, $1\mu m$ and $0.1\mu m$. The solid lines show power law fit to data. Inset shows the rms roughness as a function of ion fluence. 87

4.10 Showing the rms roughness versus scan length L at different fluences. The solid lines represent the best power law fit $\sigma \sim L^{\alpha}$ with $\alpha = 0.84 \pm 0.08$ 89

4.11 The wavelength (λ) of the implanted surfaces, measured using SPM, is plotted as a function of ion fluence. Inset shows the power spectral density distributions for some representative fluences. 90

5.1 First order optical Raman spectra of virgin InP (a) and 1.5 MeV Sb implanted InP at ion fluences of 1×10^{11} $ions/cm^2$ (b), 1×10^{12} $ions/cm^2$ (c), 1×10^{13} $ions/cm^2$ (d), 1×10^{14} $ions/cm^2$ (e), 5×10^{14} $ions/cm^2$ (f) and 1×10^{15} $ions/cm^2$ (g) 98

5.2 Evolution of first order LO and TO modes: The intensity of both LO and TO modes normalized with respect to virgin (a), FWHM of both LO and TO modes (b) the shift in position (ω) of LO mode (c) and shift in position (ω) of TO mode (d) are shown as a function of ion fluence. Data for the virgin sample are also shown. 100

5.3 Evolution of L$^-$ mode: The intensity of L$^-$ mode normalized with respect to virgin (a), FWHM (b) and the shift (ω) in position (c) are shown as a function of ion fluence. Data for the virgin sample are also shown. 102

5.4 Second order optical Raman spectra of virgin InP (a) and 1.5 MeV Sb implanted InP at ion fluences of $1 \times 10^{11}\ ions/cm^2$ (b), $1 \times 10^{12}\ ions/cm^2$ (c), $1 \times 10^{13}\ ions/cm^2$ (d), $1 \times 10^{14}\ ions/cm^2$ (e), $5 \times 10^{14}\ ions/cm^2$ (f) and $1 \times 10^{15}\ ions/cm^2$ (g) 103

5.5 Evolution of second order 2LO and 2TO modes: The intensity of both 2LO and 2TO modes normalized with respect to virgin (a), FWHM of both 2LO and 2TO modes (b) the shift in position (ω) of 2LO mode (c) and shift in position (ω) of 2TO mode (d) are shown as a function of ion fluence. Data for the virgin sample are also shown. 104

5.6 Evolution of LO+TO mode: The intensity of LO+TO mode normalized with respect to virgin (a), FWHM (b) and the shift (ω) in position (c) are shown as a function of ion fluence. Data for the virgin sample are also shown. 105

5.7 Raman spectra of Sb implanted InP(111) at various fluences fitted with PCM; ●: experimental data, –: PCM fit to data. L($\AA$) is the phonon coherence length as determined by the fit to the data. Fitting for the virgin sample is also shown. 107

5.8 Electron Phonon Coupling Strength: Normalized Raman intensity of second-order 2LO phonon with respect to that of first-order LO as a function of ion fluence. Value for the virgin bulk-InP is also shown. The coherence lengths (L), at all fluences, are also marked on the top axis. 109

Chapter 1

Introduction

1.1 Introduction

Nanotechnology and Nanoscience are inducing a turning point in fields from Condensed Matter Physics and Materials Science to Chemistry and Biology. This is due to the new types of behaviors and properties displayed by nanostructures, ranging across traditional disciplines [1]. Interest in these systems is also triggered by the possibility of characterizing them morphologically by scanning probe microscopy techniques (SPM) [2] as well as by other advanced surface structure determination methods. Within this more specific context, there is an increasing need for the development of techniques and methods for the patterning of materials at the nanoscale. Moreover, this goal must be achieved in an efficient, fast and low-cost manner for eventual technological applications to be compatible with mass-production. In addition, the processes involved should allow control over the size, shape and composition of the nanostructures produced. Within this trend, there is also a great interest in developing methods for producing confined nanostructures, which would display quantum confinement effects, on surfaces. Of especial interest would be those systems in which these surface nanostructures form an ordered pattern.

Since with shrinking dimensions the conventional "top down" approach using lithographic techniques become more expensive and technologically challenging, the bottom up approach, where atoms or molecules spontaneously form nanostructures which self organize into qausiperiodic arrays, is an elegant alternative. Thus, an exploration of self-organization phenomena at crystalline surfaces became an attractive research topic in the last decade [3]. Self-organization due to ion beam irradiation on semiconductor surfaces is one of the emerging field in this area [4]. The potential of this bottom-up approach has been enhanced due to the ease and the reproducibility achievable as well as the possibility of production of regular arrays of dots on large areas in a single technological step.

Unique properties of InP have attracted enormous interest. It is being widely applied in high speed electronic and opto- electronic devices due to its attractive electronic properties [5, 6, 7] as well as its excellent lattice match with low band gap alloys like GaInAs, GaInAsP, AlGaInAs etc. GaInAsP/InP based photo-diodes operate in low loss window of silica fibers with high quantum efficiency and fast response time. Due to its excellent physical properties like high thermal conductivity, high peak velocities for electrons and holes, InP is considered an important semiconductor material and it is being prominently utilized in the devices for high electron mobility transistors, high efficiency and high speed quantum well lasers, photo-detectors, photonic integrated circuits etc. InP is also preferred, over GaAs based devices, for Millimeter-wave sources and amplifiers due to its low noise and higher efficiency operations in high frequency regime. Junction field effect transistors fabricated on InP display high performance.

Ion bombardment of solids often gives rise to characteristic surface topographies, which depend on ion beam parameters, such as ion fluence, ion energy, incident angle, sample temperature etc.[8, 9, 10, 11]. Height modulations on the sub-micron scale have been observed for crystalline semiconductors [12, 13] as well as for crystalline metals[14, 15], and some amorphous and polycrystalline materials[16]. Ion beam sputtering(irradiation) is frequently regarded as an alternative process for the fabrication of various nano-structured surfaces or interfaces via self organization. Under certain conditions sputtering can roughen this surface resulting in a pronounced topography evolution in some cases producing well ordered pattern [17, 18, 19, 20, 21]. This pattern formation is related to the surface evolution due to the competition between curvature dependent ion sputtering that roughens the surface and smoothing by different relaxation mechanism [22, 23, 24]. Recent studies show the formation of ordered InP nanostructure by Ar^+ ion sputtering under normal ion incidence [25, 26, 4] or alternatively under oblique ion incidence with simultaneous sample rotation [28]. Generally for off-normal ion incidence without sample rotation, a periodic height modulation in the form of ripple or wave like structure with a sub-micron length scale develops during ion bombardment as observed for single crystalline III-V semiconductors [27, 28].

MeV ion-beam implantation techniques are extensively utilized for device processing in semiconductor industry. Due to its low thermal stability, MeV ion implantation is a prominent way to introduce and dope the materials in InP. MeV implantation is also important for forming thick buried layers with modified properties as well as modification of vertically limited layers and quantum well structures. The increased density in VLSI circuits also makes the technological applications of the ion implantation, especially in MeV energy range, increasingly important. Sb is considered an important dopant because of its role in the development of field effect transistors and infrared detectors [29, 30]. Sb has also found applications as isoelectronic dopant for trapping charge carriers in InP [31]. MeV implantation, however, can also produce severe modifications in the material depending on the nature and the energy of the impinging ion, and the implantation dose [30]. Extensive usage of ion implantation in device fabrication and the continued miniaturization of device structures has brought the issue of surface modifications, via ion implantations, to the forefront. However, the factors responsible for such modifications and the surface morphology after ion implantation, have received little attention [32]. These issues are important from fundamental as well as technological point of view for ion implantation to be a viable candidate for the development in semiconductor technology. Since roughness of surface can crucially effect the performance and reliability of devices [33], it becomes necessary to characterize the surface roughness and understand the processes influencing it. The formation and the development of the surface structures, due to the ion implantation, are also gaining importance because of the realization that these structures can be utilized for controlled fabrication of semiconductors similar to self-organized growths.

1.1.1 Basics of Ion-Solid interaction

Energetic ions incident on a solid material can influence its properties and are utilized in research and technology in various ways[35]. Primary processes leading to material modification via ion beam irradiation are shown in figure 1.1. As shown in fig. 1.1(a) ion implantation can lead to the build up of a concentration profile of foreign atoms within a solid, thus altering the composition in the implanted zone. The spatial distribution of foreign atoms will depend on the ion energy and the stopping (nuclear and electronic) processes. Figure 1.1(b) illustrates that the 'hard' nuclear collisions can causes the displacement of target atoms from their regular lattice sites. A single heavy ion can lead to the displacement of several tens, or even hundreds, of lattice atoms within the volume surrounding the ion trajectory. This is termed as collision or displacement cascade. As a consequence, ion bombardment can create considerable structural damage to the material. Figure 1.1(c) illustrates that nuclear collision of ions can sometimes lead to the ejection of surface atoms from target through the process of sputtering. This phenomenon of sputtering can cause surface erosion and can also sometimes produce self assembly of nano structure on surfaces. The phenomenon of sputtering is predominant at low (keV) energies whereas the lattice modification

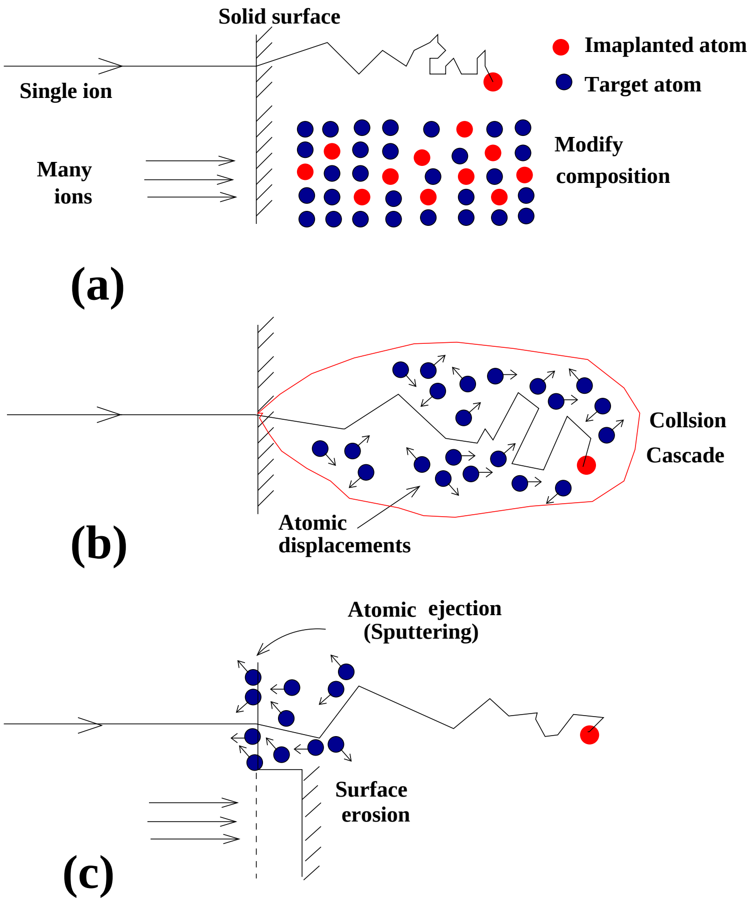

Figure 1.1: Basic materials modification processes (a) implantation; (b) damage; and (c) sputtering, Adapted from Ref.[34]

and deep layer implantations occur at high (MeV) energies.

In materials synthesis and modifications, an ion loses energy by two nearly uncorrelated processes. Elastic collisions with the atomic nuclei, produce nuclear energy loss ($S_n = (dE/dx)_n$) whereas inelastic excitations and ionizations of the electrons produce electronic energy loss ($S_e = (dE/dx)_e$) [36, 37]. The basic interaction process in both the cases is Coulomb type, a pure Coulomb potential for ion-electron interactions and a screened Coulomb potential for nuclear case. However, the energy regions of the dominance for these two processes are different. At ion energies of a few keV/amu, where the ion velocity is much less than the Bohr velocity of electrons, the interaction time between the projectile and a nucleus is relatively large. In this energy regime, nuclear loss is the predominant mechanism. At higher energies of about a few MeV/amu, where projectile velocity is comparable to the Bohr velocity of electrons, inelastic electronic energy loss becomes the major slowing down process. The distinct regions of S_n and S_e dominance are shown in fig. 1.2 which shows the variations of both the stopping powers of antimony (Sb) ions traversing through indium phosphide (InP) single crystal target as a function of energy. Levalois, Bogadanski, and Toulemonde[38] have studied the effect of swift heavy ion (SHI) on semiconductor materials and have shown that S_e is insensitive in creating defects in the bulk lattice. Even Motooka, Harada, and Ishimaru[39] have shown that S_e does annealing of the defects produced by S_n processes. In these studies, the effect of S_e has been neglected in defect production. On the other hand, electronic excitations due to S_e have been realized as a mechanism for defect annealing.

1.1.2 Nuclear Energy loss

Nuclear collisions usually involve large discrete energy transfer and significant angular deflections of the ions from their trajectory. The energy deposited through these collisions result in the production of lattice disorder by the displacement of atoms from their equilibrium positions. These displaced atoms sometime have sufficient energy to cause cascade of secondary displacements of the secondary atoms to form a tree of disorder along the ion path. When the concentration of displaced atoms per unit volume approach the atomic density of a semiconductor, the material becomes amorphous. Ion fluence (ions falling per unit area) also plays a crucial role in the defect formation. At low fluences, disordered zones created by different ions remain generally well separated from each other. However, as the fluence increases, these zones start overlapping leading to the amorphization of the material.

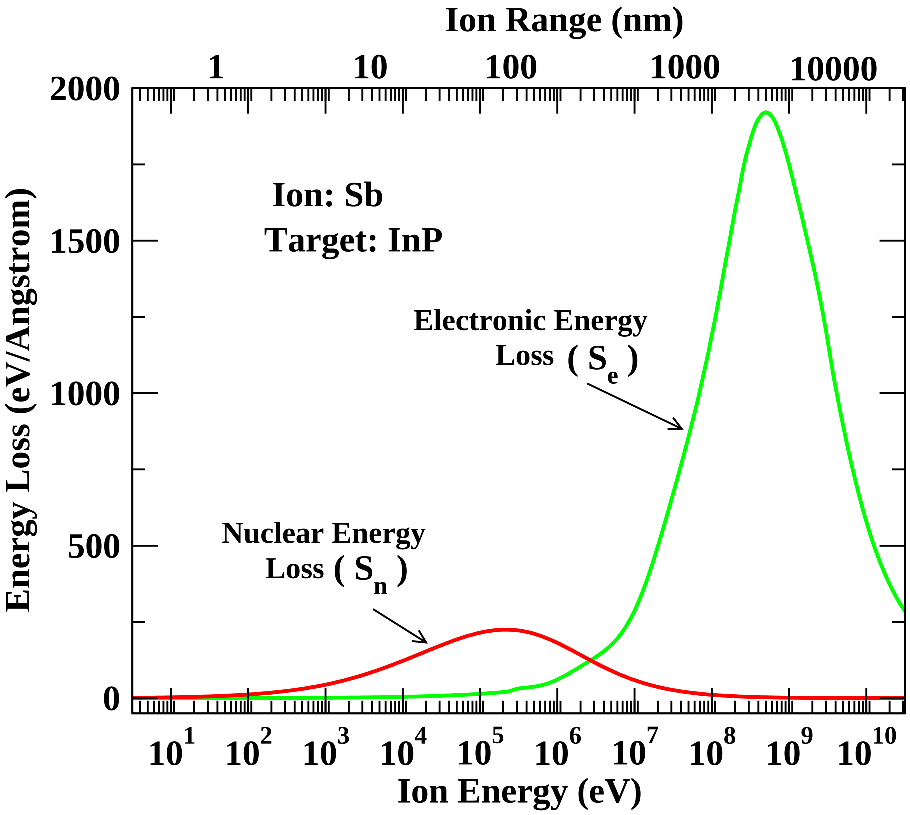

Figure 1.2: Variation of stopping power, nuclear energy loss S_n and electronic energy loss S_e for Sb ions in InP target estimated using SRIM2006 simulation code[40]

The process of nuclear stopping could be visualized by a series of classical elastic scattering events between an incoming hard sphere (energy E_0 and mass M_0) and a target hard sphere (zero initial energy and mass M_1), usually known as a binary collision approximation. The kinetic energy transfer (T) from incident particle to the target can be derived as a function of scattering angle (θ) using the requirement of momentum and energy conservation[37, 41]:

$$T = T_{max}\ sin^2\frac{\theta}{2};\quad T_{max} = \frac{4M_0M_1}{(M_0+M_1)^2}\ E_0 \tag{1.1}$$

The probability $P_{1,2}$ of a two-atom collision process occurring in a target of thickness x is characterized by the cross-section σ, $P_{1,2} = 2x\sigma$ and the appropriate form of the nuclear scattering cross section is expressed by [42, 43]:

$$d\sigma(E,T) = C_m E^{-m} T^{-1-m} dT; \tag{1.2}$$

where $C_m = \frac{\pi}{2}\lambda_m u^2 \left(\frac{M_0}{M_1}\right)^m \left(\frac{2Z_0Z_1e^2}{u}\right)^{2m}$

Here $u = 0.885a_0(Z_0^{2/3} + Z_1^{2/3})^{-1/2}$, where a_0 is the Bohr radius, Z$_0$ and Z$_1$ are the atomic numbers of the ion and the target, and λ_m is a function that depends upon the parameter m; for high energy, m approaches unity, and for low energy m vanishes. The nuclear stopping power $(dE/dx)_n$ is defined as the mean ionic energy loss due to elastic collisions per unit length: $(dE/dx)_n = \int T d\sigma$. Using eqn (1.2),

$$\left(\frac{dE}{dx}\right)_n = \frac{1}{1-m} C_m \gamma^{1-m} E^{1-2m}, \tag{1.3}$$

with $T_{max} = \gamma E$, where $\gamma = \frac{4M_0M_1}{(M_0+M_1)^2}$ is the reduced mass.

1.1.3 Electronic Energy loss

An ion incident on the target excites or ejects atomic electrons.This causes electronic energy loss. This electronic energy loss comes from the "frictional resistance" that the projectile encounters on its passage through the electron clouds surrounding each target atom, and is viewed as an inelastic interaction due to the complex nature of the energy loss process. Electronic scattering is a minor effect, because electron mass m_e is much smaller than the mass M_1 of the impinging ion. Electronic collisions involve very small energy losses per collisions, negligible deflection of the ions trajectory, and negligible lattice disorder. In addition to stopping, the electronic interaction of an ion passing through matter results in charge changing collisions, so that the actual charge state of a fast ion in matter fluctuates continuously and is determined by a balance between electron loss and electron attachment. The average charge of the ion, which depends on its velocity (v_0), is denoted as effective charge, Z_0^{eff} , and is quickly established (typically within some nm) when an ion of any charge state impinges onto a solid surface. In the limit of very low energy, the ion becomes neutral with a vanishing effective charge, so that projectile electrons interact with the electrons of the solid. At high velocities, the projectile starts getting stripped-off its electrons and looses all its electrons at $v \geq v_0 Z_0^{2/3}$. The ion, at this point, could be visualized as positive point charge $Z^{eff} = Z_0$ moving with velocities greater than the mean orbital velocity of atomic electrons in the target. Because of the high ion velocity, the influence of the incident particle may be regarded as a sudden, small perturbation to the electron cloud. This picture leads to the Bohr's theory of stopping power. The effective charge of an ion as estimated by Bohr is given by[41]:

$$Z_0^{eff} = Z_0\Big[1 - exp\Big(-\frac{v}{v_o} Z_0^{-2/3}\Big)\Big] \tag{1.4}$$

with the upper limit of velocity defined by $Z_0^{eff} = Z_0$.

At ion velocities where $v < v_0 Z_0^{2/3}$, the widely used model for electronic stopping power calculation was given by Lindhard and Scharff [44, 45]. In this region, the electronic stopping power is given by:

$$\left(\frac{dE}{dx}\right)_e = 3.83 \frac{Z_0^{7/6} Z_2}{(Z_0^{2/3} + Z_1^{2/3})^{3/2}} \left(\frac{E}{M_1}\right)^{1/2} = K_L E^{1/2} \tag{1.5}$$

or

$$\left(\frac{dE}{dx}\right)_e \propto v_{ion} \tag{1.6}$$

The stopping power is proportional to ion velocity in this regime.

For higher ion velocities $v \geq v_0 Z_0^{2/3}$, Bethe and Bloch [46, 47] provided a good estimate with the base lying in the Bohrs classical theory of ion stopping. In the non-relativistic limits, the electronic energy loss is given by:

$$\left(\frac{dE}{dx}\right)_e = \frac{2Z_0^2 e^4}{E} N Z_1 \left(\frac{M_1}{m_e}\right) ln \frac{2m_e v_{ion}^2}{I} \tag{1.7}$$

In this thesis, the results are presented for the ion irradiation of InP(111) surface with 3 keV Ar ion and 1.5 MeV Sb ion. For 3 keV Ar ion irradiation on InP target, the nuclear and electronic energy losses are calculated to be $\left(\frac{dE}{dx}\right)_e = 0.05$ keV/nm and $\left(\frac{dE}{dx}\right)_n = 0.34$ keV/nm, respectively. For 1.5 MeV Sb ion irradiation on InP, it is $\left(\frac{dE}{dx}\right)_e = 0.84$ keV/nm and $\left(\frac{dE}{dx}\right)_n = 1.58$ keV/nm . Due to the ion energies used here, nuclear effects are dominant compared to electronic effect.

1.1.4 Ion Range

The energy loss of the projectile with penetration depth x can be expressed as the sum of nuclear and electronic energy loss terms, i.e.

$$\frac{dE}{dx} = \left(\frac{dE}{dx}\right)_n + \left(\frac{dE}{dx}\right)_e \tag{1.8}$$

The total distance traveled by the ion, before coming to rest, is called the range (R_T) and can be found by integration of above equation to give:

$$R_T = \int_0^{E_0} \left(\frac{dE}{dx}\right)^{-1} dE \tag{1.9}$$

where E_0 is the incident energy. Since energy is lost by the projectile to the target atoms and electrons in a series of discrete collisions, the energy loss per collision and hence the total path length will have a statistical spread of values. This leads to a near-Gaussian distribution of stopping distances. The stopping processes and typical ion range parameters describing the distribution of stopping distances are illustrated in fig. 1.3. The trajectory of the penetrating ion is fairly straight when electronic stopping dominates but it follows a zig zag path as it slows down and undergoes more frequent nuclear collisions. As a result, the stopping distance or projected range, R_P, along the incident ion direction can be considerably less than the total path length or range, R_T. The projected range and the associated statistical spread (standard deviation) both parallel (ΔR_P,) and perpendicular (ΔR_L) to the ion direction are more useful practical range parameters than those relating to the total path length.

1.1.5 Implantation

Ion implantation is a process by which ion of a material can be introduced into another solid, thereby changing the physical properties of the solid. Ion implantation

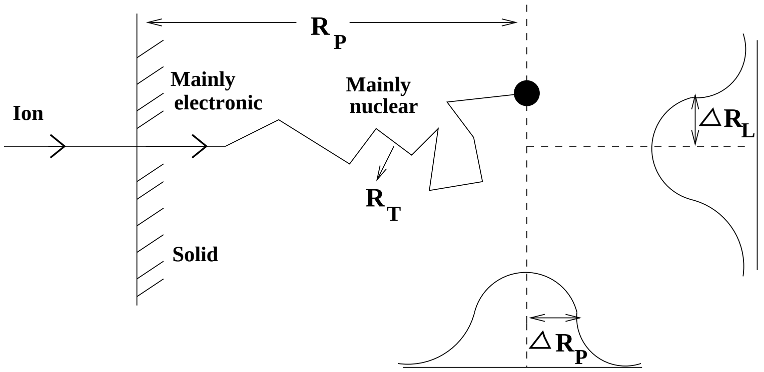

Figure 1.3: Schematic defining the ion range parameters R_T, R_P, ΔR_P, and ΔR_L used to characterise the ion implanted distribution. Adapted from Ref. [49]

is used in semiconductor device fabrication and in metal finishing, as well as various other applications in materials science research. The ions introduce both a chemical as well as structural modifications in the target.

Ion implantation-irradiation system typically consist of an ionization chamber, where ions of desired element are produced, an accelerator, where ions are electrostatically accelerated to a specific energy, and target chamber, where ions impinge on a target. The number of ions implanted in the target is determined from the time integral of the current and the known charge state of the ion. The number of ions implanted per cm^2 of the target is called the fluence. The current supplied by the implanters are typically small (nano Amperes), and so the fluences which can be implanted in reasonable amount of time are small. Thus, the ion implantation finds application in cases where the required concentration of implanted ions is small.

During ion implantation, interactions of the energetic ion with the host atoms produce collisions. In these collisions, sufficient energy may be transferred from the ion to displace the host atom from its lattice site. The displaced atom can in turn displace other atoms, and so on - thus creating a cascade of atomic collisions within the solid. This leads to a distribution of vacancies, interstitial atoms, and other types of lattice disorder in the region around the ion track. As the number of ions incident on a crystal increases, the individual disordered regions begin to overlap. At some stage an amorphous layer may form. The total amount of damage and its depth distribution will depend on the implanted species, its energy and ion dose, substrate temperature, and the channeling effects[48, 49].

1.1.6 Surface Modification due to MeV ion irradiation

During MeV ion irradiation, an incident ion sets several target atoms into motion, thus causing several modifications in bulk lattice via damage due to the displacement of lattice atoms and implantation. However modifications also occur on the surfaces[50]. At such high energies, the surface can get modified in interesting ways depending on the fluence and tilt angle of the incident ion[51]. MeV ion irradiation can lead to extensive modification of the surface and bulk lattice. Although the bulk modifications, after MeV irradiation, have received much attention, surface modification have not been studied much. Recently, the issue of surface modifications has become important [52, 53, 54, 55, 56, 57, 58] due to the realization that the self-assembled surface structures can develop after MeV ion irradiations. The self assembled structures are related to the damage on the surface. The self assembled patterns displays several scaling properties discussed in the following sections.

1.1.7 Sputtering

Sputtering is the removal of near surface atoms from the target. An ion sputtering event is best described as a collision process [61] involving electronic stopping and nuclear scattering. Ion sputtering occurs when an ion colliding with one or more target nuclei results in elastic scattering events. If the energy thus imparted to near surface atoms is large enough to break atomic bonds, atoms are sputtered. Sputtering yield (S) is defined as the mean number of sputtered target atoms per incident ion:

$$S = \alpha N S_n(E)/E_B \tag{1.10}$$

Here, N is the target atom density, E_B is the binding energy of a surface atom and α is a material and geometry dependent parameter. The product $NS_n(E)$ represents the energy loss per unit length as the ion travels in the target.

As the definition of sputtering yield implies, the number of atoms removed are assumed proportional to the number of incident particles while holding all other factors constant. Sputtering yield is strongly dependent on the kinetic energy of the bombarding ion. The sputtering yield is very sensitive to the surface binding energy and for real surfaces this changes with its roughness and stoichiometry.

When multi-component targets are bombarded with heavy ions, various elemental constituents may not be sputtered at the same rate. Preferential sputtering, of lighter atoms compared to heavier atoms, can result in a surface composition which differs appreciably from the stoichiometric bulk composition[62, 63]. It is difficult to distinguish between preferential sputtering and other processes such as radiation-induced mass transport and segregation effects, all of which may lead to near-surface composition changes during sputtering.

1.1.8 Surface patterning by ion beam sputtering

A quantitative description of the process of ion sputtering was developed by Sigmund[22]. Assuming an infinite medium, he found that, in the elastic collision regime at the energies of a few keV where electronic stopping is not dominating, the deposited energy can be approximated by Gaussian distribution near its maximum. Specifically, the density of energy spread out in the bulk by an ion with kinetic energy E is given by

$$\epsilon_s(r\prime) = EN_s.exp\Big[-\frac{x\prime^2 + y\prime^2}{2\mu^2} - \frac{(z\prime + a)^2}{2\sigma^2}\Big] \tag{1.11}$$

where the origin of the $r\prime = (x\prime, y\prime, z\prime)$ coordinate system is placed at the impact of the ion within the surface; $\hat{z}\prime$ is aligned along the ion beam direction, and

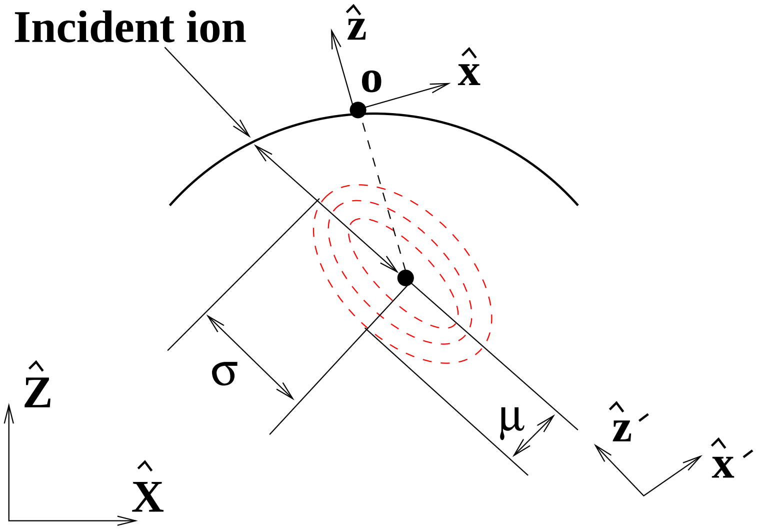

Figure 1.4: Two-dimensional profile of the distribution of energy deposition, Eq (1.11). σ and μ are the transversal and longitudinal widths of the Gaussian, respectively. The reference considered in the text are also shown. Adapted from Ref. [34]

$\hat{x}\prime$ and $\hat{y}\prime$ belong to the perpendicular plane to $\hat{z}\prime$ (see fig. (1.4)). In Eq. (1.11), $N_s = [(2\pi)^{3/2}\sigma\mu^2]^{-1}$ is a normalization constant and due to the initial momentum of the ion, the maximum energy deposition occurs at a distance along the ion trajectory inside the bulk. The longitudinal and transverse straggling widths of the distribution are σ and μ respectively.

As we noted above,correlation of the sputtering yield with the surface topography is a crucial issue. In ref.[22] Sigmund showed that the topography of the surface can indeed influence the magnitude of the rate of erosion and, provided an analytical description that describes the increase of yield for geometries different from the flat morphology. It is assumed that the speed of erosion at a point O on the surface is proportional to the amount of energy deposited there by the ions, see figure 1.5.

Let us suppose that, as shown in Fig. 1.5, we irradiate a certain surface with a

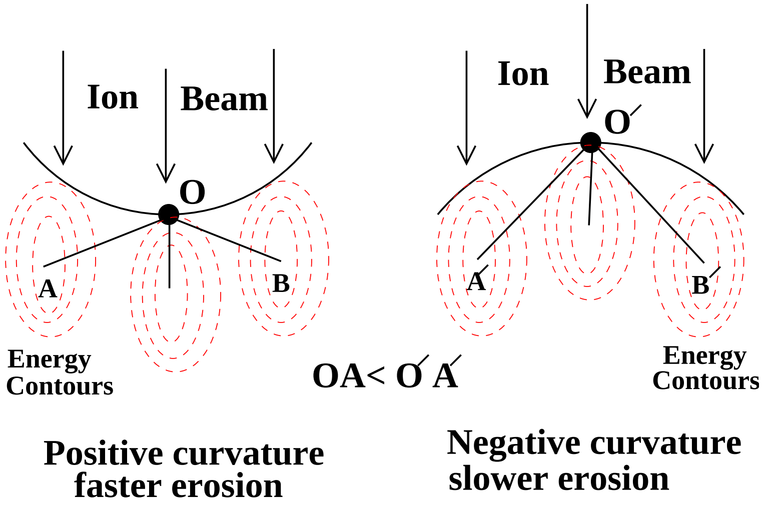

Figure 1.5: Sketch of deposited energy for two different profiles. The energy deposited at O is larger than at O'. This induces more erosion in surface valleys than in crests, which produces a morphologic instability in the system. Adapted from Ref. [34]

homogeneous flow of ions. We can verify that distances OA and OB are smaller than $O'A'$ and $O'B'$ due to the geometry of the interface. This implies that, for this energy distribution, the penetrations of ions at A and B induce large energy deposition at O than the impacts on A' and B' at O'. As the rate of erosion is proportional to the deposited energy, erosion is faster at O than at O'. Thus, valleys are eroded more quickly than crests. This amplifies the initial differences in heights. This different rates of erosion cause surface instability. Sigmund suggested that an alternative process that flattens the surface must exist and he proposed atomic migration as a mechanism to correct this instability.

1.1.9 Morphological evolution of the surface after ion beam sputtering

A successful description of the morphological evolution of sputter eroded surfaces has been proposed by Bradley and Harper (BH) [23], based on Sigmund's theory of sputtering[64] predicting that the height h(x,y,t) of the eroded surface is described by the linear equation

$$\frac{\partial h}{\partial t} = -v_0 + \nu \nabla^2 h - D \nabla^4 h \tag{1.12}$$

where v_0 is the constant erosion velocity, ν is the effective surface tension and D denotes the surface diffusion which is activated by different physical processes (i.e. thermal diffusion, ion-induced diffusion) that may or may not involve lateral mass transport on the surface. The competition between the ion-induced surface instability and diffusive smoothening builds up a regular pattern on the surface with a characteristic wavelength. In general, the characteristic wavelength of the surface structure modulations is given by $\lambda = \sqrt{(2D/\nu)}$. The linear model of Eq.(1.12) predicts that the surface height grows exponentially with the fluence and the wavelength is independent of fluence.

Refined theories are based on BH model and include nonlinear effects with noise. Based on Sigmund's continuum theory of ion-beam sputtering [22] recently, Cuerno and Barabasi (CB)[20] or more generally Makeev, Cuerno, and Barabasi (MCB)[65] have developed a model to describe the ion-induced pattern formation on amorphous or semiconductor materials that are easily amorphized by ion bombardment. The early stage morphology predicted by the CB model[20] is similar to the linear instability theory developed by Bradley and Harper (BH)[23]. However, the late stage dynamics of the ion-induced morphology is dominated by the nonlinear terms of the Kuramoto-Sivashinsky (KS) equation [66] involved in the CB model[20] as described by Park et al.[24] and Rost and Krug[21]. Depending on the sign of the product of the coefficients of the two non- linear terms, the late stage morphology may show [20, 24, 21] kinetic roughening described by the universality class of the Kardar-Parisi-Zhang (KPZ) equation[67] or yield the formation of rotated ripple structure (RRS) [24, 67] or display dots and hole [4, 25, 26] on the ion eroded surface. Starting from the Bradley-Harper (BH) theory [23], description of the morphological evolution of the ion sputtered surface can be given by the isotropic KS equation [20, 21, 25, 26].

The temporal development of the surface profile h(x,y,t) is given by the following undamped KS equation:

$$\frac{\partial h}{\partial t} = -v_0 + \nu \nabla^2 h - D\nabla^4 h + \frac{\lambda}{2}(\nabla h)^2 + \eta, \tag{1.13}$$

where the nonlinear term $\frac{\lambda}{2}(\nabla h)^2$ accounts for the slope-dependent erosion yield that brings forth the saturation of surface roughness with time. η is an uncorrelated white noise with zero mean, mimicking the randomness resulting from the stochastic nature of ion arrival to the surface.

1.1.10 Scaling Theory

The surface topography, after ion beam bombardment, is controlled by the various roughening and the smoothening processes [68]. Recent studies have shown that the scaling theories applicable to non-equilibrium film growth may also be applicable to ion bombarded surfaces[17, 69]. Depending on the roughening and the smoothening processes relevant, surfaces will be governed by different scaling exponents[70].

Scaling theory is a theoretical tool to describe and characterize the roughening of non-equilibrium surfaces[71, 72, 73]. It has been observed that the roughness of many natural surfaces follows rather simple scaling laws, which can be quantified using scaling exponents. Let us consider a two-dimensional surface that is characterized by the height function h(x,y,t). The morphology and dynamics of a rough surface can be quantified by the interface width(σ), defined by the rms fluctuations in the height h(x,y,t),

$$\sigma(L,t) \equiv \sqrt{\frac{1}{L^2} \sum_{x,y=1.L} [h(x,y,t) - \bar{h}(t)]^2} \tag{1.14}$$

where L is the linear size of the sample and $\bar{h}$ is the mean surface height of the surface given as:

$$\bar{h}(t) \equiv \frac{1}{L^2} \sum_{x,y=1.L} [h(x,y,t) \tag{1.15}$$

It is general practice that instead of measuring the roughness of a surface over the whole sample size $L \times L$, one can choose a window of size $l \times l$ where $l < L$ and measure the local width, $\sigma(l)$. A general property of many rough surfaces is that the roughness depends on the length scale of observation. This can be quantified by plotting $\sigma(l)$ as a function of l. There are two characteristic regimes one can distinguish:

- For length scales smaller than l_c, the local width increases as[71]:

  $$\sigma(l) \sim l^{\alpha} \tag{1.16}$$

  where α is the roughness exponent. To investigate the surface phenomena that take place at length scales shorter than l_c, one cannot neglect the roughness of the surface. In this regime, the roughness is not simply a number, rather depends on the length scale of the measurement.

- For $l > l_c$, $\sigma(l)$ is independent of l, thus at length scales larger than l_c, one can characterize the surface roughness with the saturation width $\sigma_{sat} = \sigma(l_c)$.

  The dynamics of the roughening process can be best characterized by the time dependent total width, given by Eqn.(1.14). At early times the total width increases as[71]:

  $$\sigma(L,t) \sim t^{\beta} \tag{1.17}$$

  where β is the growth exponent.

However, for finite systems, after a critical time (t_c), the width saturates, following the $FamilyVicsek$ scaling function[72]

$$\sigma(L,t) \equiv t^{\beta} f(L/t^{\beta/\alpha}) \tag{1.18}$$

where f(x) is a scaling function such that f(x) is constant for $x >> 1$ and f(x) $\sim x^{\alpha}$ for $x << 1$. Thus the roughness has the scaling property $\sigma(L,t) \sim t^{\beta}$ before saturation and $\sigma(L,t) \sim L^{\alpha}$ after saturation.

The exponents β and α are, respectively, called as the growth and roughness exponents and characterize the nature of the surface roughness. The values of the exponents α and β are independent of many details of the system, and they are uniquely defined for a given universality class[71, 72]. In contrast, other quantities, such as l_c or σ_{sat}, are non-universal, i.e. they depend on almost every detail of the system[73, 74].

Bibliography

[1] Hodes G, When small is different: Some recent advances in concepts and applications of nanoscale phenomena, Adv. Mater. **19**, 639 (2007).

[2] Binnig G, Quate C, Gerber Ch (1986) Atomic force microscope. Phys Rev Lett **56**, 930 (1986).

[3] V.A. Schukin, D. Bimberg, Rev. Mod. Phy. **71**, 1125 (1999).

[4] S. Facsko, T. Dekorsy, C. Koerdt, C. Trappe, H. Kurz, A. Vogt, H. L. Hartnagel, Science **285**, 1551 (1999).

[5] D. Streit, Compound Semiconductors, May 2002.

[6] B. Humphreys, A. O'Donell, Compound Semiconductors, August 2003.

[7] D. Lammers, Electronic Engineering Times, 12 September 2002.

[8] U. Valbusa, C. Boragno, and F.B. de Mongeot, J. Phys.: Condens. Matter **14**, 8153 (2002).

[9] G. Carter, J. Phys. D **34**, R1 (2001); C. Teichert, Appl. Phys. A: Mater. Sci. Process. **76**, 653 (2003).

[10] J S Williams, Rep. Prog. Phys. **49**, 491-587 (1986).

[11] M. Chicoine, S. Roorda, L. Cliche, and R. A. Masut, Phys. Rev. B.**56**, 1551 (1997).

[12] G.W. Lewis, M.J. Nobes, G. Carter, and J.L. Whitton, Nucl. Instr. Meth. **179**, 363 (1980).

[13] E. Chason, T. M. Mayer, B. K. Kellermann, D. E. McIlroy, and A. J. Howard, Phys. Rev. Lett. **72**, 3040 (1994).

[14] S. Rusponi, G. Constantini, C. Boragno, and U. Valbusa, Phys. Rev. Lett.**81**, 4184 (1998).

[15] S. Habenicht, W. Bolse, K. P. Lieb, K. Reimann, and U. Geyer, Phys. Rev. B **60**, R2200 (1999).

[16] T. M. Mayer, E. Chason, and A. J. Howard, J. Appl. Phys. **76**, 1633 (1994).

[17] F. Frost, A. Schindler, and F. Bigl, Phys. Rev. Lett. **85**, 4116 (2000).

[18] Jonah Erlebacher, Michael J. Aziz, Eric Chason, Phys. Rev. Lett.**84**, 5800 (2000).

[19] B. Ziberi, F. Frost, Th. Hoche, and B. Rauschenbach, Phys. Rev. B.**72**, 235310 (2005).

[20] R. Cuerno, H.A. Makes, S.Tomassone, S.T. Harington, and A.-L. Barabási, Phys. Rev. Lett. **75** 4464 (1995).

[21] M.Rost and J. Krug, Phys. Rev. Lett. **75** 3894 (1995).

[22] Peter Sigmund, Phys. Rev. **184**, 383 (1969).

[23] R. Mark Bradley and James M. E. Harper, J. Vac. Sci. Technol. A **6**, 2390 (1988).

[24] S. Park, B. Kahng, H. Jeong, and A.-L. Barabasi, Phys. Rev. Lett.**83**, 3486 (1999).

[25] B. Kahng, H. Jeong and A.-L. Barabasi, Appl. Phys. Lett **78**, 805 (2001).

[26] S.K. Tan, A.T.S. Wee, J. Vac. Sci. Technol. B **24**, 1444 (2006).

[27] S.W. Maclaren, J.E. Baker, N.L. Finnegan, C.M. Loxton, J. Vac. Sci. Technol. A **10**, 468 (1992).

[28] F. Frost, B. Ziberi, T. Hoche, B. Rauschenbach, Nucl. Instr. and Meth. B **216**, 9 (2004).

[29] G. Tempel, N. Schwarz, F. Muller, F. Koch, H.P. Zeindl, and I. Eisele, Thin Solid Films **174**, 171 (1990).

[30] M.Tamura and T. Suzuki, Nucl. Instr. and Meth. **B39** 318 (1989).

[31] S.G. Bishop, B.V. Shanabrook, P.B. Klein, and R.L. Henry, Phys. Rev. B. **38**, 8469 (1988).

[32] G. Carter, M.J. Nobes, I.V. Katardjiev and J.L. Whitton Defect and Diffusion Forum, **vol.57/58**, 97 (1988) . Ion Implantation 1988, ed. F.H. Wohlbier (Trans. Techn. Publ. Ltd).

[33] D.J. DiMaria and D.R. Kerr, Appl. Phys. Lett. **27**, 505 (1975).

[34] M. A. Makeev, R. Cuerno, A. L. Barabasi, Nucl. Instr. and Meth. in Phys. Res. B **197**, 185 (2002).

[35] L.C. Feldman, J.W. Mayer and S.T. Picraux In: Material Analysis By Ion Channeling, Academic Press, New York (1982), p. 1.1

[36] U. Littmark, J. F. Ziegler, Handbook of Range Distributions for Energetic Ions in All Elements, Vol. 6, Pergamon Press, New York (1980).

[37] J. F. Ziegler, Handbook of Stopping Cross Sections for Energetic Ions in All Elements, Pergamon Press, 1980.

[38] M. Levalois, P. Bogadanski, and M. Toulemonde, Nucl. Instrum. Methods Phys. Res. B **63**, 14 (1992).

[39] T. Motooka, S. Harada, and M. Ishimaru, Phys. Rev. Lett.**78**, 2980 (1997).

[40] J. P. , L. G. Haggmark, The Transport and Ranges in Matter. Nucl Instrum. Meth 174, 257 (1980), Available from www.srim.org.

[41] J. F. Ziegler, J. P. Biersack, and U. Littmark. In The Stopping and Range of Ions in Matter, volume 1, New York, 1985. Pergamon.

[42] E. Rutherford, Phil. Mag. **21**, 212 (1911); ibid **21**, 699 (1911).

[43] K. B. Winterbon, P. Sigmund, J.B. Sanders, K. Dan. Vidensk. Selsk. Mat. Fys. Medd. **37**, No 14, 1970.

[44] J. Lindhard, M. Scharff, and H. E. Schoitt, Range concpet and heavy ion ranges (notes on atomic collisions II) Mat. Fys. Medd. Dan. Vidensk. Selsk. **33**, 3 (1963).

[45] L. D. Landau and E. M. Lifshitz, Electrodynamics of Continuous Media (1960).

[46] H. A. Bethe, Ann. Phys. **5**, 325 (1930).

[47] R. M. Barnett et al., Phys. Rev. D **54**, 1 (1996).

[48] S. Mantl, Nucl. Inst. Meth. Phys. Res. B, **84**, 1127 (1993).

[49] J.S. Williams, R.D. Goldberg, M.Petravic, and Z. Rao, Nucl. Inst. Meth. Phys. res. B.**84**, 199 (1994).

[50] A. Gutzmann, S. Klaumnzer and P. Meier Phys. Rev. Lett. **74**, 2256 (1995).

[51] A. Gutzmann and S. Klaumnzer Nucl. Instr. and Meth. B **127/128**, 12 (1997).

[52] J.P. Singh, R. Singh, N.C. Mishra, D. Kanjilal, and V. Ganeshan, Jour. Appl. Phys. **90** (2001) 5968.

[53] C.A. Volkert, J. Appl. Phys. **70**, 3521 (1991) and reference therein.

[54] P.C. Srivastava, V. Ganesan, and O.P. Sinha, Nucl. Instru. Methods, Phys. Res. B 222, 491 (2004).

[55] Dipak Paramanik, Asima Pradhan, and Shikha Varma, J. Appl. Phys. **99**, 014304 (2006)

[56] Dipak Paramanik and Shikha Varma, Nucl. Instr. Meth. B. **244**, 69 (2006).

[57] Dipak Paramanik and Shikha Varma, Nucl. Instr. Meth. B. **244**, 81 (2006).

[58] S. Dey, D. Paramanik, V. Ganeshan, S. Varma, Appl. Surf. Sci **253**, 1116 (2006).

[59] Dipak Paramanik and Shikha Varma, J. Nanosci. and Nanotech. **07**, 2197 (2007).

[60] Dipak Paramanik and Shikha Varma J. Appl. Phys. **101**, 023528 (2007)

[61] P. Sigmund, in Sputtering by Particle Bombardment I , R. Behrisch, ed. (Springer- Verlag: Berlin (1981)).

[62] Z.L. Liau, J.W. Mayer, W.L. Brown, J.M. Poate: J. Appl. Phys. **49**, 5295 (1978)

[63] Andersen H H and Bay H L, Radiat. Eff. **19**, 139 (1973), J. Appl. Phys. **46** 2416 (1975).

[64] Peter Sigmund, J. Mat. Sci. **8**, 1545 (1973)

[65] M. A. Makeev and A. L. Barabasi, Appl. Phys. Lett. **71**, 2800 (1997)

[66] Y. Kuramoto and T. Tsuzuki, J. Mater. Sci. **55**, 356 (1977); G. I. Sivashinsky, Acta Astronaut. **6**, 569 (1979).

[67] M. Kardar, G. Parisi, and Y.-C. Zhang, Phys. Rev. Lett. **56**, 889 (1986).

[68] E.A. Eklund, E.J. Snyder, and R.S. Williams, Surf. Sci. **285** 157 (1993).

[69] Debi Prasad Datta and Tapas Kumar Chini, Phys. Rev. B **76**, 075323 (2007),Phys. Rev. B **71**, 235308 (2005), Phys. Rev. B **69**, 235313 (2004).

[70] Z.J. Liu, N. Jiang, Y. G. Shen, Y.W. Mai, J. Appl. Phys. **92** 3559; A.E. Litand John E. Sanchez, J. Appl. Phys. **85** 876.

[71] A.L. Barabasi, H.E. Stanley, Fractal Concepts in Surface Growth, Cambridge University Press, Cambridge, 1995.

[72] F. Family, T. Vicsek (Eds.), Dynamics of Fractal Surfaces,World Scientific, Singapore, 1991.

[73] P. Meakin, Phys. Rep. 235 (1993) 189; T. Halpin-Healey, Y.-C. Zhang, Phys. Rep. **254**, 215 (1995).

[74] F. Family and T. Vicsek J. Phys. A **18**, L15 (1985).

Chapter 2

Experimental techniques

2.1 Ion irradiation techniques

This chapter briefly discusses the ion implantation facilities and setups that were utilized in sample preparations. In this thesis InP(111) single crystals were ion irradiated at 1.5 MeV and 3 keV. MeV ion irradiation was performed by utilizing the ion accelerator Pelletron facility whereas for 3 keV ion irradiation, an ion gun facility was utilized. Following the ion irradiations, InP sample were characterized for modifications of their surfaces and bulk properties. Several techniques like Scanning Probe Microscopy(SPM), X-ray Photo electron Spectroscopy (XPS), Raman scattering etc. were utilized for these characterizations. These techniques are also briefly discussed in the following sections.

2.1.1 MeV ion irradiation-implantation

The MeV ion irradiation experiments, investigated in this thesis, have been done using the 3 MV tandem Pelletron Accelerator (9SDH2, NEC, USA) facility at our institute which has been schematically shown in fig. 2.1. The accelerator is an upgraded version of electrostatic Van de Graff generator. The accelerator is housed in a steel pressure vessel, which is pressurized with sulphur hexafluride (SF_6) insulating gas during operation. The machine is equipped with two ion sources - one RF ion source (Alphatross) used for providing He, H and a multi-cathode SNICS (source of negative ions by cesium sputtering) for providing almost all other elements in the periodic table except inert gas ions.

Negative ion beams produced from the ion source are pre-accelerated upto a maximum of 70 keV energy before being injected in to the machine. The beam enters through the low energy end of the accelerator where the negative ions are attracted to the positively charged high voltage terminal and are thus accelerated. At the terminal, they are charge stripped by passing them through a gas stripper system and converted into positive ions. As the positive ions exit the stripper and drift into the second stage of the accelerator, they are repelled by the high voltage terminal and thus accelerated once again. This dual acceleration gives the singly charged ions twice the energy. If the negative ions are injected with an initial energy of E' and the terminal potential is V, then the ion energy at the end of the terminal will be:

$$E = [E' + (1 + q)V] \tag{2.1}$$

where q is the charge state of the ion after stripping. On the high energy side there is a 90^0 analyzing magnet for selecting the desired ions with right energy. A switching magnet finally puts the ions into the desired beam-lines. There are six beam lines with the accelerator. The first one (45^0) is a general purpose beam line for carrying out RBS/channeling, PIXE, NRA experiments. The second one developed in $+15^0$ beam-line is for carrying out C^{14} AMS measurements. The zero degree beam-line is used for low energy atomic and nuclear physics experiments. The -15^0 beam-line is dedicated for ion implantation. At the -30^0 beam-line, facilities for carrying out surface physics experiments have been developed. The micro-beam facility has been developed at the -45^0 beam-line.

The Pelletron facility, discussed above, was utilized to prepare MeV implanted

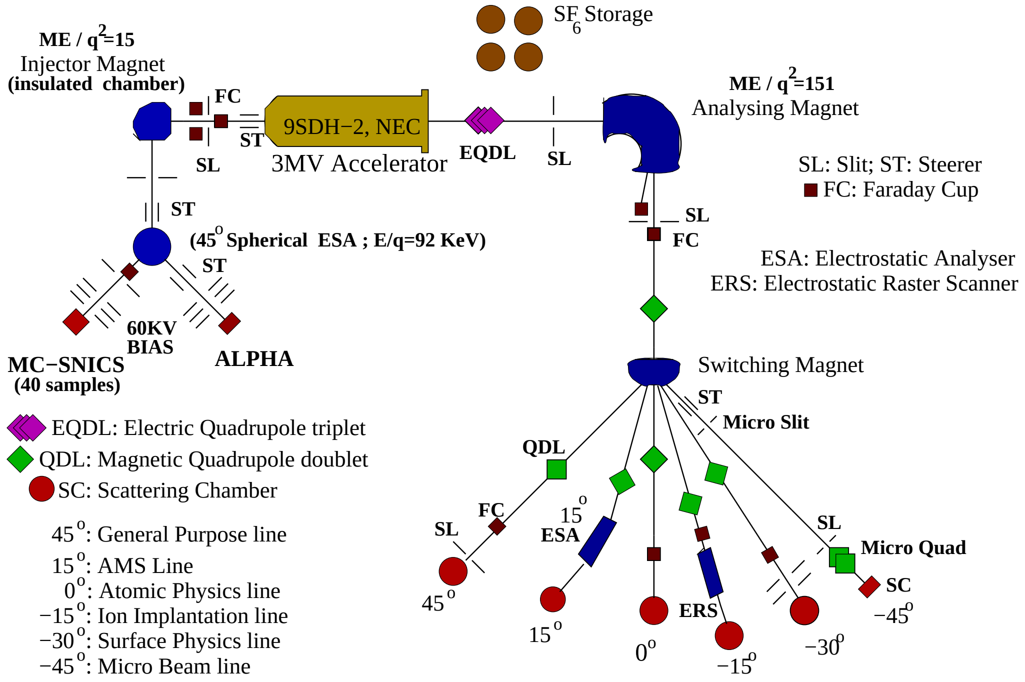

Figure 2.1: Schematic diagram of the 3 MV tandem Pelletron accelerator along with various beamlines.

InP(111) samples. The samples were implanted at room temperature with a scanned beam of 1.5 MeV Sb^{2+} ions at various fluences ranging from 1×10^{11} to $5\times10^{15} ions/cm^2$. The beam was scanned over a square area of 0.5 cm $\times$ 0.5 cm on the sample surface. The average Sb flux was 0.02 μA/cm^2. This current was measured directly on the target after suppressing the secondary electrons by applying a negative bias of 200V to a suppressor assembly around the target. The implantations were performed with the samples oriented 7^o off-normal to the incident beam to avoid channeling effects. The implantations were carried out in a high vacuum ($\sim 1\times10^{-7}$ mbar) chamber located in the -15^0 beam line. This chamber is equipped with a raster scanner, operating at 517 Hz and 64 Hz in the horizontal and vertical directions, respectively, for achieving uniformly implanted regions.

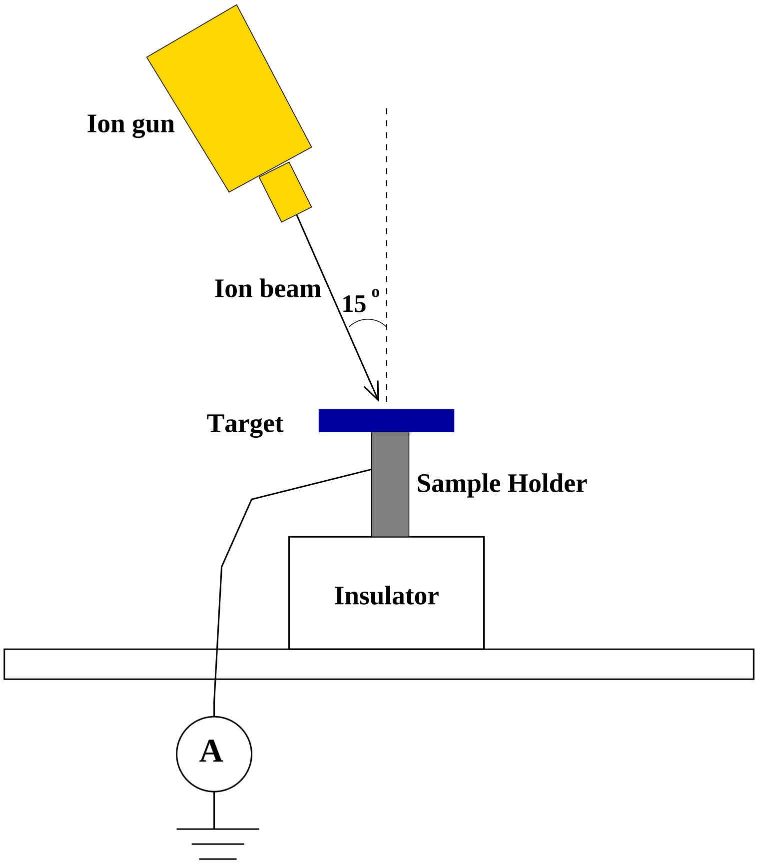

Figure 2.2: Schematic diagram for low energy ion erosion.

2.1.2 keV ion irradiation-sputtering

Low energy (keV) ion irradiation of InP(111) samples was performed by utilizing an argon ion gun(model EX03) facility. Schematic diagram of the sputtering setup is shown in fig. 2.2. The EX03 ion gun (from Thermo Scientific) is an electron impact source designed for surface preparation in surface analysis experiments and is intended for use with inert gas species. The energy range of the gun is 300 eV to 3 keV. The ion gun can produce an adjustable low current (1 to 10μA) ion beam. Ions are created in the source region of the gun where high purity(99.99%) Ar gas is introduced through an auxiliary gas inlet. A source current is run through a refractory oxide filament to produce electrons for impact ionization of the neutral gas. The source region of the ion gun was connected to an open port on the vacuum chamber through a tube to provide extra pumping capability in this part of the ion gun. The ions are extracted from the source region and focused using a zoom lens consisting of a series of electrostatic elements that can be individually set to various voltages in order to adjust the spot size and current density of the beam.

Using this facility, InP(111) single crystals were irradiated with 3 keV Ar ions. Irradiations were performed at room temperature at an incidence angle of 15°, with respect to the sample surface normal. Several sets of InP(111) single crystal surfaces were irradiated for 5 to 80 minutes with a low ion flux of $1 \times 10^{13}\ cm^{-2}s^{-1}$. The beam was scanned over a circular area of 0.3 cm diameeter on the sample surface. During the experiment the vacuum in the chamber was $\sim 1 \times 10^{-7}$ mbar. The vacuum was produced using a 70 l/sec turbo molecular pump and a rotary pump.

2.2 Sample characterization techniques

The techniques that have been utilized to characterize the ion irradiated samples will be briefly discussed in the following sections.

2.2.1 Scanning Probe Microscopy(SPM)

SPM is a family of microscopy techniques that forms images of surfaces using a physical probe that scans the specimen. An image of the surface is obtained by mechanically moving the probe in a raster scan,line by line, and recording the probe-surface interaction as a function of position. Many scanning probe microscopes can image several interactions(tunnelling current, inter-atomic force, magenetic force, electric force, frictional force) simultaneously. Scanning Tunneling Microscopy (STM), the first of the SPM techniques was invented in 1981 by G. Binnig and H. Rohrer[1, 2]. Sub-atomic resolution was achieved and the Nobel Prize was awarded for their work in

1986. The first and most important extension of STM is the Atomic Force Microscopy (AFM), invented in 1986 by G. Binnig, C. Quate, and C. Gerber [3]. This technique allowed for the surface characterization of conductive as well as non-conductive samples. AFM can provide 2-D as well as 3-D images of the surfaces with atomic resolutions. All this makes AFM a very attractive tool for research.

AFM is able to measure small variations in surface topography by measuring the deflection of a tip on the end of a cantilever beam, as the sample surface is rastered below the tip. The tip is located at the free end of a cantilever that is 100 to 200 μm long. The tip is typically made of silicon or silicon nitride. Silicon nitride tips exhibit excellent flexibility, making them easier to use than stiffer silicon tips. Silicon tip is used in tapping mode AFM whereas in contact-AFM silicon nitride tips are used. The radius of curvature of the tip is between 10 and 50 nm. A laser is focused on to the tip of a highly reflective cantilever beam such that the laser is reflected onto the surface of a position-sensitive photo-detector. The sample is rastered underneath the tip via a piezoelectric scanner made of PZT (Lead Zirconium Titanate) compound. A feedback loop is used to maintain either a constant deflection (contact mode) or oscillatory amplitude (tapping mode) of the cantilever. A schematic view of an AFM system is shown in fig 2.3. The AFM can be operated in two basic modes: with feedback control or without the feedback control. If the electronic feedback is *switched on* then the positioning piezo(scanner) that moves the sample up and down, can respond to any change in force, which is detected, and alter the tip-sample separation to restore the force to a pre-determined value. This mode of operation, known as constant force, usually enables a fairly faithful topographical image to be obtained. If the feedback electronics is *switched off*, then the microscope is said to be operating in constant height or deflection mode. This is particularly useful for imaging very flat samples at high resolution.

The force most commonly associated with atomic force microscopy is the interatomic van der Waals force. The dependence of the van der Waals force upon the

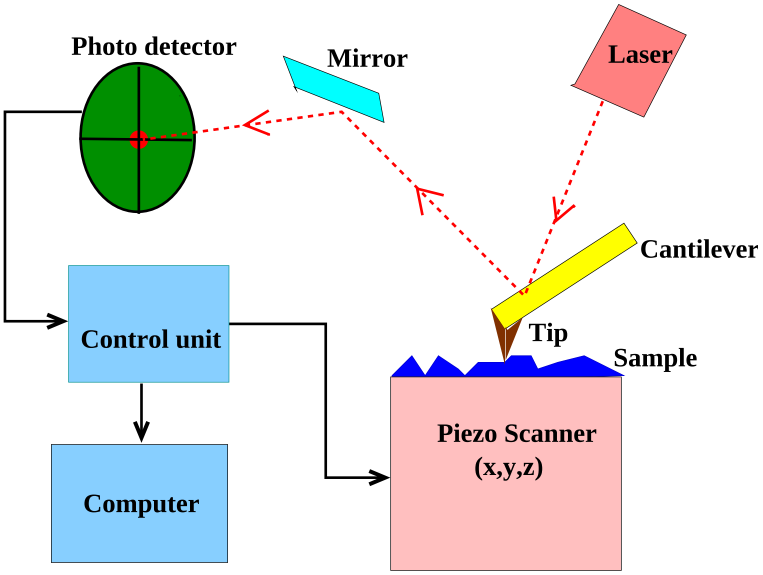

Figure 2.3: A schematic diagram of atomic force microscopy

distance between the tip and the sample is shown in fig. 2.4. Two distance regimes are labeled in fig. 2.4 : the contact regime; and the non-contact regime. In the contact regime, the cantilever is held less than a few $\mathring{A}$ from the sample surface, and the inter-atomic force between the cantilever and the sample is repulsive in nature. In the non-contact regime, the cantilever is held about tens to hundreds of angstroms away from the sample surface, and the inter-atomic force between the cantilever and the sample is attractive (largely a result of the long-range van der Waals interactions).

There are mainly three scanning modes used in AFM. These are contact, non-contact and tapping modes:

(i) **Contact or repulsive mode :** In contact-AFM mode, also known as repulsive mode, an AFM tip makes soft 'physical contact' with the sample. The tip is attached to the end of a cantilever with a low spring constant, lower than the effective spring constant holding the atoms of the sample together. As the scanner gently traces the tip across the sample (or the sample under the tip), the contact force causes the cantilever to bend to accommodate changes in the topography. This mode is

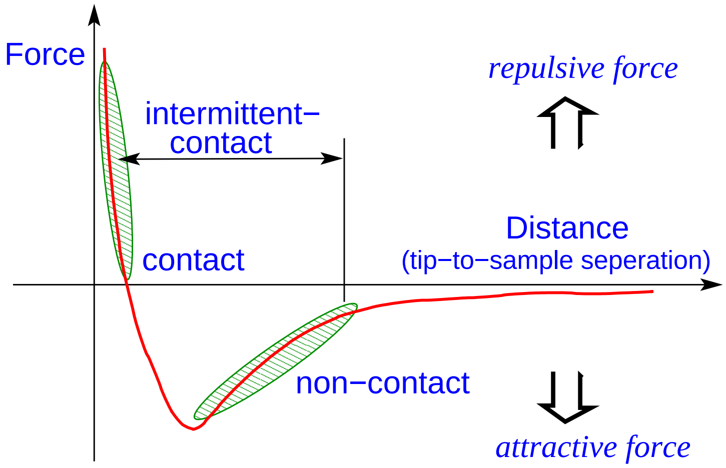

Figure 2.4: Inter-atomic force vs. distance

usually applied on the hard crystalline surfaces with atomic or molecular resolution, but it is not suitable for biological samples where this force is strong enough to cause deformations.

(ii) **Non-contact or attractive mode :**

Non-contact AFM is one of several vibrating cantilever techniques in which an AFM cantilever is vibrated near the surface of a sample. The spacing between the tip and the sample is of the order of tens to hundreds of angstroms. In this mode, the tip is at a distance from the sample surface where the attractive Van der Waals forces dominate. The major advantage of the non-contact mode AFM is its truly non-invasive character. This mode is suitable for biological samples or soft samples.

(iii) **Tapping mode :**

This technique allows high resolution topographic imaging of sample surfaces that are easily damaged, loosely held to their substrate, or difficult to image by other AFM techniques. Tapping mode overcomes problems associated with friction, adhesion, electrostatic forces, and other difficulties that can plague conventional AFM scanning methods by alternately placing the tip in contact with the surface to provide high resolution and then lifting the tip off the surface to avoid dragging the tip across the surface. Tapping mode imaging is implemented in ambient air by oscillating the cantilever assembly at or near the cantilever's resonant frequency using a piezoelectric crystal. The piezo motion causes the cantilever to oscillate with a high amplitude(typically greater than 20nm) when the tip is not in contact with the surface. The oscillating tip is then moved toward the surface until it begins to lightly touch, or tap the surface. During scanning, the vertically oscillating tip alternately contacts the surface and lifts off, generally at a frequency of 50,000 to 500,000 cycles per second. As the oscillating cantilever begins to intermittently contact the surface, the cantilever oscillation is necessarily reduced due to energy loss caused by the tip contacting the surface. The reduction in oscillation amplitude is used to identify and measure surface features.

During tapping mode operation, the cantilever oscillation amplitude is maintained constant by a feedback loop. Selection of the optimal oscillation frequency is software-assisted and the force on the sample is automatically set and maintained at the lowest possible level. When the tip passes over a bump in the surface, the cantilever has less room to oscillate and the amplitude of oscillation decreases. Conversely, when the tip passes over a depression, the cantilever has more room to oscillate and the amplitude increases (approaching the maximum free air amplitude). The oscillation amplitude of the tip is measured by the detector and input to the controller electronics. The digital feedback loop then adjusts the tip-sample separation to maintain a constant amplitude and force on the sample.

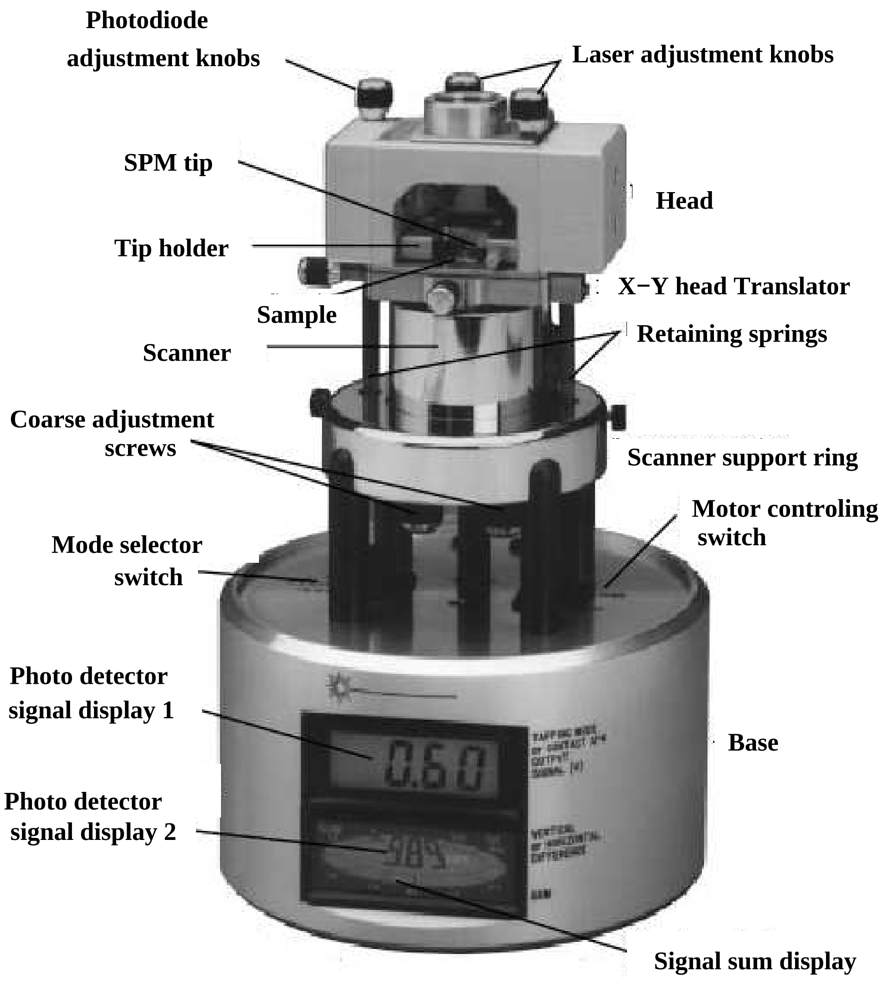

Figure 2.5: Multi mode SPM in our laboratory

In the present thesis, the surface morphologies of the MeV and keV ion irradiated InP(111) surfaces were investigated using a multi mode SPM(fig. 2.5) with Nanoscope IIIa controller from Digital Instrument (Veeco). All the reported SPM images have been acquired with constant force mode in tapping mode by utilizing the silicon probes. The Nanoscope software was used for the analysis of the SPM images.

2.2.2 X-ray Photoelectron Spectroscopy (XPS)

XPS is also known as ESCA, an abbreviation for Electron Spectroscopy for Chemical Analysis. First working XPS system was developed by Kai Siegbahn and his group in Sweden in 1954. It is a widely used method to determine[4, 5, 6, 7]:

- Elemental composition of the surface (110 nm usually)
- Empirical formula of pure materials
- Elements that contaminate a surface
- Chemical or electronic state of each element in the outermost layers
- Uniformity of elemental composition across the top surface (line profiling or mapping)
- Uniformity of elemental composition as a function of ion beam etching (depth profiling)

The technique works on the photoelectric effect discovered by Heinrich Rudolf Hertz in 1887.

The core electrons of atoms have characteristic binding energies. When an X-ray beam is incident on the sample surface, the energy of an X-ray photon may be adsorbed completely by a core or valence electron of an atom (fig. 2.6). If the photon energy, hν, is larger than the electron binding energy, then the electron will escape from the atom and be emitted out of the surface. The emitted electron with the kinetic energy E_K is referred to as the photoelectron. The binding energy (E_B) of the core electron is given by the Einstein relationship:

$$E_B = h\nu - E_K - \phi \tag{2.2}$$

where $h\nu$ (h being the Plank's constant and ν being the frequency of the radiation) is the X-ray photon energy, E_K is the kinetic energy of photoeletron, and ϕ is the spectrometer work function.

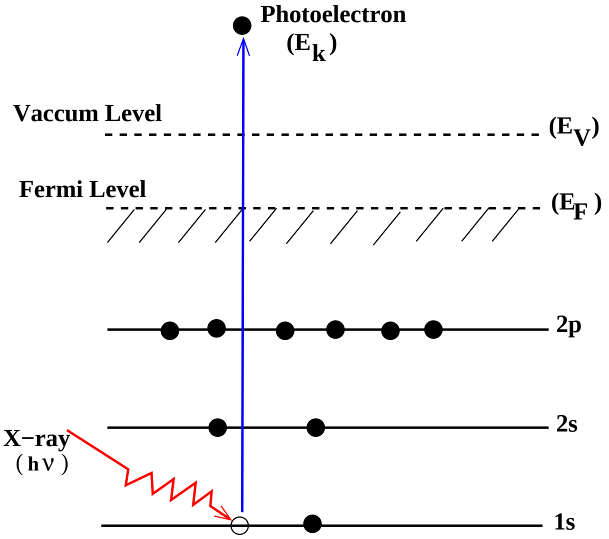

Figure 2.6: Schematic diagram of core level x-ray photoelectron emission process.

The kinetic energy of the escaping photoelectrons limits the depth from which they can emerge, giving XPS its high surface sensitivity and sampling depth of a few nanometers (usually upto 10 nm). Since the number of photoelectron of an element is dependent upon the atomic concentration of that element in the sample, XPS is used not only to identify the elements but also to quantify the chemical composition. After the value of peak intensity (the peak area after background removal) is obtained, the atomic concentration of an element, C_i, can be expressed as:

$$C_i = \frac{\frac{I_i}{S_i}}{\sum_i \frac{I_i}{S_i}} \tag{2.3}$$

where I_i is the peak intensity for element i, and S_i is the atomic sensitivity factor for the peak i.

XPS instruments consist of an x-ray source, an energy analyzer for the photoelectrons, and an electron detector. The analysis and detection of photoelectrons requires that the sample be placed in a high-vacuum chamber. An electrostatic analyzer analyzes the energy of the photoelectrons, and an electron multiplier tube or a

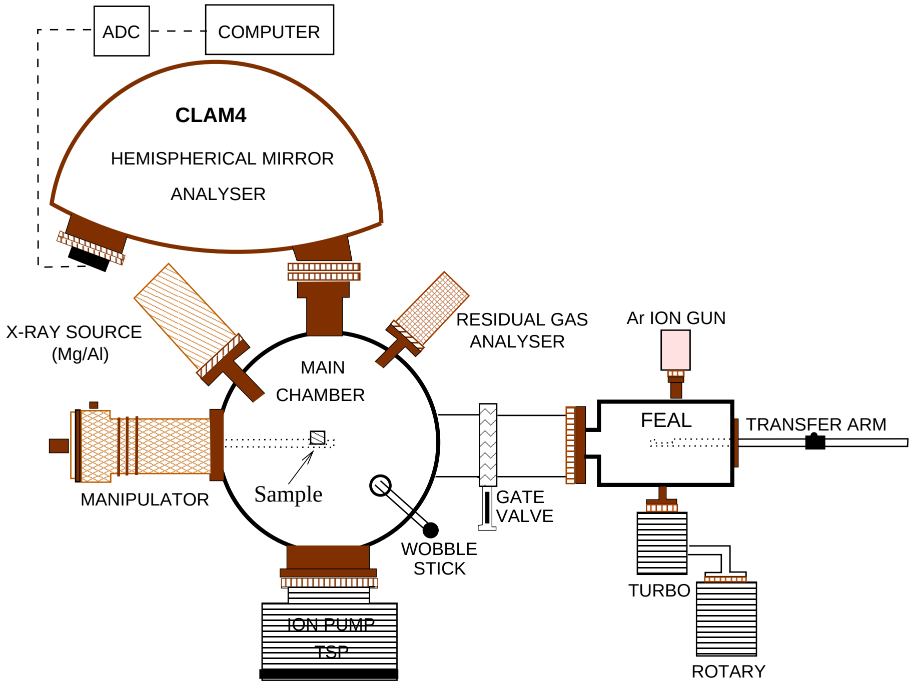

Figure 2.7: Schematic diagram of the XPS System in our laboratory.

multichannel detector (channeltron) such as a micro channel plate detects the photoelectrons.

XPS measurements, in the present thesis work, were performed using a VG system (fig. 2.7) with a base pressure of $\sim\ 1 \times 10^{-10}\, Torr$. The XPS system is equipped with dual Mg-Al anodes, a hemispherical analyzer and a channeltron. Non-monochromatic Mg K_α (1253.6 eV) radiation was used at 300 Watt for all the XPS measurements reported here. The analyzer was operated with a pass energy of 200 eV for large size survey scans of 0-1000 eV. For high resolution scans a pass energy of 20 eV was utilized. The instrumental resolution is about 0.9 eV. Data were acquired at a take-off angle, that is, the angle between the sample normal and the analyzer axis, of 30^0. Peak positions of the collected spectra were referenced to the binding energy of adventitious Carbon 1s peak at 284.6 eV. Background (Shirley) subtraction and curve fitting of the collected spectra was performed using the VGX-900 software supplied with the system.

2.2.3 Raman spectroscopy

Raman spectroscopy is a versatile, convenient, non-destructive characterization tool widely used in the field of semiconductors. Since it probes lattice vibrations, which are sensitive to internal and external perturbations, it can be used to study the composition, phase, crystallinity, crystal orientation, and in some cases doping, in semiconductors. An important aspect of Raman spectroscopy is its ability to determine the changes in the vibrational frequencies induced by the microstructures and/or by the strain in the lattice[8, 9]. Thus it is a very useful tool for studying structural modifications in semiconductors after ion irradiation[10, 11]. Micro-Raman spectroscopy, where the light of the exciting laser is focused on the sample through a microscope, is especially very useful for microelectronics devices with small dimensions as it allows investigation with micron spatial resolution.

Raman spectroscopy is inelastic light scattering technique used to diagnose the internal structure of molecules and crystals [8, 9]. The light of a known frequency and polarization is scattered from a sample. The majority of the scattered photons have the same frequency as incident photons and are known as Raleigh scatter. The Raman scattered photons (very small fraction approximately 1 in 10^7 of incident photons) have frequencies shifted from the incident photons by the energies of molecular vibrations. The magnitude of the shift is independent of the excitation frequency. This "Raman shift" is therefore an intrinsic property of the sample.

Most of the Raman scattered photons are shifted to longer wavelengths (Stokes shift), but a small portion is shifted to shorter wavelengths (anti-Stokes shift). Figure 2.8 shows a diagram of Rayleigh scattering, Stokes Raman scattering, and anti-Stokes Raman scattering. In each case, the incident photon excites an electron into a higher virtual energy level and then the electron decays back to a lower level, emitting a scattered photon. In Rayleigh scattering the electron decays back to the same

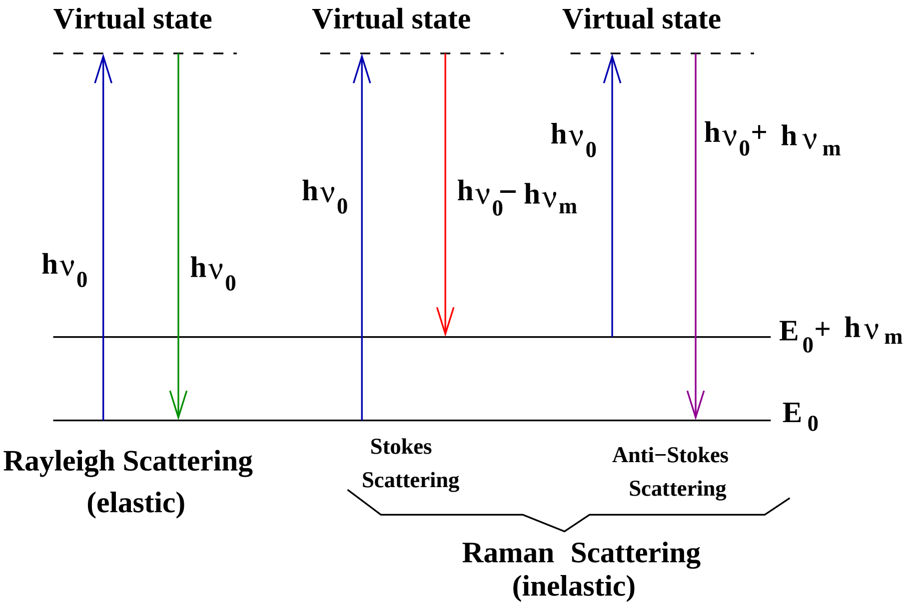

Figure 2.8: Energy level diagram demonstrating Raleigh and Raman (Stokes and Anti-Stokes) scattering of photons.

vibrational level from which it started. Stokes Raman scattering occurs when the final energy level is higher than the initial level, while anti-Stokes Raman scattering occurs when the final energy level is lower than the starting level. Stokes scattering is much more common than anti-Stokes scattering because at any given time an electron is most likely to be in its lowest energy state at room temperature, in accordance with the Boltzmann distribution. Only Stokes Raman scattering is commonly used in spectroscopy.

Here we shall briefly discuss the theory [12, 13, 14, 15] involved in explaining Raman spectra from lower dimensional systems. Let us consider the wave function of a phonon of wave vector $\mathbf{q_0}$ in an infinite crystal :

$$\Phi(\mathbf{q_0}, \mathbf{r}) = u(\mathbf{q_0}, \mathbf{r}) e^{i\mathbf{q_0}\cdot\mathbf{r}} \tag{2.4}$$

where $u(\mathbf{q_0}, \mathbf{r})$ has the periodicity of the lattice. Now, we confine this phonon to a sphere of diameter L. The phonon confinement changes the phonon wave function to

$$\Psi(\mathbf{q_0}, \mathbf{r}) = W(\mathbf{r}, L)\Phi(\mathbf{q_0}, \mathbf{r}) = \Psi'(\mathbf{q_0}, \mathbf{r}) u(\mathbf{q_0}, \mathbf{r}) \tag{2.5}$$

where $W(\mathbf{r}, L)$ is the phonon weighting function such that

$$|\Psi(\mathbf{q_0}, \mathbf{r})|^2 = |W(\mathbf{r}, L)|^2 \tag{2.6}$$

It is clear that $W(\mathbf{r}, L)$ describes the phonon confinement, although many functions can accomplish it. To calculate the Raman spectra, we first expand $\Psi'(\mathbf{q_0}, \mathbf{r})$ in a Fourier series :

$$\Psi'(\mathbf{q_0}, \mathbf{r}) = \int C(\mathbf{q_0}, \mathbf{q}) e^{i\mathbf{q}.\mathbf{r}} d^3q \tag{2.7}$$

with Fourier coefficients $C(\mathbf{q_0}, \mathbf{q})$ obtained from

$$C(\mathbf{q_0}, \mathbf{q}) = \frac{1}{(2\pi)^3} \int \Psi'(\mathbf{q_0}, \mathbf{r}) e^{-i\mathbf{q}.\mathbf{r}} d^3r \tag{2.8}$$

The nanocrystal phonon wave function is a superposition of eigenfunctions with $\mathbf{q}$ vectors centered at $\mathbf{q_0}$. Thus, the first-order Raman spectrum $I(\omega)$ is given by

$$I(\omega) = \int \frac{|C(\mathbf{0}, \mathbf{q})|^2 d^3q}{[\omega - \omega(\mathbf{q})]^2 + (\Gamma_0/2)^2} \tag{2.9}$$

where $\omega(\mathbf{q})$ is the phonon dispersion curve, Γ_0 is the natural line width of the curve, $\mathbf{q_0} = 0$, which is appropriate for first-order Raman scattering, and the integration must be performed over the entire Brillouin zone.

In order to carry out numerical calculations one has to write suitable functions of phonon confinement $W(\mathbf{r}, L)$ and phonon dispersion $\omega(\mathbf{q})$.

For the case of semiconductors such as InP, ZnTe, and for spherical nanocrystallites, Kagaya and Borcherds [16, 17] have investigated the influence of the choice of $W(\mathbf{r}, L)$ on the quality of the fit between theory and experiments. They considered three types of functions, given below together with their Fourier coefficients :

$$W(\mathbf{r},L) = \frac{sin(2\pi r/L)}{2\pi r/L}, \qquad |C(0, \mathbf{q})|^2 \approx \frac{sin^2(qL/2)}{(4\pi^2 - q^2L^2)^2} \tag{2.10}$$

$$W(\mathbf{r},L) = exp(-4\pi^2 r/L), \qquad |C(0, \mathbf{q})|^2 \approx \frac{1}{(16\pi^4 - q^2L^2)^4} \tag{2.11}$$

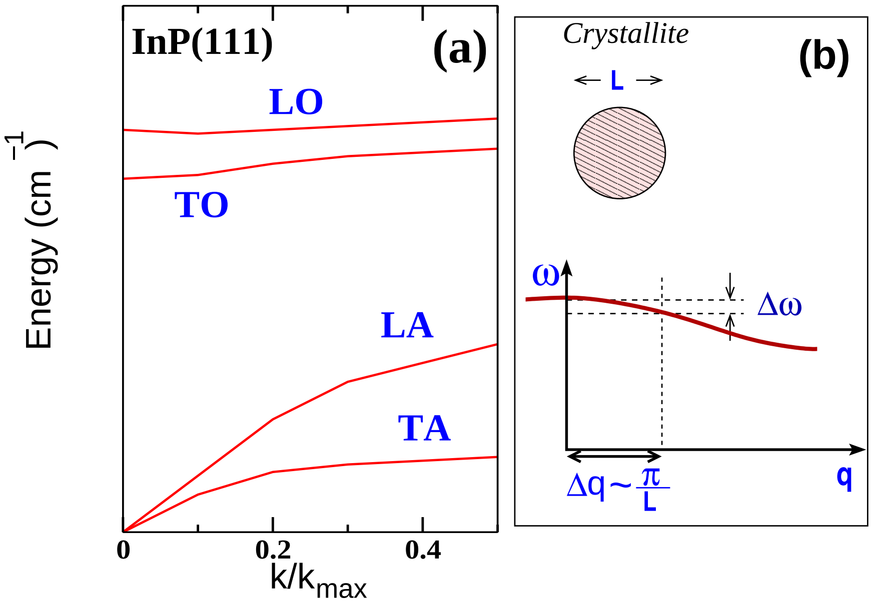

Figure 2.9: **(a)** Dispersion curves of InP in the direction of (111) axis. **(b)** Confinement of phonon due to finite size **L** of the crystallite of InP. Adapted from Reference[16, 17].

$$W(\mathbf{r},L) = exp(-8\pi^2 r^2/L^2), \qquad |C(0,\mathbf{q})|^2 \approx exp(\frac{-q^2L^2}{16\pi^2}) \tag{2.12}$$

The first confinement function, eqn. 2.10, was chosen by analogy with the ground state of an electron confined to a hard sphere. The amplitude of the phonon is zero at the boundary. The second confinement function, eqn. 2.11, which can be written as $exp(-\alpha r)$, was chosen by analogy with a wave in a lossy medium. The third confinement function, eqn. 2.12, which can be written as $exp(-\alpha r^2/L^2)$, was chosen in anticipation of the size distribution and in agreement with Nemanich et al. [14] and Richter et al. [15]. With this equation, the phonon is confined very strongly to the nanocrystal, since W($\mathbf{r}$ = L/2, L) is very small.

The phonon dispersion relation $\omega(\mathbf{q})$ is taken as :

$$\omega(\mathbf{q}) = \omega_p - A(\frac{\mathbf{q}}{\mathbf{q_0}})^2 \tag{2.13}$$

where $q_0 = \frac{2\pi}{a_0}$, a_0 is the lattice constant, ω_p corresponds to the phonon energy at q

= 0 and A is a constant. According to Richter [12], the final result is not critically dependent on the form of the dispersion relation, as long as $\omega(q)$ is parabolic near the center of the Brillouin zone. The value of the constant A can be determined by fitting the available neutron data of phonon dispersion for different crystals to eqn. 2.14 .

Let us discuss the results for nanocrystalline-InP (nc-InP) and bulk crystalline-InP (c-InP). Since the agreement with experimental results is good only for Gaussian confinement [15], we use eqn. 2.13 as the confinement function. eqn. 2.10 can now be rewritten as

$$I(\omega) = \int_0^{\frac{2\pi}{a_0}} \frac{exp(\frac{-q^2L^2}{16\pi^2})4\pi q^2 dq}{(\omega - \omega(\mathbf{q}))^2 + (\Gamma_0/2)^2} \tag{2.14}$$

For bulk InP single crystal, the lattice constant $a_0 = 5.58$ Å. To calculate the line shape, we have taken the natural line width $\Gamma_0 = 7.6$ cm^{-1}, and the phonon energy(at q = 0) $\omega_p = 350.0$ cm^{-1} [17] (discussed later in Chapter 5). The value of the constant A has been chosen as 68 [17]. These parameters reproduce the dispersion relation for the longitudinal optical (LO) phonons along [111] direction in InP well. Dispersion curves for InP along the (111) direction have been shown in fig. 2.9.

As illustrated in fig. 2.10 three parameters are generally used to describe the Raman line shape quantitatively. These are the shift ($\Delta\omega$) in central InP-peak frequency with respect to the peak of bulk crystalline InP, the full width at half maximum (Γ) of c-InP (FWHM), and the ratio (Γ_a/Γ_b) of the half width at half maximum (HWHM) on the low energy side(Γ_a) to the HWHM on the high energy side (Γ_b).

The evolution of the Raman line using eqn. 2.14, as a function of decreasing size (L) for spherical InP nanocrystallites is shown in fig. 2.9. From this figure, it is clear that the size affects the Raman spectra corresponding to bulk crystalline InP and makes the curve asymmetric ($\Gamma_a/\Gamma_b \neq 1$) and shifts ($\Delta\omega$) the peak towards lower or higher energy side depending on the nature of the dispersion curve. Hence from a set of experimental Raman data, the Γ_a/Γ_b value provides the degree of crystallinity of the sample. If there is a stress in the sample, it may alter $\Delta\omega$ [18, 19]. From the sign ($\pm$) and the value of $\Delta\omega$, it is possible to measure the type and magnitude of the

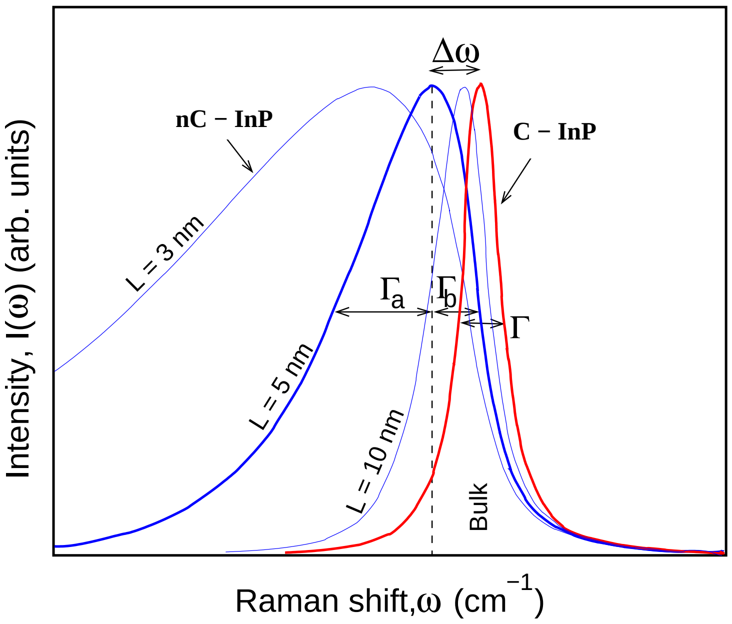

Figure 2.10: Theoretical Raman spectra for bulk crystalline InP (c-InP) and nanocrystalline InP (nc-InP) where $\Delta\omega$, Γ, Γ_a and Γ_b are shown. The evolution of Raman line-shape, as a function of decreasing coherence length, L is shown. Note the apparent downward shift in peak position which accompanies the skewing of the Raman peak as L decreases. Line shapes have been obtained using eqn. 2.14.

stress. In case of shift to lower energy (red shift), the stress is tensile and for shift to higher energy (blue shift), the strain is compressive. So the shift ($\Delta\omega$) may be because of two effects : grain size and stress. The only difference between these two effects is – grain size effects make the Raman spectra asymmetric but the stress effects leave the curve symmetric. In addition, Campbell and Fauchet[20] have suggested that the two phonon Raman spectrum could be used in conjunction with the one phonon Raman spectrum to distinguish the effect of stress from that of crystal size because stress and crystal size affect these two types of processes differently. Among the other factors, a wide size and strain distribution and surface effects play an important role to alter the Γ, Γ_a/Γ_b and $\Delta\omega$.

In the present study, Raman spectroscopy has been performed in the 180^0 backscattering geometry at room temperature. The schematic diagram in fig. 2.11 shows the

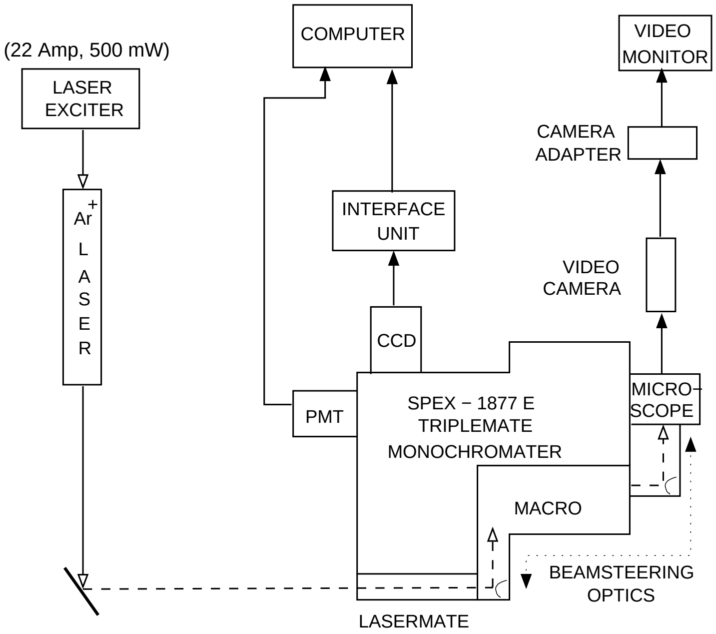

Figure 2.11: Schematic block diagram of the Raman setup with 180^0 scattering configuration

Raman set-up with 180^0 scattering configuration. The experimental set-up for Raman measurements mainly consists of :

- **Excitation source :** Spectra Physics 5 Watt (all line) Ar^+ laser.
- **Spectrometer :** Spex 1877 E Triplemate with two scattering configurations (90^0 and 180^0 geometries).
- **Detection system :** Charged coupled device (CCD) and photo-multiplier detector.

Bibliography

[1] G. Binning, H. Rohrer: " Scanning tunneling microscopy", Helv. Phys. Acta **55**, 726 (1982)

[2] G. Binning, H. Rohrer, Ch. Gerber, and E. Weibel:"7×7 reconstruction on Si(111) resolved in real space" Phys. Rev. Lett. **50**(2), 120 (1983)

[3] G. Binnig, C. F. Quate and Ch. Gerber, Phys. Rev. Lett. **56**, 930 (1986).

[4] Handbook of X-ray photoelectron spectroscopy, edited by C. D. Wagner, W. M. Rigs, L. E. Davis, J. F. Moulder, and G. E. Muilenberg (Perkin-Elmer, Eden Prairie, MN, 1978).

[5] V. I. Nefedov, X-ray Photoelectron Spectroscopy of Solid Surfaces, (Brill-VSP Pulishers, 1988), Physics at surfaces edited by Andrew Zangwill (Cambridge University Press, 1988)

[6] Practical Surface Analysis - Auger and X-ray Photoelectron Spectroscopy edited by D. Briggs and M. P. Seah (Wiley Interscience, 1990), An introduction to surface analysis by XPS and AES edited by John F. Watts, John Wolstenholme (Wiley Interscience, 2003)

[7] T. A. Carlson, X-ray Photoelectron Spectroscopy, Academic Press, 1978

[8] I. R. Lewis, H. G. M. Edwards, Handbook of Raman Spectroscopy Marcel Dekker, New York, 2001.

[9] Characterization of Materials, edited by E. N. Kaufmann, (John-Wiley & Sons Publications, 2003).

[10] Dipak Paramanik and Shikha Varma, J. Nanosci. and Nanotech. **07**, 2197 (2007).

[11] Dipak Paramanik and Shikha Varma, J. Appl. Phys. **101**, 023528 (2007).

[12] H. Richter, Z. P. Wang and L. Ley, Solid State Commun. **39**, 625 (1981).

[13] R. J. Nemanich and S. A. Solin, Phys. Rev. **B20**, 392 (1979).

[14] R. J. Nemanich, S. A. Solin and R. M. Martin, Phys. Rev. **B23**, 6348 (1981).

[15] P. M. Fauchet and I. H. Campbell, CRC Crit. Rev. Solid State Mater. Sci. **14**, S79 (1988).

[16] H. Kagaya, T. Soma, physica status solidi. B. **121**, K113, (1984).

[17] P. H. Borcherds, G F Alfrey, A. D. B. Woods and D. H. Saunderson J. Phys. C: Solid State Phys. **8**, 2022 (1975).

[18] E. Anastassakis, A. Pinczuk, E. Burstein, F. H. Pollak and M. Cardona, Solid State Commun. **8**, (1970), 133.

[19] M.J. Seong, O.I. Micic, A.J. Nozik and A. Mascarenhas, and H.M. Cheong, Appl. Phys. Lett. **82**, 185 (2003).

[20] H. Campbell and P. M. Fauchet, Solid State Comm. 58, 739 (1986)

Chapter 3

Nano-Pattern formation and Surface Modifications after keV Irradiation on InP(111)

3.1 Introduction

Patterning of regular nano dot arrays on semiconductor surfaces is of immense importance due to their potential applications in optoelectronic, photonic and recording media[1]. Fabrication of nano-dots through self-organization induced by ion irradiation processes has attracted special interest due to the possibility of production of regular arrays of dots on large areas in a single technological step. The pattern formation is related to the surface instability between curvature dependant ion sputtering that roughens the surface and smoothening by different relaxation mechanisms [2, 3, 4, 5]. Recently it was observed that self organized nano dot patterns can evolve from low energy ion sputtering of III-V semiconductor surfaces. This patterning is mostly performed either under normal incidence conditions [5, 6, 7] or in off-normal geometry coupled with rotation [8, 9]. Generally for off-normal ion incidence, without sample rotation, a periodic height modulation in the form of ripple or wave like structure, with sub-micron length scale, develops during ion bombardment as observed for single crystalline III-V semiconductors [10, 11]. During this patterning, however, along with nano dot fabrication the surface also undergoes structural modifications due to ion sputtering. Although these surface modifications have not received much attention, they are important for understanding the parameters influencing the nanodots as well as their evolution.

Here, in this chapter, a detailed investigation on the temporal evolution and the coarsening behaviour of InP nano dots in conjunction with the structural modifications occurring on the InP(111) surface have been presented. The dots have been fabricated by 3 keV Ar^+ ion sputtering under off-normal geometry but in the absence of rotation. These nano-structures are produced over a wide temporal range of sputtering time spanning from 5 min to 80 min, with a low ion flux of 1×10^{13} $ions\ cm^{-2}\ s^{-1}$. A detailed investigation of these nano-structures has been done by SPM. The average size and height of the nano-structures varies in the range of 10 to 100 nm and 5 to 40 nm, respectively, for different sputtering times. A high density of nano-dots, with narrow size and height distributions, is found for 10 minutes of sputtering. These nano-dots exhibit a weak short range ordering. The nano-structures develop in the early stages of sputtering and coarsen in size and height with increasing time upto a critical time (t_c). Beyond t_c (= 40 min), however, an inverse coarsening and fragmentation of the nano-dots is seen. During this nano dot formation, by ion beam irradiation, the surface undergoes several modifications. The value of rms surface roughness increases upto t_c but decreases for longer sputtering durations. To understand the nature of the surface modifications and to compare these observations with the existing theoretical models, roughness exponent (α) and the growth exponent (β) have been measured using SPM images. Raman Scattering results show that during the coarsening of nano-dots, in addition to other modifications, the surface also experiences an increased tensile stress. For higher sputtering durations, surface amorphization is observed. This leads to the inverse-coarsening and fragmentation of the dots. Consequently, relaxation in the stress, by Raman scattering results, as well as smoothening of surface, by SPM technique, are observed.

The technique of X-ray Photoelectron Spectroscopy (XPS) has been utilized to understand the chemical stoichiometric modifications occurring on the InP surfaces during 3 keV ion irradiation. Results show the shift of In(3d)and P(2p) core levels towards the higher binding energy. These shifts have been related to the nano-dots formation. Moreover, an excess In concentration compared to P atoms is also seen. This leads to In -rich zones on the surface. These In- rich zones act as nucleation sites for the formation of nano-dots on the surface. The decrease in In/P ratio at higher sputtering durations causes the fragmentation of the nano-dots.

3.2 Experimental

InP(111) wafers were sputtered by 3 keV Ar^+ ions in absence of any sample rotation. Sputtering was performed at an incidence angle of 15°, w.r.t surface normal, in a UHV chamber for 5 to 80 minutes with a low ion flux of 1×10^{13} $cm^{-2}s^{-1}$ producing fluences in the range of 3×10^{15} to 4.8×10^{16} $ions/cm^2$, respectively. Nearly 200 images of 50 nm to 10 μm sizes of ion beam modified surfaces were imaged in tapping mode by Scanning Probe Microscope(SPM). The mean size(diameter for circular dots and diagonal length for rectangular dots at 40 min), height and density of the nano dots were calculated from a statistics of around 500 dots for each sample using the Nanoscope software. Raman scattering measurements were performed at room temperature in the backscattering geometry, with a 488 nm argon ion laser at 500 mW. After ion sputtering, *in situ* X-ray Photo-electron Spectroscopy (XPS) experiments were performed in ultra high vacuum (UHV).

3.3 Results and Discussion

Figure 3.1 shows the two dimensional 500 nm×500 nm SPM images of InP surfaces sputtered for durations varying from 5 minutes to 80 minutes (fluences are mentioned in fig. 3.1). An image from a virgin (un-sputtered) surface is also shown (fig. 3.1a). After sputtering for 5 min some irregular structures, wavy patterns as well as some dots are seen on InP surfaces (fig. 3.1b). However, after 10 min sputtering the surface topography appears very different. The surfaces display the presence of several nano dots (fig. 3.1c). The size and the height distributions are shown in figures 3.2 and 3.3. The density of dots is found to be $2 \times 10^{11}\ cm^{-2}$. The dots display a narrow size distribution with a mean dot diameter of $24 \pm 4\ nm$ and a mean height of $4 \pm 0.4\ nm$ (fig. 3.3). Very small nano dots of sizes smaller than 13 nm and heights lower than 3.5 nm are also seen (fig. 3.2). The autocorrelation image of the nanodot pattern for 10 min sputtering (fig. 3.1c) is shown in fig. 3.5a. This image shows a weak short range ordering among the dots with the mean dot separation of $30 \pm 4\ nm$.

Although the density of the dots remains the same after a sputtering for 20 min (fig. 3.1d), the dots appear to have slightly ripened and grown with the average diameter and the height being 33 nm and 8 nm, respectively(fig. 3.3). The ripening of dots continues after the sputtering for 30 min also. At this stage, however, a drastic agglomeration of dots is also observed in fig. 3.1e. As a result, a large increase in the size and height of dots is observed with their average diameter and height becoming 47 nm an 17 nm, respectively(fig. 3.2). Nano dots smaller than 15 nm, seen after early stage of sputtering of 5 and 10 min are not observed at this stage. Moreover, several dots of sizes as large as 90 nm and heights as large as 27 nm can be seen. Both the height and size distribution have become broader due to the ripening and agglomeration of dots. As a consequence of agglomeration, the density of the dots decreases to $4 \times 10^{10}\ cm^{-2}$.

After 40 min sputtering, SPM image displays an array of rectangular shaped cells as shown in fig. 3.1f. The spatial distribution of these dots appears very uniform

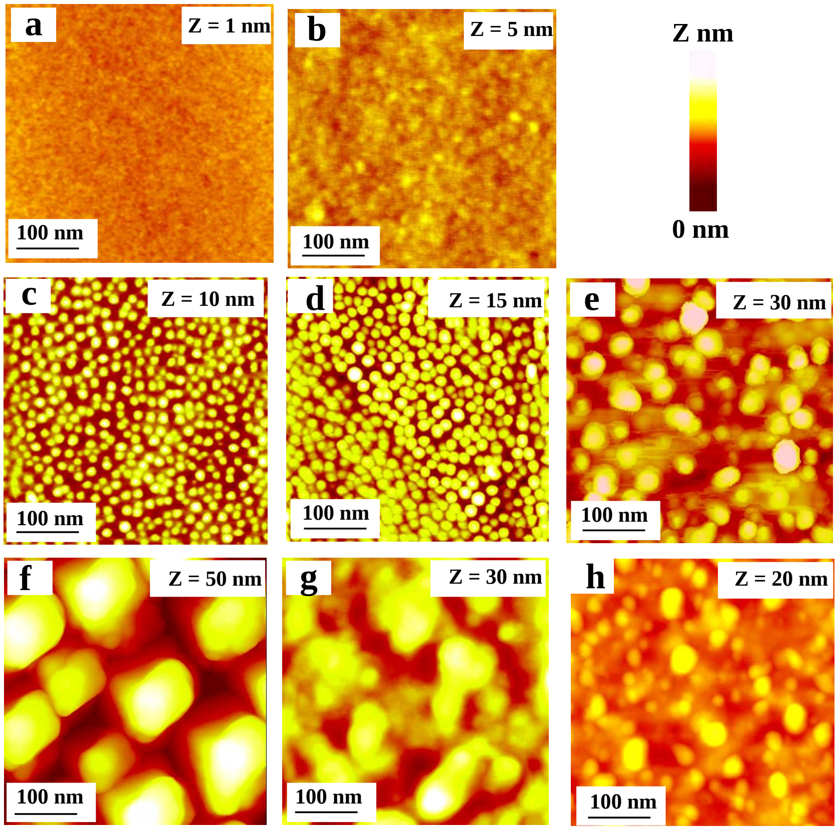

Figure 3.1: 500 × 500 nm^2 SPM images of InP surfaces for the virgin sample (a), as well as after sputtering it for 5 min (3×10^{15} $ions/cm^2$)(b), 10 min (6×10^{15} $ions/cm^2$)(c), 20 min (12×10^{15} $ions/cm^2$)(d), 30 min (18×10^{15} $ions/cm^2$)(e), 40 min (24×10^{15} $ions/cm^2$)(f), 60 min (36×10^{15} $ions/cm^2$)(g), and 80 minutes(48×10^{15} $ions/cm^2$) (h).

with the rectangular dots arranged in rows. Fig. 3.4 shows the SEM image taken on large area after 40 min sputtering where the ordering of the self assembled InP nano dots can be clearly seen. The process of ripening and agglomeration of dots continues causing further increase in the size and the height of the dots and a decrease in their density. Figures 3.2 and 3.3 show immense increase in the size and the height of the dots at this stage with their average size and height becoming 90 nm and 41 nm, respectively. Dots smaller than 40 nm or lower than 25 nm are not observed. The density of the dots is observed to be 6×10^9 cm^{-2}. Table 1 lists the density, mean

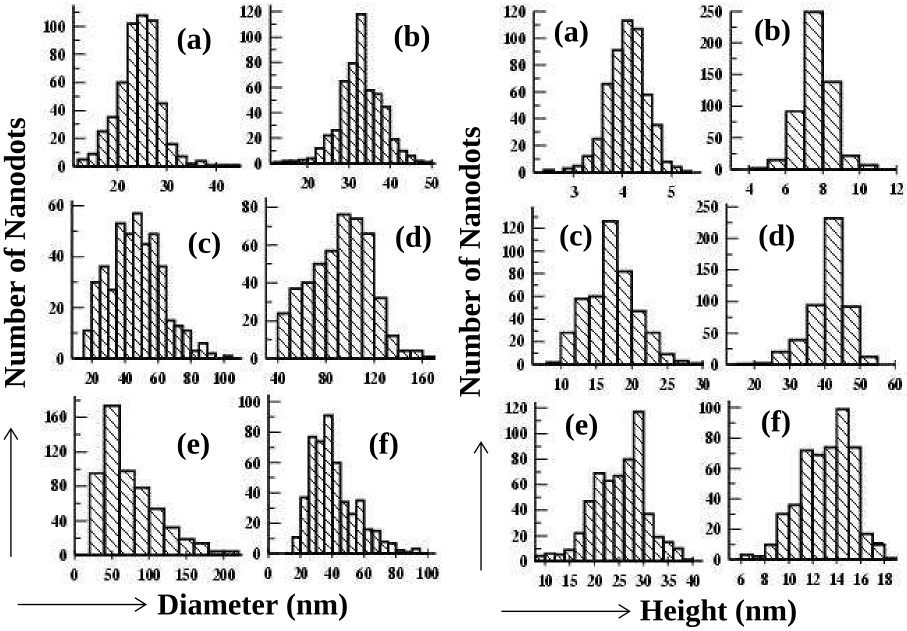

Figure 3.2: Size (a) and height (b) distributions of the nanostructures formed after sputtering.

size and mean height of the nano-structures at the various sputtering times:

Table 1: Density, size and height distribution of nano-structures

Time(min)	Density(cm^{-2})	Size(nm)	Height(nm)
10	2×10^{11}	24 ± 4	4 ± 0.4
20	2×10^{11}	33 ± 5	8 ± 0.9
30	4×10^{10}	47 ± 16	17 ± 3
40	6×10^{9}	90 ± 26	41 ± 5
60	3×10^{10}	75 ± 37	25 ± 5
80	5×10^{10}	41 ± 14	13 ± 2

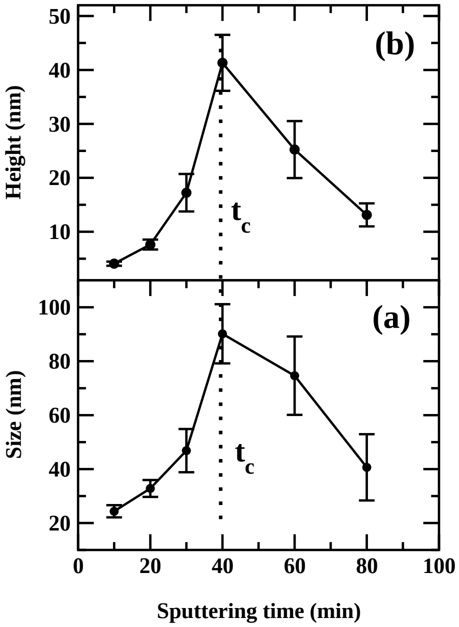

Figure 3.3: Mean size (a) and mean height (b) of the nanostructures formed at different sputtering time. t_c represent the critical time (discussed in the text)

The nano dot patterns obtained at 10 min display self-organization (fig. 3.1c) with short range weak square order as revealed by 2D auto-correlation pattern in fig. 3.5a. During the coarsening, when the dots grow, the size (and height) distributions becomes broader (fig 3.2 b,c,d) and although the dots continue to exist, the local order in their pattern, which was present at 10 min, becomes weaker. The local order, though still weak becomes better at 40 min. SPM image (fig. 3.1f) exhibits a self assembly of rectangular celled arrays and its 2D auto-correlation pattern displays a weak short range ordering in fig. 3.5b.

Interestingly, for sputtering durations higher than 40 min, a combination of inverse ripening and fragmentation of nano dots is observed. Figure 3.1g displays the fragmentation of several bigger dots into smaller dots after 60 min sputtering. As a

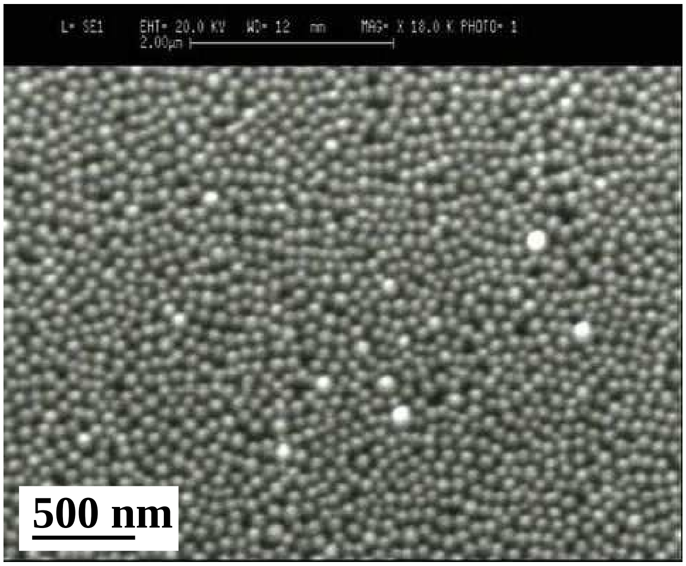

Figure 3.4: SEM image showing $3\mu m \times 2.7\mu$m pattern of self assembled nano dots formed after 40 min of sputtering.

consequence, the density of dots increases to 3×10^{10} cm^{-2} and the size of the dots reduces. The dots have an average size of 75 nm compared to 90 nm seen after 40 min of sputtering. The average height of the dots also reduces to 25 nm compared to 41 nm after 40 min sputtering (fig. 3.3). Moreover, small dots of sizes 20 nm and height 5 nm are seen at this stage (see fig. 3.2e), which were not seen after 40 min. The decrease in height suggests that the inverse ripening may not just happen due to the fragmentation of dots, due to sputtering, into smaller sizes but some mass flow from larger to smaller dots may also be involved. Both size and the height distributions are very broad at this stage. Existence of some large 200 nm nano dots suggests that a few dots may also ripen at this stage. However, their numbers is very small and fragmentation and inverse ripening dominates the structure formation. SPM images show that the fragmentation and inverse ripening of nano dots continues after 80 min of sputtering also(fig. 3.1h). This causes a further decrease in size and height of nano dots as well as an increase in their density to 5×10^{10} cm^{-2}. The average size and

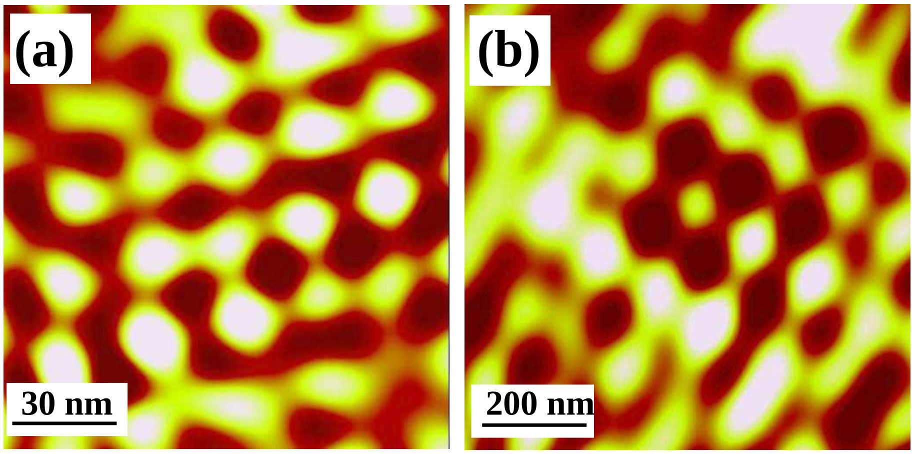

Figure 3.5: Auto-correlation pattern after (a) 10 min sputtering from 150 $nm \times 150$ nm SPM image and (b) 40 min sputtering from 1000 nm × 1000 nm SPM image.

the height of the dots are 41 nm and 13 nm, respectively.

The scenario emerges that the surface with cloud-like patches seen after 5 min transforms into a morphology where isolated and self assembled nano dots, generated by the interplay between the ion induced roughening and the surface relaxation [12], are seen after 10 min. The amplification of the random amplitudes by the negative surface tension compete with the smoothening processes such as surface diffusion and viscous flow leading to the formation of nano-dot patterns. Numerical simulations by Kahng *et al.* show that these dots are inherently non-linear objects [6]. The dots once formed, coarsen and agglomerate, becoming largest at 40 min. At this stage dots also show weak short range ordering. This stage we refer to critical time, t_c, since beyond this, a fragmentation and inverse ripening of the dots is observed.

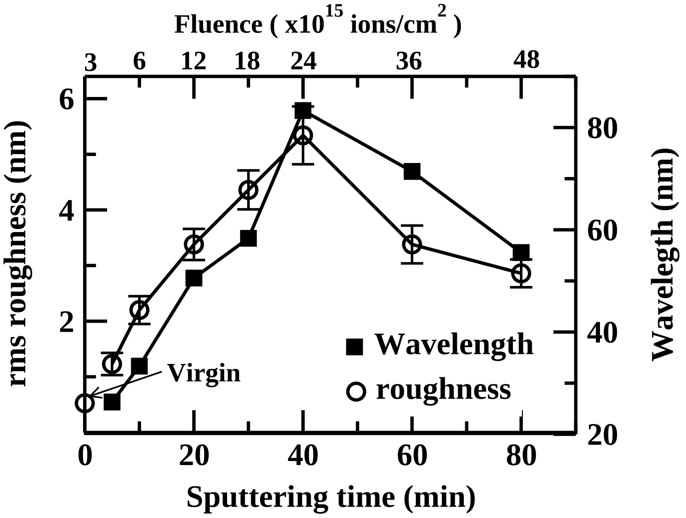

Figure 3.6: Variation of rms surface roughness and spatial wavelength are plotted as a function of sputtering time and fluence (top axis).

3.3.1 Roughness and scaling exponent studies of the nano-patterned surface

Figure 3.6 shows the rms roughness for virgin InP surface as well as after sputtering it (shown in fig.3.1) with 3 keV Ar^+ ions at various fluences. During the early stages of sputtering process, the rms roughness increases from 0.5 nm for the virgin sample to 5.5 nm after sputtering for 40min. However, for higher sputtering durations the roughness decreases to about 3.0 nm after 80 min. Thus, during the coarsening of nano dots from 10 to 40 min the surface roughens whereas when the fragmentation and inverse-coarsening of the nano-dots occurs, beyond 40 min, a slight smoothening in the surface is observed. The time (40 min or the fluence 24×10^{15} $ions/cm^2$) beyond which a slight decrease in rms surface roughness is observed is referred to here as critical time, t$_c$. Smoothening of surface, beyond the critical time, as discussed later is associated with the amorphization of the surface at this stage. At high fluences, the density of electronic excitations increase and the covalent bonds in the lattice weaken or get broken causing the surface-amorphization. The amorphization

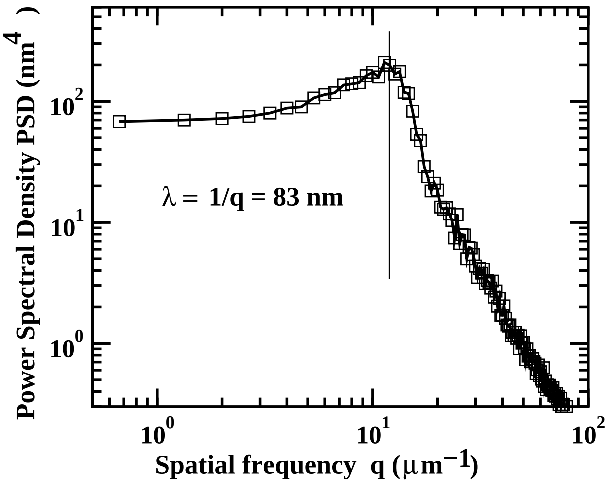

Figure 3.7: A typical PSD spectrum and the corresponding wavelength(λ) for 40 min sputtering has been shown here.

can lead to relaxations [13, 14] and smoothening of the surface via decreased strains [15]. Surface smoothening has been reported for MeV Sb ion implantation in Si[16] and InP[17] as well as for keV implantations of P and As in amorphous films [18].

Also shown in fig. 3.6 is the spatial wavelength (or mean dot separation) of the nano dots determined from the first peak in circularly averaged power spectral density (PSD) spectra. The PSD function is a 2-dimensional Fourier transform of the surface and is defined by [19]:

$$\gamma = \frac{1}{area}\left|\int\int \frac{d^2r}{2\pi} e^{-iq.r}\langle h(r)\rangle_t\right|^2, r = (x, y) \tag{3.1}$$

where q is the spatial frequency (inverse of scan length λ) and *h(r)* is the height at the position r.

Figure 3.7 shows a typical PSD spectra for the InP surface sputtered for 40 min. The first maxima of the PSD plot has been used to measure the wavelength (λ), as $\lambda = 1/q$. Similarly, λ for various sputtering times are measured and plotted in fig 3.6.

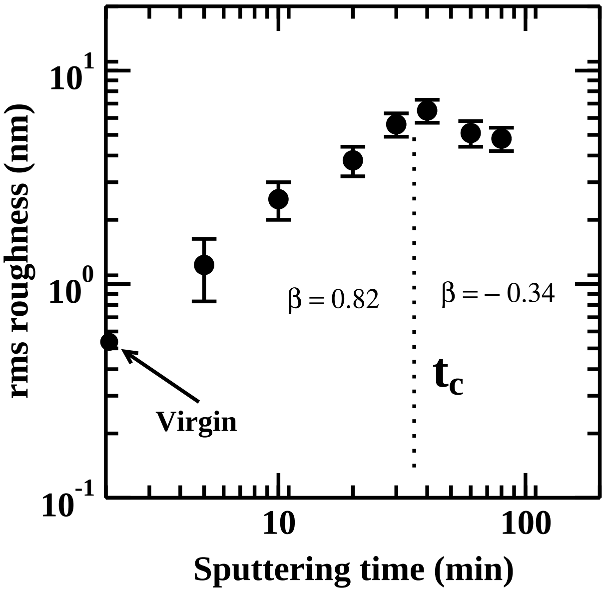

Figure 3.8: Showing the log-log plot rms roughness σ versus sputtering time t. The value of β was extracted from a linear fit of the log-log plot of σ vs t.

Figure 3.6 shows an initial increase of λ upto critical time $t_c = 40\ min$ and then a decrease of λ is noticed for higher sputtering times. The wavelength λ increases with time from $\sim\ 30\ nm$ for 10 min until it reaches a value of $\sim\ 83\ nm$ at 40 min (t_c). For longer durations of sputtering, the wavelength decreases to $\sim\ 55\ nm$ at t=80 min.

Figure 3.8 shows the plot of rms roughness versus the sputtering time in a log-log scale. The linear characteristic indicates that the rms roughness increases with sputtering time according to a power-law. By fitting the power-law behaviour to rms roughness as $\sigma(L,t) \sim t^{\beta}$, we can obtain the growth exponent β. The obtained value of β is 0.82 in early time regimes. Moreover we also observe a crossover in the power law scaling of $\sigma(t)$ from $\beta = 0.82$ in the early time regime to $\beta = -0.34$ in the late time regime.

According to the theoretical expectations [6] for short erosion time $t < t_c$ (critical

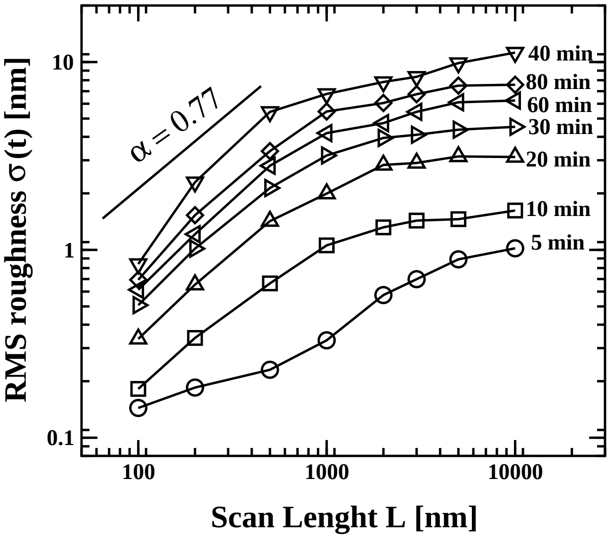

Figure 3.9: Showing the rms roughness σ versus scan length L at different sputtering time. The solid lines represent the best power law fit $\sigma \sim L^{\alpha}$ with $\alpha = 0.77$

time) the surface width should increase exponentially while for $t > t_c$ the surface width still increases but at a much smaller growth rate until it reaches saturation. Our experimental results show that in early time regime the surface morphology is not described by an exponential increase rather it shows a powerlaw behaviour. Moreover beyond the critical time, β decreases. As shown by Cuerno *et al.* [20] a power law behaviour can be a consequence of various non-linear terms which are neglected in the BH model (chapter-1, section 1.1.9). Similar powerlaw behaviour has been observed by Kim *et al.*[21]. However the behaviour of negative β, observed in present study, in long time regimes $t > t_c$ has never been observed before. Our results suggest that the interface width beyond the crossover time is small and actually decreases. The surface evolution may belong to the class of Edward Wilkinson(EW) model [21]. We have also measured the roughness exponent α by plotting the roughness of the ion irradiated surface as a function of the scan length L for different sputtering times. The results are shown in fig. 3.9. It is seen that the local width increases as $\sigma \sim L^{\alpha}$ before it saturates. The roughness exponent α obtained from a linear fit of the unsaturated region of σ versus L is found to be about 0.77. Value of α, varying between 0.7 - 0.8, is nearly independent of ion fluence. The 1+1 dimension simulation by Cuerno *et al.*[20] shows three time regimes with different values of β, but a nearly time-invariant $\alpha = 0.7 - 0.8$. If we assume that their very early-time regime is not accessible within our experiments then our findings for α and β roughly correspond to the results of the simulations. Consequently, it might be concluded that the time evolution of the surface topography is reasonably described by the use of the KS equation(chapter-1, section 1.1.9). However, there are several experimental findings that are not consistent with the KS equation or the BH model[22, 23], one of them are being the presence of negative β, in fig. 3.8, for $t > t_c$. The dependence of wavelength (λ) on fluence , as seen in fig. 3.6, is also not expected for the B-H model (see section 1.1.9).

3.3.2 Raman scattering studies of the nano patterned surfaces

For III-V semiconductors like InP and other zinc- blend structures, the first order Raman spectrum consists of usually two Raman modes corresponding to the Longitudinal Optical (LO) and Transverse Optical (TO) phonons associated with the Brillouin zone center. The zone center phonons corresponding to TO and LO modes obey the following selection rules for zinc blend type crystals. For the scattering by (111) face, both LO and TO modes are allowed in Raman scattering. However, only TO mode is allowed for scattering by (110) face whereas only LO mode is allowed for (100) face. Both LO and TO modes being allowed for InP(111), we have been able to investigate the evolution of both these modes at various sputtering fluences. Raman spectra from virgin (bulk) InP and nano patterned InP surfaces after Ar^+ ion sputtering are shown in Fig. 3.10. The LO and TO modes appearing at 351.5 cm^{-1} and 301.5 cm^{-1}, respectively, for the virgin sample, soften and shift towards lower wave-numbers appearing at 350.5 and 300.5 cm^{-1}, respectively, for 5 min sputtering.

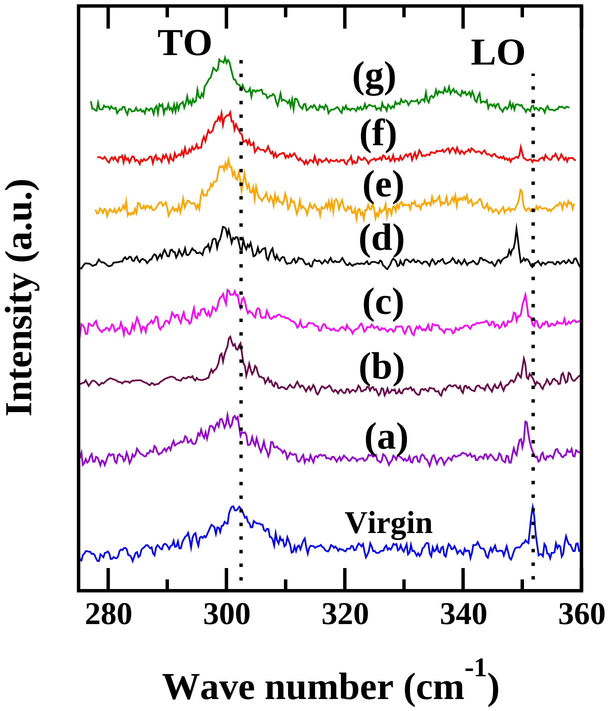

Figure 3.10: Raman Spectra of virgin InP and 3keV sputtered InP surfaces after sputtering for (a)5 min, (b) 10 min, (c) 20 min, (d) 30 min, (e) 40 min, (f) 60 min, and (g) 80 minutes.

The softening of the modes, suggests development of tensile stress after sputtering [15]. Due to the Fröhlich interactions[24], LO is a more surface sensitive mode and thus its modifications may reflect the structural changes on the InP surface [25]. The LO mode shifts to 350.2, 350.3 and 349.2 cm^{-1} after 10, 20 and 30 min, respectively, with the largest shift being 2.3 cm^{-1} after 30 min. The surface, thus, is under tensile stress that increases with time up to 30 min. The assymmetricity seen in LO modes can be attributed to the phonon confinement effects in nanodots [25]. At t_c (=40min), a reduction in shift to 1.8 cm^{-1} (LO feature at 349.7 cm^{-1}) suggests a slight relaxation in stress. A significant decrease in the LO intensity is also noticed at t_c. The reduced stress, lower LO intensity as well as the appearance of a broad feature at 340 cm^{-1} suggest the initiation of amorphization at the InP surface at this stage (fluence of 24×10^{15} $ions/cm^2$) [26]. With the surface beginning to amorphize

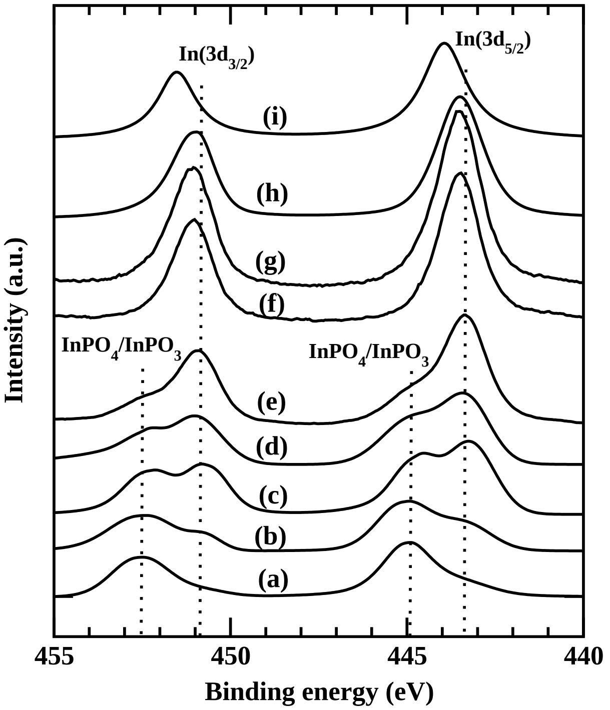

Figure 3.11: High Resolution XPS of Indium (3d) region is shown for (a)virgin as well as after the irradiation for (b) 2 min, (c) 5 min, (d) 10 min, (e) 20 min, (f) 30 min, (g) 40 min, (h) 60 min and (i) 80 min. In(3d$_{5/2}$) and In(3d$_{3/2}$) regions are marked in the figure.

at t_c, the surface becomes completely amorphous at 80 min where no LO feature but a stronger $340cm^{-1}$feature is present [26]. This surface-amorphization also leads to smoothening of the surface seen in fig. 3.6.

3.3.3 Studies of stoichiometry of the ion irradiated nano-patterned surface by XPS

XPS was utilized to measure the electronic binding energy of the core levels features of In(3d) and P(2p) for the InP surface as a function of ion fluence. Figure 3.11 shows the high resolution XPS of In(3d) region from the virgin (un-irradiated) as well as ion irradiated InP surfaces. The XPS from virgin sample (Fig. 3.11a) shows two

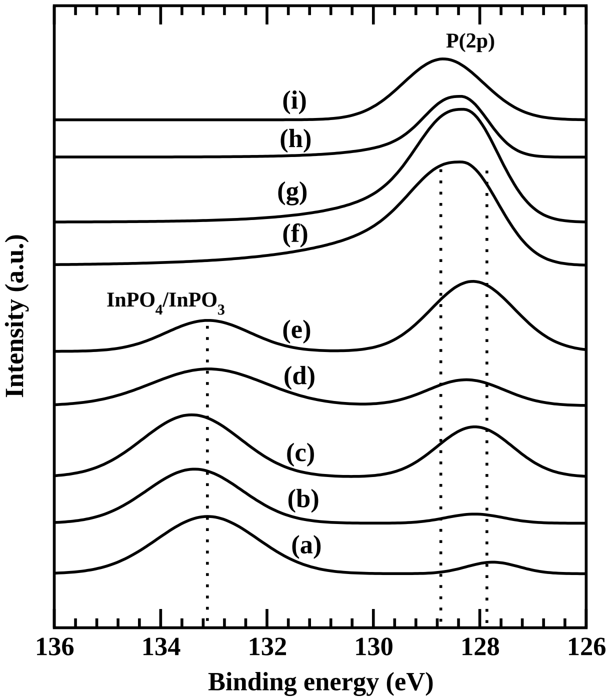

Figure 3.12: High Resolution XPS of Indium (3d) region is shown for (a)virgin as well as after the irradiation for (b) 2 min, (c) 5 min, (d) 10 min, (e) 20 min, (f) 30 min, (g) 40 min, (h) 60 min and (i) 80 min.

broad regions around 444 and 452 eV. Each of these features can be deconvoluted into two features. The peak at 443.27 and 451.08 eV are due to In(3d$_{5/2}$)-P and In(3d$_{3/2}$)-P bonds, respectively. Lee and Anderson reported that InPO$_3$ and InPO$_4$ oxide peaks are shifted from the In(3d)-P peaks to higher binding energies by about 0.8 and 1.5, respectively [27]. Thus, the features at higher binding energy of In(3d$_{5/2}$)-P at 444.9 eV as well as at the higher binding energy of In(3d$_{3/2}$)-P at 452.4 eV (in fig. 3.11a) may be due to these oxides. With the increase in the sputtering time the intensity of these oxide features decrease upto 20 min. After 30 min, clean In3d$_{5/2}$ and In3d$_{3/2}$ features are observed at 443.58 and 451.39 eV, respectively. In(3d) features also display shifts towards higher binding energies at 60 and 80 min.

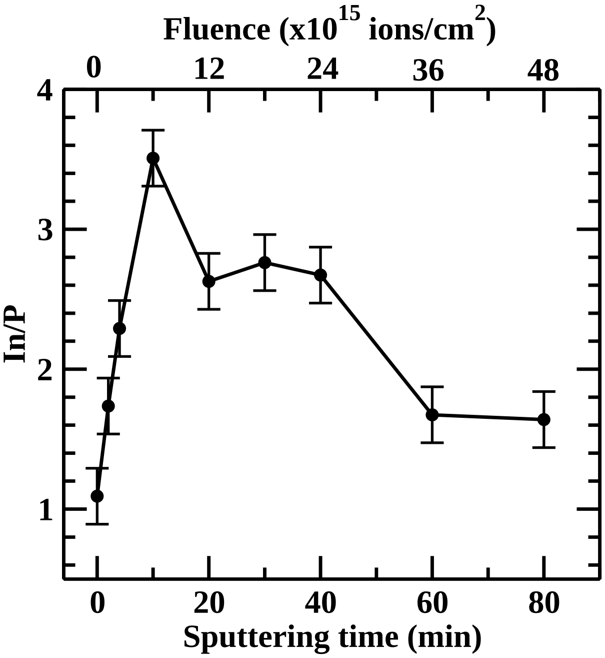

Figure 3.13: Ratio of areas of In(3d) and P(2p) features for the virgin InP as well as after sputtering it for various sputtering times or fluences (top axis)

Figure 3.12 shows the XPS spectra of the P(2p) region for the virgin as well as the ion irradiated InP surfaces. For the un-irradiated sample (Fig. 3.12a), the P(2p) peak at 128 eV can be de-convoluted into two peaks, P ($2p_{3/2}$) at 127.6 and P ($2p_{1/2}$) at 128.4, with a peak energy difference of 0.8 eV. The binding energies of $InPO_3$, $InPO_4$ and P_2O_5 oxides are known to be higher than that of P(2p) peak by about 4.5, 5, 7 eV, respectively [27]. The peak observed at 133 eV in fig. 3.12a may be thus, due to InP native oxide (i.e. P in $InPO_3$ and $InPO_4$ matrix). However, no clear P_2O_5 feature at $\sim$ 135 eV was observed. The signal due to oxides decrease upto 20 min and at 30 min no oxide feature is visible. At 30 min the components of the P(2p) are observed at 128.0 and 128.8 eV corresponding to the $2p_{3/2}$ and $2p_{1/2}$ features, respectively. P(2p) features also display shifts towards higher binding energies at 60 and 80 min.

Fig. 3.13 displays the ratio of areas of the In(3d) and P(2p) features. The ratio for the virgin InP is 1.1 which is slightly higher than 1 due to the presence of native oxide layer. Similar result has been reported earlier [7]. A high ratio, 3.5, of In/P is observed for 10 min. This shows an excess In on the surface which may be promoting the nucleation of dots on the InP surface. The ratio remains high (although not as high as that at 10 min) up to 40 min. After 40 min, a drastic decrease in In/P ratio to 1.6 is seen. This may be causing the fragmentation of dots (seen in fig. 3.1) after 60 and 80 min.

InP is a III-V compound with a mass difference of 84 u between In(m=114.82) and P(m=30.97). This large mass difference causes preferential sputtering of P atoms, compared to In atoms, during ion irradiation of InP surfaces. This effect becomes pronounced for the sputtering under oblique ion incidence of non-rotating sample surfaces where preferential P sputtering leads to agglomeration of *In* and formation of *In rich regions* [28]. These *In rich zones* become the nucleation centers for the formation of self assembled nanostructures seen in Fig. 3.1. Indium(In) agglomeration at the nucleation of nano-dot position cause the Schwobel barrier affects to control the surface evolution in early times. Dot coarsening, on the other hand, may be controlled by the diffusion current driven by the In concentration gradient across the surface [29]. Smoothening of the surface may reduce this gradient thus promoting the inverse coarsening phenomenon seen here.

A large In/P ratio of 3.5 at 10 min, thus leads to pattern formation on InP surface. Long sputtering can cause the reduction in preferential sputtering of P atoms, since the top layers will predominantly contain In atoms, leading to a decrease in In/P ratio as seen at 80 min. This causes the fragmentation of the nano dots at high sputtering times. The preferential sputtering of P over In atoms also leads to P vacancy sites on the InP surface as well as causes the presence of uncompensated In^+ species on the surface. These uncompensated charge regions on the surface can lead to the higher oxidation states resulting in the higher binding energies for In(3d) and P(2p) core levels, at 60 and 80 min. Presence on nanocrystalline zones can also cause the shifting of In(3d) and P(2p) towards higher binding energies.

3.4 Summary and Conclusion

In conclusion the surface with cloudlike patches seen after 5 min transforms into a morphology where isolated and self assembled nano dots, generated by the interplay between the ion induced erosion and the surface relaxation, are seen after 10 min. The amplification of the random amplitudes by the negative surface tension compete with the smoothening processes such as surface diffusion and viscous flow leading to the formation of nano-dot patterns. During this process the size of dots increases and their size distributions becomes broader leading to an increased roughness of the surface. The dots once formed, coarsen and agglomerate, become largest at 40 min. Raman scattering results shows that surface also experiences a tensile stress which increases with sputtering but relaxes at t_c where the surface-amorphization is first observed. This results in the inverse ripening and fragmentation of dots along with the smoothening of InP surface for longer sputtering durations. The scaling parameters have been measured for the ion irradiated surfaces. The roughness (α) and the growth (β) exponents have been determined to be 0.77 and 0.82, respectively. A negative β, beyond t_c, is also observed. We further observe that the characteristic wavelength, of the surface patterns, depends on the ion fluence. XPS results demonstrate that keV irradiation leads to an excess of In atoms on the surface that promote the nucleation of nano dots leading to their self assembled growth. Decrease in In/P ratio causes the breaking of nano dots into smaller structures.

Bibliography

[1] Andrew N. Shipway, Eugenii Katz, Itamar Willner, ChemPhysChem,**1**, 18 (2000).

[2] Peter Sigmund, Phys. Rev. **184**, 383 (1969).

[3] R. Mark Bradley and James M. E. Harper, J. Vac. Sci. Technol. A **6**, 2390 (1988).

[4] C. M. Demanet *et al.*, Surf. Interface Anal. **23**, 433 (1995); **24**, 497 (1996), **24**, 503 (1996).

[5] S. Facsko, T. Dekorsy, C. Koerdt, C. Trappe, H. Kurz, A. Vogt, H. L. Hartnagel, Science **285**, 1551 (1999).

[6] B. Kahng, H. Jeong and A.-L. Barabasi, Appl. Phys. Lett. **78**, 805 (2001).

[7] S.K. Tan, A.T.S. Wee, J. Vac. Sci. Technol. B **24**, 1444 (2006).

[8] F. Frost, A. Schindler, and F. Bigl, Phys. Rev. Lett. **85**, 4116 (2000).

[9] B. Ziberi, F. Frost, and B. Rauschenbach, Appl. Phys. Lett. **88**, 173115 (2006).

[10] S.W. Maclaren, J.E. Baker, N.L. Finnegan, C.M. Loxton, J. Vac. Sci. Technol. A **10**, 468 (1992).

[11] F. Frost, B. Ziberi, T. Hoche, B. Rauschenbach, Nucl. Instr. and Meth. B **216**, 9 (2004).

[12] Mario Castro, Rodolfo Cuerno, Luis Vazquez, and Raul Gago, Phys. Rev. Lett. **94**, 016102 (2005).

[13] C.A. Volkert, J. Appl. Phys. **70**, 3521 (1991) and reference therein.

[14] P.C. Srivastava, V. Ganesan, and O.P. Sinha, Nucl. Instru. Methods, Phys. Res. B 222, 491 (2004).

[15] S. Dey, C. Roy, A. Pradhan, S. Varma, J. Appl. Phys. **87**, 1110 (2000).

[16] S. Dey, D. Paramanik, V. Ganeshan, S. Varma, Appl. Surf. Sci **253**, 1116 (2006).

[17] D. Paramanik, A. Pradhan and S.Varma, J. Appl. Phys. **99**, 014304 (2006).

[18] R. Edrei, E. N. Shauly, and A. Hoffman, J. Vac. Sci. Technol. A. **20**, 344 (2002).

[19] R. Petri, P. Brault,O.Vatel, D. Henry, E .Andre, P. Dumas, and F. Salvan, J.Appl. Phys.**75**, 7498 (1994) .

[20] R. Cuerno, H. A. Makse, S. Tomassone, S. T. Harrington, and A.-L. Barabsi, Phys. Rev. Lett. **75**, 4464 (1995); M. A. Makeev and A. L. Barabasi, Appl. Phys. Lett. **71**, 2800 (1997); M. A. Makeev, R. Cuerno, and A. L. Barabasi, Nucl. Instrum. Methods Phys. Res. B **197**, 185 (2002).

[21] J. Kim, B. Kahng, and A. L. Barabasi, Appl. Phys. Lett. **81**, 3654 (2002).

[22] R. M. Bradley, Phys. Rev. E 54, 6149 (1996).

[23] R. M. Bradley and E.-H. Cirlin, Appl. Phys. Lett. 68, 3722 (1996).

[24] K.J. Nash and M.S. Skolnick, Phys. Rev. Lett.**60**, 863 (1988).

[25] D. Paramanik and S. Varma, J. Appl. Phy.**101**, 023528 (2007).

[26] R.Cusco, G. Talamas, L. Artus, J.M. Martin and G. Gonzalez-Diaz, J. Appl. Phys. **79**, 3927 (1996).

[27] Y.S. Lee and W.A. Anderson, J. Appl. Phys. **65**, 4051(1989).

[28] M. Nozu, M. Tanemura and F. Okuyama, Surf. Sci. Lett. **304**, L468 (1994). Lett. **81** 4184(1998).

[29] S.G. Mayr, M. Moske and K. Samwer, Phys. Rev B. **60** 16950 (1999).

Chapter 4

Nano pattern formation and surface modification by 1.5 MeV Sb ion irradiation on InP(111)

4.1 Introduction

Submicron morphology of semiconductor surfaces, developed by MeV irradiation, poses interesting challenges; like how do surface structures spontaneously develop at these energies or how does their evolution or distribution compare with the surface structures that develop at other energies. At low (keV) energy regimes, the elastic nuclear energy losses (S_n) play a dominant role in the development of surface structures. The self assembly of nano dots on InP(111) surfaces, their evolution as well as the surface roughness or amorphization, after 3 keV Ar ion irradiation (as discussed in chapter-3) are crucially controlled by S_n. At SHI energies also, it has been shown by earlier studies [1, 2], S_n is effectively responsible for the development of surface morphologies and S_e often leads to the annealing of defects. S_n induced sputtering, irradiation induced de-wetting, mass flow, dangling-bond induced flow, radiation induced segregation, stoichiometric modifications are some primary processes that, depending on the ion energy and target characteristics, can cause surface roughening in semiconductors. On the other hand, annealing of defects by S_e, sputter re-deposition, viscous flow, surface diffusion etc. can lead to surface smoothening. The surface evolution, after ion bombardment, is governed by the competition between the various roughening and smoothening processes. In a recent work it has been shown that the surfaces, evolving after ion irradiation, sometimes display scaling relations which have been applicable for non-equilibrium thin film growth[3, 4].

In this chapter the results on the modification in roughness and morphology of InP surfaces upon 1.5 MeV Sb ion implantation are presented. Formation of nanoscale defect structures on InP surface due to Sb implantation have been observed in SPM images. The height and size distributions of the nanoscale defect structures have been presented here. We further observe that the MeV Sb ion implantation in InP leads to surface roughness that displays two different behaviours as a function of fluence. Initially, the surface roughness increases with increasing fluence. Beyond a critical fluence, however, the surface roughness decreases with increasing fluence. The smoothening of the surface thus may be related to the amorphization in InP. We have also utilized the Raman scattering technique, discussed in chapter-5, to understand the modifications in surface roughness of InP after implantation. The Raman scattering results indicate that the critical fluence, where the surface roughness begins to decrease for increasing fluence, occurs at a stage when the InP lattice has become amorphous.

Surface scaling analysis via Power Spectral Distributions (PSD) demonstrate that diffusion processes are smoothening the implanted surfaces. In addition, we have also evaluated the Radial Separation Distributions (RSD) of the nanostructures that form on the InP surfaces after implantation. Interestingly, we observe a scaling behavior as has been suggested for thin films growths [5]. However, we also observe that the nanostructures are not uniformly distributed and exhibit clustering at $r \approx \langle R \rangle$ where$\langle R \rangle$ is the avarage separation between the nanostructures. This is a surprising result as ion beam induced structure formation will be expected to be created in a random fashion. These radial distribution scaling studies have never been applied for the investigation of the structure formation on ion bombarded surfaces.

The scaling studies and the scaling exponents characterize the nature of surface roughness and provide the crucial information on the surface roughening mechanisms as well as the parameters governing the patterning of the surfaces. The scaling exponents: the roughness exponent (α) and the growth exponent (β) have been investigated here for various ion fluences. The scaling behaviour of the critical wavelength (λ) of the patterns formed, on InP(111) surfaces, is also studied. We show that the dynamics of the surfaces evolved after ion implantation do not obey simple Bradley-Harper (BH)[6] or Kuramoto-Sivashinsky (KS)[7, 8] type growth model.

4.2 Experimental

A mirror polished (111)-oriented InP single crystal wafer was used in the present study. The samples were implanted at room temperature with a scanned beam of 1.5 MeV Sb^{2+} ions at various fluences ranging from 1×10^{11} to $5\times10^{15} ions/cm^2$. The average Sb flux was 0.02 μA/cm^2. This current was measured directly on the target after suppressing the secondary electrons by applying a negative bias of 200V to a suppressor assembly around the target. The implantations were performed with the samples oriented 7^o off-normal to the incident beam to avoid channeling effects. Monte Carlo simulations were performed for 1.5 MeV Sb implantation in InP using the SRIM2006 code and the mean projected range of Sb-ion distribution was found to be 400 nm [9]. SPM was used to image the implanted InP (111) surfaces. Several images ranging from 0.2 to 10 μm square were obtained and anlyzed. The root mean square (rms) surface roughness and the mean size(diameter), height and density of the nano dots were calculated for each sample using the Nanoscope software.

4.3 Results and Discussion

Figure 4.1 shows the 10 $\mu m \times 10$ μm 2D SPM images from the InP surfaces. The image from a virgin (un-implanted) InP(111) sample is shown and it is observed that this surface is smooth. Other images of fig. 4.1 show the evolution of the surface morphology on InP surfaces after 1.5 MeV Sb implantation at fluences ranging from 1×10^{11} $ions/cm^2$ to 1×10^{15} $ions/cm^2$. Comparison of the surface morphologies of InP surfaces of fig. 4.1, after implantation, show the formation of nanoscale sized defects with varying size, height and density depending on the fluence. Figure 4.1a shows the InP surface after an Sb implantation with 1×10^{11} $ions/cm^2$. Several nano sized defects can be observed on the surface. The structures have developed due to the damage created at the surface.

We have investigated the height and the size distribution of the nanoscale sized defects (seen in fig. 4.1) on the InP surfaces after various Sb fluences. The size and the height distributions are shown in fig. 4.2 and 4.3 respectively. After a fluence of 1×10^{11} $ions/cm^2$, most of the nanostructures have a diameter smaller than 450 nm and a height smaller than 10 nm. The density of the nanostructures has been calculated to be about 2.5×10^8 cm^{-2}. Figure 4.1b shows the InP surface image after an Sb fluence of 1×10^{12} $ions/cm^2$. It is observed that the nanostructures have become bigger in size. As seen in the size distribution of fig. 4.2b, some structures have diameter as large as 1200 nm. However, a large number of nanostructures have diameter smaller than 200 nm. Although some nanostructures are as high as 18 nm, most of the nanostructures are lower than 12 nm (fig. 4.3b). Furthermore, a large number of nanostructure have a height lower than 4 nm. The total density of the nanostructures is found to be similar to that observed at 1×10^{11} $ions/cm^2$. At 1×10^{13} $ions/cm^2$, in fig. 4.1c, we notice a slight increase in the density of nanostructures to 3.6×10^8 cm^{-2}.

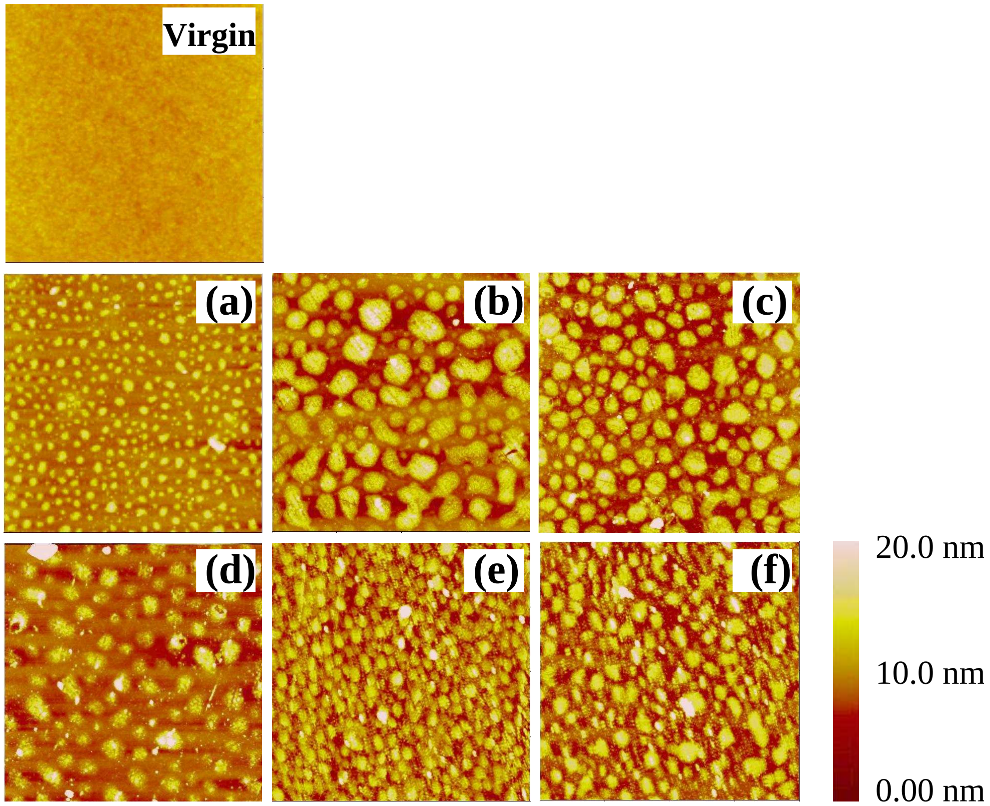

Figure 4.1: 10 $\mu \times 10$ μ SPM images of InP surfaces for the virgin sample as well as after implantation with 1.5 MeV Sb ions at a fluence of (a) 1×10^{11} $ions/cm^2$, (b) 1×10^{12} $ions/cm^2$, (c) 1×10^{13} $ions/cm^2$, (d) 1×10^{14} $ions/cm^2$, (e) 5×10^{14} $ions/cm^2$. and (f) 1×10^{15} $ions/cm^2$

A few nanostructures have diameters as large as 950 nm. A large number of nanostructures, greater than at 1×10^{12} $ions/cm^2$, have diameters smaller than 200 nm (fig. 4.2c). Although some are 20 nm high, a large number have a height lower than 12 nm (fig. 4.3c). Again, a large number of nanostructures have a height lower than 4 nm. The increase in density at this stage can also be noticed by a changed (y) scale for both the distributions. Figure 4.1d shows the image acquired after the fluence of 1×10^{14} $ions/cm^2$. The density of the nanostructures is about 5.0×10^{8} cm^{-2}. The size and the height distribution is very similar to that observed at 1×10^{13} $ions/cm^2$. However, the diameter of the largest nanostructures observed is smaller (700 nm)

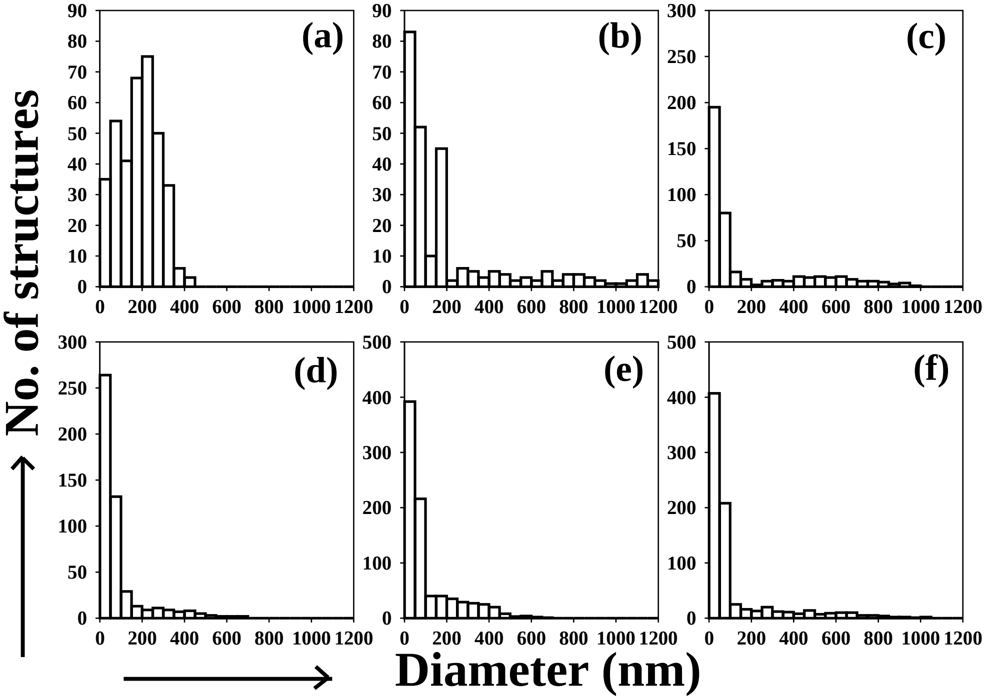

Figure 4.2: Size distributions of the surface structures after 1.5 MeV Sb implantation with fluences of (a) 1×10^{11} $ions/cm^2$, (b) 1×10^{12} $ions/cm^2$, (c) 1×10^{13} $ions/cm^2$, (d) 1×10^{14} $ions/cm^2$, (e) 5×10^{14} $ions/cm^2$. and (f) 1×10^{15} $ions/cm^2$

and the number of small (diameter less than 100 nm) nanostructures has increased (fig. 4.2d). Also, larger number have a height lower than 4 nm (fig. 4.3d). After a fluence of $5{\times}10^{14}$ $ions/cm^2$, a drastic increase in density of the nanostructures is observed in fig. 4.1e. We also observe a larger number of nanostructure with small size. The density of nanostructures at this stage is about $8.0{\times}10^8$ cm^{-2}. Although the size distribution is similar to that observed at $1{\times}10^{14}$ $ions/cm^2$, there are many more nano-structures with small 0-100 nm diameter (fig. 4.2e). Similarly the nanostructures having height smaller than 4 nm has increased (fig. 4.3e). The SPM image after a fluence of $1{\times}10^{15}$ $ions/cm^2$ is shown in fig. 4.1f. The density of the nanostructures, $8.0{\times}10^8$ cm^{-2}, as well as the size and the height distributions are very similar to those observed after $5{\times}10^{14}$ $ions/cm^2$. However, some structures of large

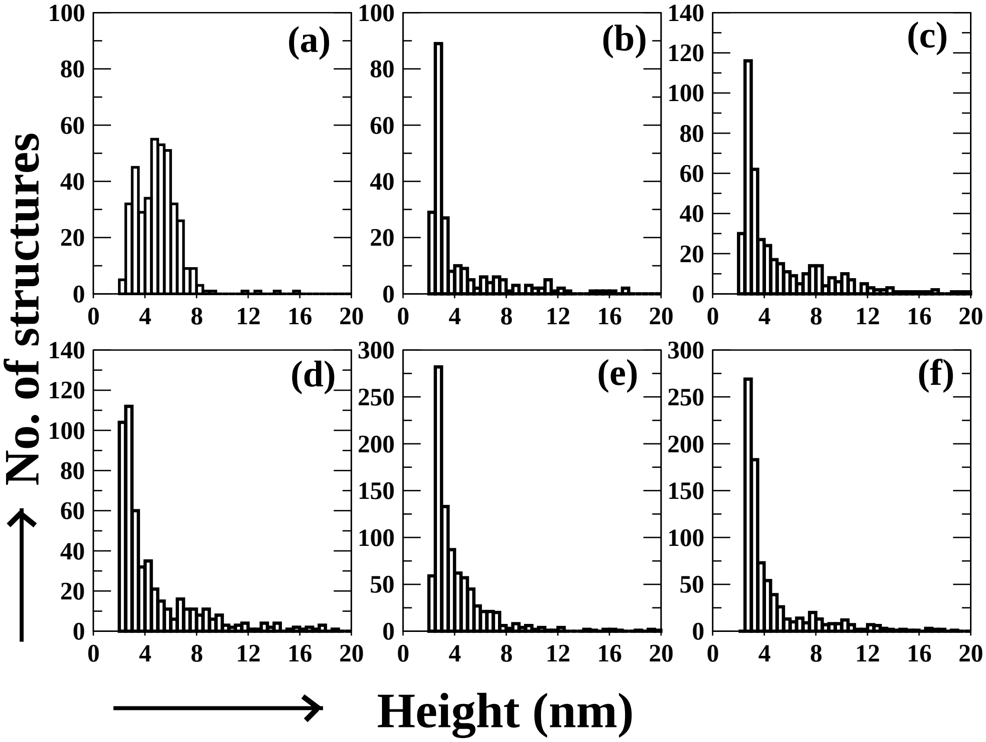

Figure 4.3: Height distributions of the surface structures after 1.5 MeV Sb implantation with fluences of (a) 1×10^{11} $ions/cm^2$, (b) 1×10^{12} $ions/cm^2$, (c) 1×10^{13} $ions/cm^2$, (d) 1×10^{14} $ions/cm^2$, (e) 5×10^{14} $ions/cm^2$. and (f) 1×10^{15} $ions/cm^2$

1000 nm diameter (fig. 4.2f) are also seen. Similar size and height distributions were also observed for 5×10^{15} $ions/cm^2$. Table 1 lists the total density of the structures seen on the surface at all the fluences. In table 1, we have also mentioned the number of nanostructures smaller than 100 nm and 200 nm seen at each fluence. For the fluence of 1×10^{12} $ions/cm^2$, although the density of surface structures is similar to that observed at 1×10^{11} $ions/cm^2$, the number of smaller structures increases. Although the density of nanostructures smaller than 100 nm increases upto the fluence of 1×10^{14} $ions/cm^2$, it decreases for higher fluences. The decrease in the number of small structures may be due to the formation of some bigger structures at higher fluences.

Table1: Density and size of nano-structures

Fluence(cm^{-2})	Density(cm^{-2})	*Structures < 200nm*	*Structures < 100nm*
1×10^{11}	2.5×10^{8}	54%	24%
1×10^{12}	2.5×10^{8}	75%	53%
1×10^{13}	3.6×10^{8}	73%	67%
1×10^{14}	5.0×10^{8}	88%	79%
5×10^{14}	8.0×10^{8}	82%	72%
1×10^{15}	8.0×10^{8}	83%	77%

Here we notice that for all fluences, the defect density is far lower than the ion beam fluence. Possible reasons for this will be discussed below. Figure 4.4 shows the high resolution $1 \times 1\ \mu m^2$, $0.5 \times 0.5\ \mu m^2$ and $0.2 \times 0.2\ \mu m^2$ images of the InP(111) surfaces after the fluence of $1 \times 10^{13}\ ions/cm^2$ and $5 \times 10^{14}\ ions/cm^2$. The figures show that the InP(111) surfaces are very different, at each scale, for these two fluences. Some section analysis of the SPM images are shown in fig. 4.5 to display some characteristic features of the distribution of the defects on InP surfaces. Figure 4.5a shows a $1.0 \times 1.0\ \mu m^2$ SPM image of InP surface after an ion fluence of $1 \times 10^{11}\ ions/cm^2$ along with the section analysis demonstrating a defect of 78.1 nm lateral and 1.8 nm vertical dimensions. Some defects of smaller size and height are also visible. Figure 4.5b shows $1.0 \times 1.0\ \mu m^2$ SPM image of InP surface after an ion fluence of $1 \times 10^{12}\ ions/cm^2$.

Some small and big sized defects are visible. Section analysis of a defect with dimensions 534 nm in lateral and 2.5 nm in vertical direction is also shown. We interestingly notice that this defect is actually composed of several smaller defects. These features can be clearly seen in fig. 4.5c where a high resolution $0.4 \times 0.4\ \mu m^2$ SPM image of this defect (from fig. 4.5b) is shown. To emphasize, image in fig. 4.5c shows the internal structure of the big defect analyzed in fig. 4.5b. As seen in fig. 4.5c, the smaller defects embedded in the big defect are of several sizes and heights. Section-analysis of a typical small defect is shown in fig. 4.5c with dimensions of 34.0 nm in

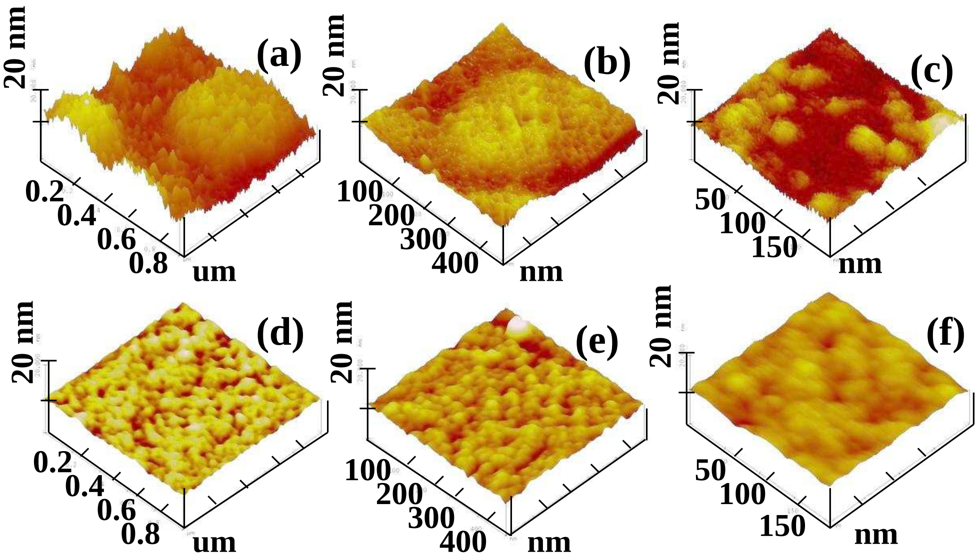

Figure 4.4: InP surface SPM images (a) 1 × 1 μm^2, (b)0.5 × 0.5 μm^2 and (c) 0.2 × 0.2 μm^2 after implantation at fluence of 1×10^{13} $ions/cm^2$. Images (d) 1 × 1 μm^2, (e)0.5 × 0.5 μm^2 and (f) 0.2 × 0.2 μm^2 are after implantation at fluence of 5×10^{14} $ions/cm^2$.

lateral and 1.0 nm in the vertical direction. The image also shows that several defects are overlapping other defects. Figure 4.5d shows a 1.0 × 1.0 μm^2 SPM image for a fluence of 1×10^{13} $ions/cm^2$. The section analysis shows a defect of 62.5 nm lateral and 4.9 nm vertical dimensions. Again, the big defects clearly appear to be composed of several smaller defects. Several small and lower defects can also be seen spread over the surface. Similar behaviour is also noticed in fig. 4.5e where a 1.0 × 1.0 μm^2 SPM image is shown for a fluence of 5×10^{14} $ions/cm^2$. The bigger defects are fully embedded with several smaller defects of various heights. The section analysis shows a defect with 46.9 nm lateral and 1.7 nm vertical dimensions. A big defect is shown in a 0.5 × 0.5 μm^2 image of fig. 4.5f for a fluence of 1×10^{15} $ions/cm^2$. Here also the big defect is embedded with several smaller defects. The section analysis shows a defect with 27.0 nm lateral and 1.0 nm vertical dimensions. Several smaller defects can also be seen around the big defect. These images show that the bigger defects at all fluences are embedded with several of nanosized defects.

During the investigation of 10 × 10 μm^2 images of fig. 4.1, we had noticed that

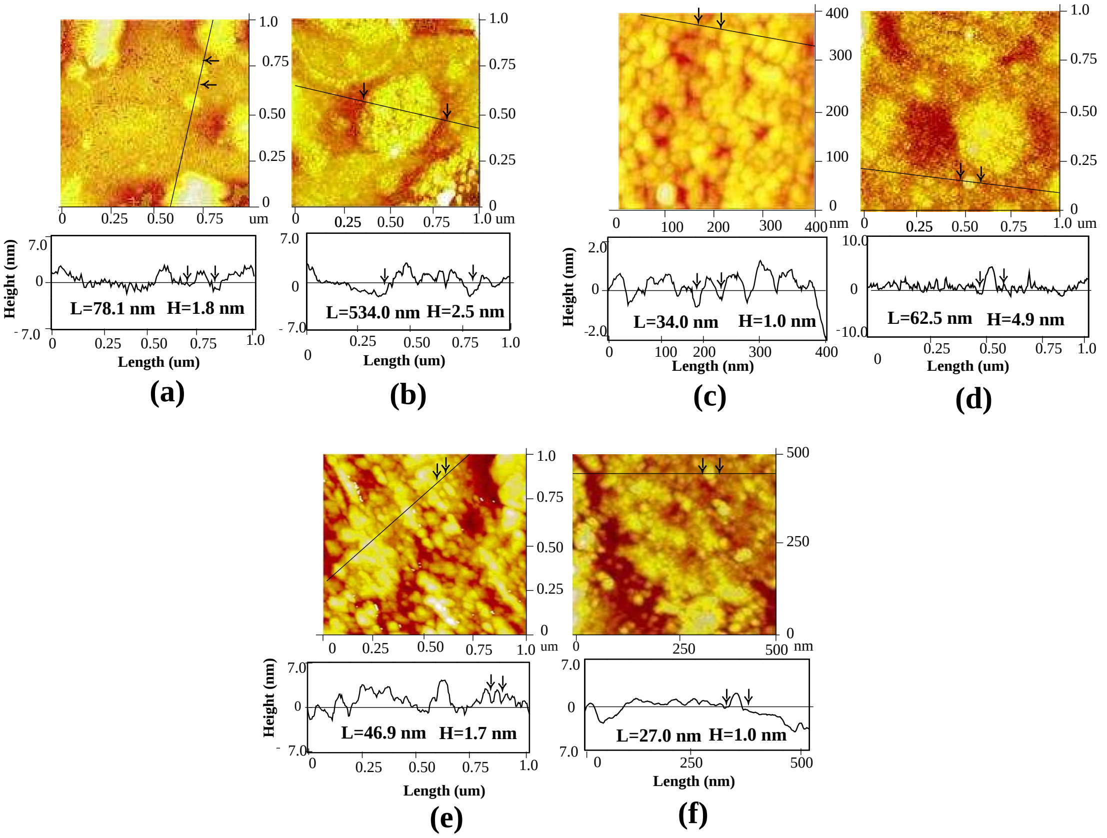

Figure 4.5: InP surface SPM images and SPM-section analysis of (a) $1 \times 1\ \mu m^2$ image for $1 \times 10^{11}\ ions/cm^2$ (b) $1.0 \times 1.0\ \mu m^2$ image for $1 \times 10^{12}\ ions/cm^2$ (c) $0.4 \times 0.4\ \mu m^2$ image for $1 \times 10^{12}\ ions/cm^2$ (d) $1 \times 1\ \mu m^2$ image for $1 \times 10^{13}\ ions/cm^2$ (e) $1 \times 1\ \mu m^2$ image for $5 \times 10^{14}\ ions/cm^2$ (f) $0.5 \times 0.5\ \mu m^2$ image for $1 \times 10^{15}\ ions/cm^2$. (L is the lateral dimension and H is the height of the nanostructure labelled with arrows)

the density of defects for all fluences varies between 2.5-8.0$\times 10^8\ cm^{-2}$, which is much lower compared to the ion fluences. From fig. 4.5, we notice that the bigger defect structures are composed of smaller nanosized-defects of sizes $\sim$ 30 nm. Taking this fact into account we have recalculated the density of defects and find it to be 5.0$\times 10^{10}\ cm^{-2}$ at 1$\times 10^{11}\ ions/cm^2$ and 1 - 1.5$\times 10^{11}\ cm^{-2}$ for higher fluences. We further notice, in figs. 4.3 and 4.5, that the height of defects also vary as a function of fluence. Although, most of the defects are about 4 nm high, higher defects are also increasingly seen at larger fluences (see fig. 4.3). In the framework of model introduced by Gibbons[10], the amorphous material is produced either directly by a single incoming ion or by multiple overlaps. According to this model, the ratio between the total surface area A_A covered by damages and the total area A_0 being implanted is given by

$$\frac{A_A}{A_0} = 1 - e^{-A_1\phi} \sum_{k=0}^{m} \frac{(A_1\phi)^k}{k!} \tag{4.1}$$

where $A_1 = \pi {r_m}^2$ is the surface area damaged by a single ion impact, ϕ is the fluence and m is the overlap number. For 1×10^{11} $ions/cm^2$ with r_m of 30 nm we find that m is 2, i.e. about two ions must impinge on the same area to produce the defect. For 250 MeV Xe irradiation of InP, Herre et al. find that the values of m is between 2 and 3 [11]. Higher heights of defects for larger fluences, as observed in fig. 4.3, may denote larger m. In addition, more than one defect may be getting formed at one place. Overlapping defects as well as defects smaller than 30 nm have also been seen in fig. 4.5. All these factors together can be responsible for the observation of the lower defect density than the ion fluences.

4.3.1 Surface Roughening and Radial Separation Distribution Studies

We have also studied the rms surface roughness of the InP surfaces after MeV ion implantation. In fig. 4.6 we have plotted the rms surface roughness(σ) of the InP surfaces as a function of ion fluence. For a virgin InP(111) surface, σ was measured to be 0.47 nm and is also marked in fig. 4.6. We observe that the rms surface roughness exhibits two distinct behaviors as a function of fluence. Initially up to 1×10^{14} $ions/cm^2$, σ increases with the increasing fluence. However for higher fluences σ decreases for increasing fluences. Our results show that there is a critical fluence of 1×10^{14} $ions/cm^2$, below which the rms roughness of the InP surfaces increases with ion fluence whereas for higher fluences the surface roughness decreases with increasing fluences. This behaviour is similar to that observed for 3 keV irradiation of InP, discussed in chapter-3, where also an initial increase in surface roughness upto a critical time and then a decrease in roughness for higher durations was observed. A decrease in surface roughness with increasing fluence, beyond a critical fluence, has also been observed for MeV Sb implantation in Si(100) [12] and for keV

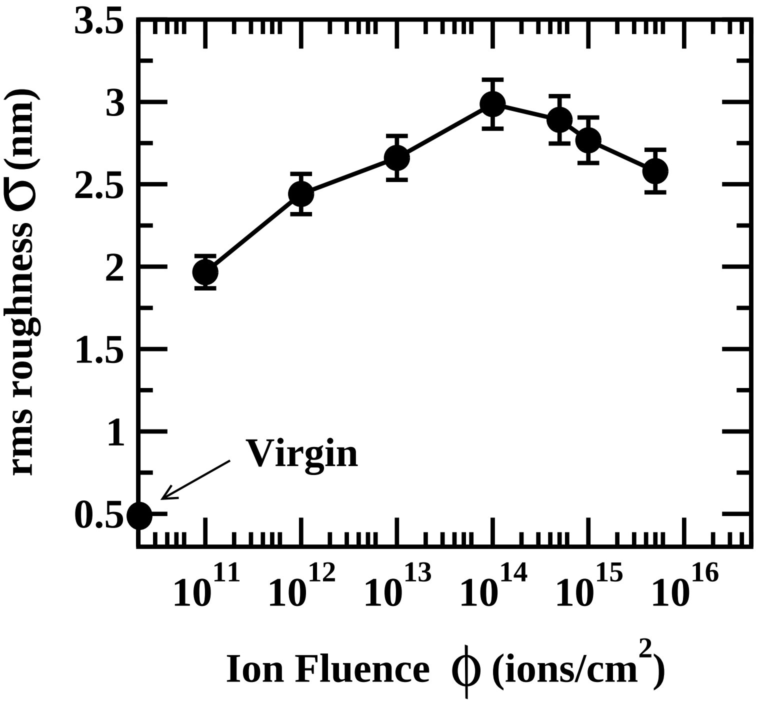

Figure 4.6: The rms surface roughness (σ) of the Sb implanted InP(111) surfaces, measured using SPM, is plotted as a function of Sb ion fluence. Data for the virgin sample is also shown.

implantations of P and As in amorphous films [13].

Comparing the surface roughness after 1.5 MeV irradiation (fig. 4.6) with that after keV irradiation (shown in fig. 3.6 of chapter-3), we observe that at the fluence of 5×10^{15} $ions/cm^2$ (maximum fluence studied for MeV irradiation) the rms surface roughness for keV irradiated surfaces will be smaller. Since the surface roughness is expected to be primarily controlled by the S_n, higher rms roughness for MeV irradiated (S_n = 1.58 keV/nm, S_e = 0.84 keV/nm) surfaces compared to keV sputtered (S_n = 0.34 keV/nm, S_e = 0.05 keV/nm) surfaces is expected. For the 100 MeV Au SHI irradiation [1] on InP (S_n = 378 eV/nm, S_e = 15 keV/nm) a lower surface rms roughness at all fluences compared to 1.5 MeV irradiated samples will be expected due to the lower S_n for SHI irradiations[2]. Although for fluences upto 1×10^{13} $ions/cm^2$ this is seen, for 1×10^{14} $ions/cm^2$ we observe a lower roughness in our case. This is an unexpected result and suggests that at higher fluences factors other than S_n are also playing role. At high fluences, density of electronic excitations increase, covalent bonds in the lattice weaken or get broken. As a result the lattice softens. This softening of the bonds and amorphization of the InP lattice has been shown by our Raman scattering results (discussed in chapter-5). The SHI studies [1] did not investigate the fluences higher than $1 \times 10^{14}\ ions/cm^2$ and also did not observe any decrease in the roughness. Our Raman scattering results, presented in next chapter, indicate the occurrence of amorphization in InP at this fluence.

The surface rms roughness will be insufficient to supply the complete information of the surface modifications and PSD is evaluated to provide quantitative information about the surface roughness both in the vertical and lateral directions. The PSD is also independent of the scan size. The PSD function is a 2-dimensional Fourier transform of the surface and is defined by [14]:

$$\gamma = \frac{1}{area}\left|\int\int \frac{d^2r}{2\pi} e^{-iq.r}\langle h(r)\rangle_t\right|^2, r = (x, y) \tag{4.2}$$

where q is the spatial frequency and *h(r)* is the height at the position *r*. SPM images of fig. 4.1 have been utilized for PSD analysis. These images have been acquired in the tapping mode with 256 × 256 data points. With the image size of $10\mu m$, for 2D isotropic PSD analysis, frequencies range from minimum frequency $q_{min} = \frac{1}{10\mu m} = 0.1\mu m^{-1}$ to the maximum frequency $q_{max} = \frac{256/2}{10\mu m} = 12.8\mu m^{-1}$. The PSD curves of 1.5 MeV Sb^{2+} ion implanted InP surfaces for the fluence ranging from 1×10^{11} to $1 \times 10^{15}\ ions/cm^{-2}$ are shown in fig. 4.7. The PSD curve for the un-irradiated (virgin) InP surface is also shown. The power spectra of fig. 4.7 can be divided into two distinct regions: the horizontal low frequency part resembles the uncorrelated white noise, while the straight line high frequency part represents the correlated surface features. The intensities of the low frequency plateau indicate that the roughening of the ion implanted surface is caused predominantly due to the uncorrelated white noise in the low frequency regions. Corrugation becomes small for points separated by a length larger than the correlation length ,q_0, and the surface can be considered as flat. Thus, it is expected that the PSD function should be q independent for $q < q_0$, while it should decrease for $q > q_0$. At $q > q_0$, no special value of spatial frequency q is

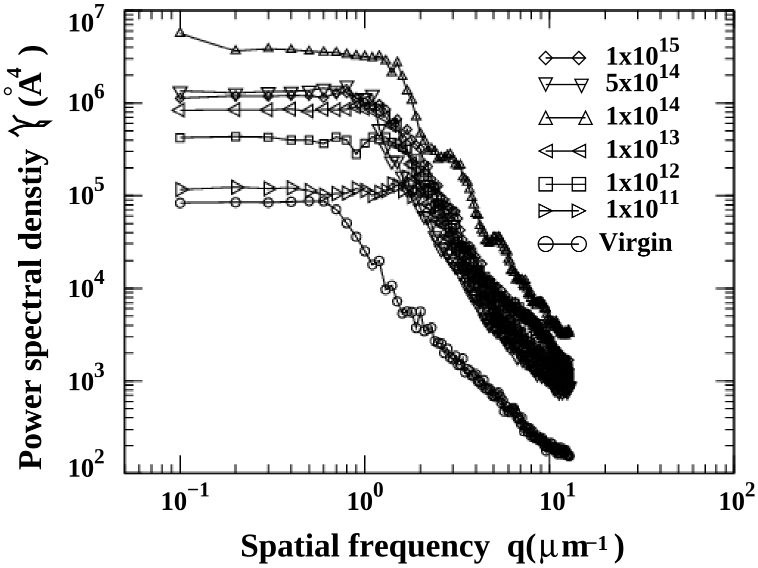

Figure 4.7: Plots of power spectral density (PSD) function vs spatial frequency q of InP surfaces for the virgin sample as well as after implantation of InP(111) with 1.5 MeV Sb ions at various fluence.

the characteristic of the surface morphology and the PSD curve displays a power-law dependence [3]:

$$\gamma = Aq^{-n} \tag{4.3}$$

where A is a constant, and n is a real number. The slope of the PSD function, in fig. 4.7, for $q > q_0$, evolves as $q^{-3.18}$ for a fluence of 1×10^{11} $ions/cm^{-2}$. For the un-implanted (virgin) surface an n of 2.01 has been found. The value of n consistently increases for increasing Sb fluences in InP upto 1×10^{14} $ions/cm^{-2}$. The values of n are 3.57, 3.68 and 4.36 for fluences of 1×10^{12} 1×10^{13} and 1×10^{14} $ions/cm^{-2}$, respectively. For higher fluences of 5×10^{14} and 1×10^{15} $ions/cm^{-2}$, the values of n decrease slightly and are found to be 3.81 and 3.75, respectively. Moreover, the variation in magnitudes of the PSD function indicate the perturbations on the ion implanted surface which increase upto the fluence of 1×10^{14} $ions/cm^{-2}$ and decrease for higher fluences. For InP surfaces irradiated by 100 MeV Au^{8+} ions the PSD function (for $q > q_0$) evolves as $q^{-2.4}$ for the fluence of $1 \times 10^{12} ions/cm^2$ and as $q^{-3.6}$ for

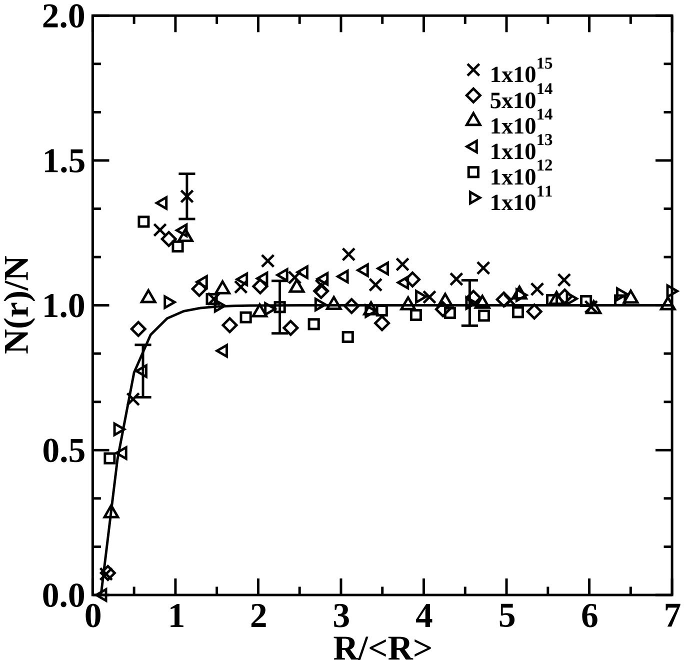

Figure 4.8: Scaled radial distribution function for finding the surface-nanostructure separated by a distance r from a given nanostructure. The radial distribution is shown for all fluences. The solid line is given by $1 - \left(\frac{K_0(r/\sqrt{D\tau})}{K_0(r_0/\sqrt{D\tau})}\right)$ where K_0 is the modified Bessel function of order zero, and $D\tau \sim 1/4\pi N$, with $\sqrt{N} \sim 1/\langle R\rangle$ [5]. The error bars denote the standard error in measurement

$1 \times 10^{14} ions/cm^2$ [1]. In a study by Eklund *et al.* it has been found that diffusion dominated surface smoothening processes lead to a q^{-4} dependence for large spatial frequencies in PSD [3]. Thus, in the present study, for fluences of $1 \times 10^{12} ions/cm^2$ and higher, surface diffusion seems to be playing a dominating role in smoothening the MeV Sb implanted surfaces of InP.

For large diffusion rates during thin film growth, Bartlet and Evans have proposed the scaling relation for the island separation distribution, N(r), which gives the probability of finding an island center separated by a distance, r, from the center of another island [5]. We apply this theory here to investigate the structure formation after MeV Sb implantation at InP surfaces. The N(r) is [5]:

$$N(r) \simeq Nf\left(\frac{r}{\langle R\rangle}\right) \tag{4.4}$$

where N is the density of islands and $\langle R\rangle \sim \frac{1}{\sqrt{N}}$ is a measure of the average separation between island centers, if they are isotropic and uniformly distributed. The scaling function, $f\left(\frac{r}{\langle R\rangle}\right)$, has the property that $f\left(\frac{r}{\langle R\rangle}\right) \rightarrow 0$ for $r \rightarrow r_0$ and $f\left(\frac{r}{\langle R\rangle}\right) \rightarrow 1$ for $r \rightarrow \infty$, where r_0 is the average radius of the island. The Radial Separation Distribution has been calculated for the nanostructures that form on InP surfaces (as seen fig. 4.1) after MeV implantation at various fluences. Collapse of the separation distribution onto a single curve is observed for all the Sb fluences in fig. 4.8. Moreover, it is observed that the Radial Separation Distribution for the fluence of 1×10^{11} in fig. 4.8, closely resembles the theoretical curve representing the functional form of the radial distribution for an isotropic noninteracting system, obtained by solving the differential equation which describes two-dimensional diffusion [5] and is shown by a solid line in fig. 4.8. Thus, at 1×10^{11}, the distribution of nanostructures on the InP surface is random. However, for higher fluences (in fig. 4.8), at $r \approx \langle R\rangle$, we observe an increased probability of nanostructures compared to uniform-random distribution. This is a surprising result in that the ion beam related defect distribution on InP surface is expected to be random. Clustering of nanostructures at $r \approx \langle R\rangle$ suggests an increased nanostructure density in this region. This may be the consequence of diffusion which is present on the ion implanted InP surfaces (as seen in fig. 4.7). Our Raman scattering results (presented in next chapter) indicate that MeV Sb implantation also leads to the creation of stress in the InP lattice [15, 16, 17]. This stress, in addition to surface diffusion, may also be responsible for the clustering of nanostructures. Evaluation of Radial Separation distributions has never been undertaken on ion beam modified surfaces. However, Radial Distribution exhibits clustering of strained InAs islands after thin film growth of InAs on GaAs(100) [18] as well as for InP islands grown on InGaP/GaAs(100) [19]. Clustering of these islands during film growth was shown to be related to the strain caused by the mismatch between the lattice constants of the overlayer and the substrate [18, 19].

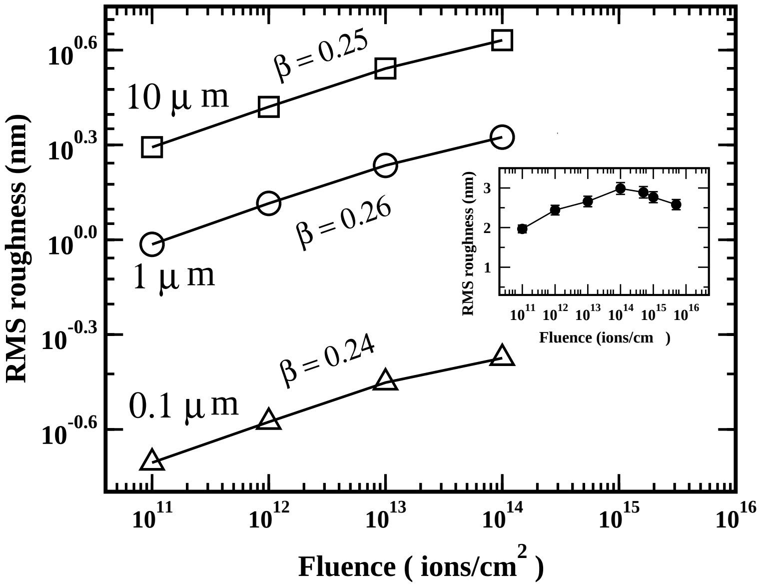

Figure 4.9: The log-log plot of rms roughness as a function of ion fluence is shown at various length scans (L) of $10\mu m$, $1\mu m$ and $0.1\mu m$. The solid lines show power law fit to data. Inset shows the rms roughness as a function of ion fluence.

4.3.2 Studies of surface evoluation due to ion irradiation via the scaling parameters

Figure 4.9 shows the log-log plot of rms surface roughness as a function of ion fluence. The inset of fig. 4.9 shows that although there is an increase in roughness in early times, there is a slight decrease in roughness beyond a critical fluence of 1×10^{14} $ions/cm^2$. Figure 4.9 shows rms roughness only for fluences below the critical fluence(1×10^{14} $ions/cm^2$). The log-log plots have been shown for three representative scan lengths (L) of $10\mu m$, $1\mu m$ and $0.1\mu m$. As expected, the rms roughness depends on L and increases with increasing L. The linear characteristic of the log-log plots, for all L, indicate that the rms roughness increases with fluence according to a power-law. By fitting the power-law behaviour to rms roughness as $\sigma(L,t) \sim t^{\beta}$, we obtain the growth exponent β to be 0.25, 0.26 and 0.24 for L=10, 1 and 0.1 μm, respectively, in early time regimes. The average value of $\beta = 0.25 \pm 0.04$, obtained here, is close to that found in the Kardar et al. ($\beta = 0.25$) [20] or the Mullins diffusion equation ($\beta = .25$) [21]. As seen in the inset of fig. 4.9, the smoothening of the irradiated surfaces, beyond the fluence of 1×10^{14} $ions/cm^2$, suggest the presence of a negative growth exponent. This exponent has been determined to be $\beta = -0.21$ for fluences higher than this critical fluence.

According to the theoretical expectations [8] for short erosion time $t < t_c$ the surface morphology is described by the linear BH model and the surface width should increase exponentially while for $t > t_c$ the surface width still increases but at a much smaller growth rate until it reaches saturation. Our experimental results show that in early time regime, below 1×10^{14} $ions/cm^2$, the surface morphology is not described by an exponential increase rather it shows a powerlaw behaviour. As shown by Cuerno et al. [22] a power law behaviour can be a consequence of various non-linear terms which are neglected in the BH model[6]. Similar powerlaw behaviour has been observed by [23] for $t < t_c$. Moreover beyond the fluence of 1×10^{14}, the rms roughness decreases as seen in fig 4.9 (inset).

We have also measured the roughness exponent, α, by plotting the roughness of the ion irradiated surface as a function of the scan length L, for different bombarding fluences. The results are shown in fig. 4.10 for the critical fluence 1×10^{14} $ions/cm^2$ as well as for higher fluences. It is seen that the local width increases as $\sigma \sim L^\alpha$ before it saturates. The roughness exponent α is obtained from a linear fit of the unsaturated region of σ versus L plot. It is found that $\alpha = 0.84 \pm 0.08$ and it is independent of ion fluence. In the limit of long time and length scales, equation 1.13 (in chapter-1) is equivalent to the Kardar-Parisi-Zhang (KPZ) equation [7]. The exponents for the KPZ- type scaling are $\alpha = 0.38$ and $\beta = 0.25$, respectively. Although the β seen in the present study is similar to KPZ for $t < t_c$, α, in the present study is much larger.

The time scaling behaviour of the nano patterns wavelength is given by $\lambda \sim t^\gamma$. Inset of fig. 4.11 shows the Power Specral Density (PSD) distribution as a function of spatial frequency, q, for some representative fluences(taken from fig. 4.7). The variations in PSD indicate the modifications in the patterning behaviour with increasing fluence. The λ here has been measured by utilizing the first maximum of the power spectral density distribution. Figure 4.11 shows the log-log plot of λ as a function

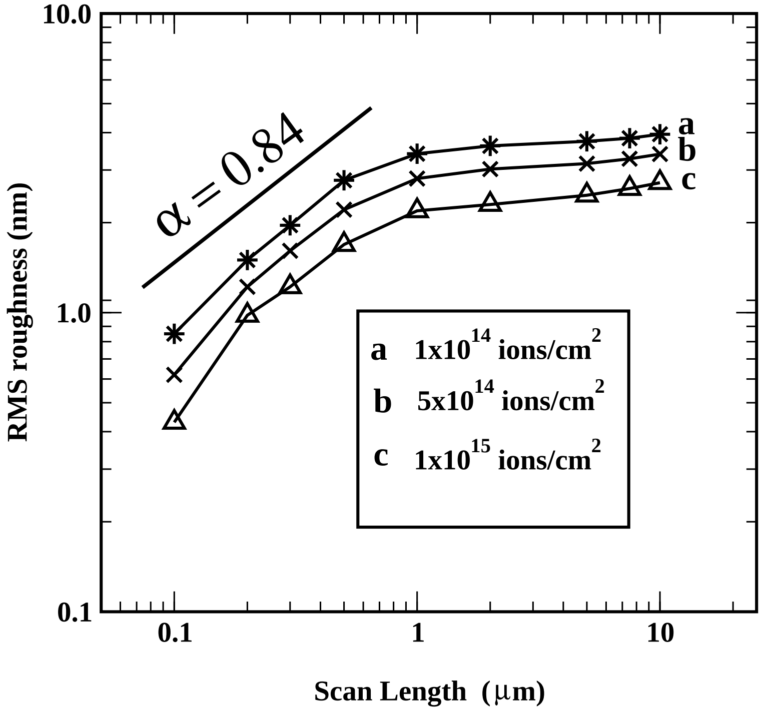

Figure 4.10: Showing the rms roughness versus scan length L at different fluences. The solid lines represent the best power law fit $\sigma \sim L^{\alpha}$ with $\alpha = 0.84 \pm 0.08$

of ion fluence. By utilizing this log-log plot a $\gamma = -0.58 \pm 0.05$ is obtained. This suggests a significant redistribution on InP surface [21]. For keV irradiation of InP surfaces a positive $\gamma = 0.14$ [24] was obtained. However for structure formation on Si negative γ has been observed [25]. Dependence of λ on time or fluence suggests that the linear BH model is not applicable for these surfaces.

The evolution of the surface morphology during ion bombardment will be governed by a balance between the roughening and the smoothening processes. The random arrival of the ions on the surface constitutes the stochastic surface roughening. Surface diffusion, viscous flow and surface sputtering etc. contribute towards the smoothening of the surface [3]. The mechanism for the formation of surface damage is also postulated as a result of cascade collisions due to nuclear energy loss. S_n has been considered to be mainly responsible for the surface modifications of InP after

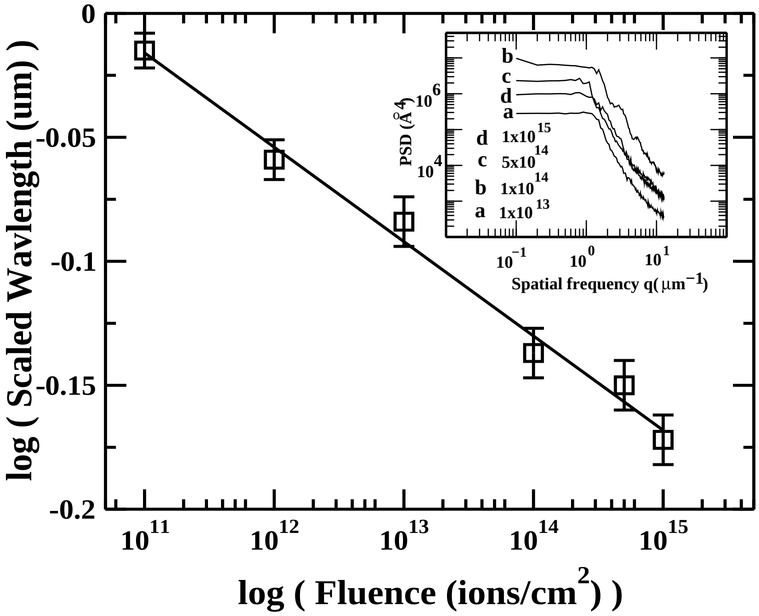

Figure 4.11: The wavelength (λ) of the implanted surfaces, measured using SPM, is plotted as a function of ion fluence. Inset shows the power spectral density distributions for some representative fluences.

2 MeV Se implantation [26] and high energy (~100 MeV) Au irradiation [1]. In the present study also S_n seems to be the dominating factor in the creation of the nanostructure after Sb implantation. The 4.5 MeV Au implantation in HOPG [27] results in protrusions and features similar to the nanostructures seen here on InP surfaces. The mechanism for the formation of the surface features, on HOPG, was also S_n dominated. Differential sputtering of InP surfaces leading to In-rich zones was suggested to be a possibility for the nucleation of surface structures after keV irradiation (discussed in chapter-3) . Similar scenario may be taking place at MeV energies also. Thus, S_n related processes, differential sputtering of a component, and the presence of tensile stress as observed in Raman spectra presented in next chapter, may be all together responsible for creating the nano-sized defects observed here after MeV Sb implantations.

4.4 Summary and conclusions

In this chapter, the modifications in the surface morphology of InP(111) have been examined after 1.5 MeV Sb implantation. The InP surfaces display nano-sized defect structures. The height and size distributions of the nanostructures have been studied here. For fluences of 1×10^{11} - 1×10^{15} $ions/cm^2$, several nanostructures of sizes smaller than 100 nm and lower than 4 nm have been observed. Larger and bigger defects are observed to be embedded with smaller nano-sized defects in the SPM images. The surface roughness initially increases upto the Sb fluence of 1×10^{14} $ions/cm^2$. For higher fluences a decrease in surface roughness is observed. Power Spectral Density has been evaluated using the SPM images. It provides a scaling exponent $n= 4.36$ for the fluence of 1×10^{14} $ions/cm^2$ suggesting that diffusion processes are crucially determining the evolution of InP(111) surfaces after MeV implantations. Radial Separation Distributions, of the nanostructures on the InP surfaces, collapse on a curve for all the fluences demonstrating that the scaling theories applicable for thin film growth may also be applicable for ion beam bombarded surfaces. Random distribution of nanostructures for 1×10^{11} $ions/cm^2$ but a non-uniform distribution at higher fluences is also observed. The scaling exponents: roughness and growth exponents have been determined. For early times, i.e. for fluences lower than 1×10^{14} $ions/cm^2$ a $\beta = 0.25$ has been obtained. For fluences higher than the critical fluence, of 1×10^{14} $ions/cm^2$, $\alpha = 0.84$ is obtained. We further observe that the wavelength of the patterns evolves as $\lambda \sim t^{-0.58}$.

Bibliography

[1] J.P. Singh, R. Singh, N.C. Mishra, D. Kanjilal, and V. Ganeshan, J. Appl. Phys. **90**, 5968 (2001); Nucl. Instru. B **179**, 37 (2001).

[2] G.K. Mehta, Vacuum **48** (1997) 957.

[3] E.A. Eklund, E.J. Snyder, and R.S. Williams, Surf. Sci. **285** 157 (1993).

[4] Z.J. Liu, N. Jiang, Y. G. Shen, Y.W. Mai, J. Appl. Phys. **92** 3559; A.E. Litand John E. Sanchez, J. Appl. Phys. **85** 876.

[5] M.C. Bartelt and J.W. Evans, Phys. Rev. **B46**, 12675 (1992), J.W. Evans and M.C. Bartelt, Surf. Sci. **284**, L437 (1993) M.C. Bartelt, M.C. Tringides and J.W. Evans, Phys. Rev. **B47**, 13891 (1993).

[6] R. Mark Bradley and James M. E. Harper, J. Vac. Sci. Technol. A **6**, 2390 (1988).

[7] R. Cuerno and A.-L. Barabasi, Phys. Rev. Lett. **74** 4746 (1995).

[8] B. Kahng, H. Jeong and A.-L. Barabasi, Appl. Phys. Lett **78**, 805 (2001).

[9] J. P. Biersack and L. G. Haggmark, Nucl. Instr. and Meth. **B174**, 257 (1980).

[10] J.F. Gibbons, Proc. IEEE **60**, 1062 (1972).

[11] O. Herre, W. Wesch, E. Wendler, P.I. Gaiduk. F.F. Komarov, S. Klaumunzer and P. Meier, Phy. Rev. B. **58**, 4832 (1998).

[12] Soma Dey, Dipak Paramanik, V.Ganesan and Shikha Varma, Appl. Sur. Sci. **253** , 1116 (2006).

[13] R. Edrei, E.N. Shauly, A. Hoffman, J. Vac. Sci. Tech. A **20**, 344 (2002).

[14] R. Petri, P. Brault,O.Vatel, D. Henry, E .Andre, P. Dumas, and F. Salvan, J.Appl. Phys.**75**, 7498 (1994) .

[15] D. Paramanik, A. Pradahn, S. Varma, J. Appl. Phys. **99**, 014304(2006).

[16] Dipak Paramanik and Shikha Varma, J. Appl. Phys. **101**,023528 (2007).

[17] Dipak Paramanik and Shikha Varma, J. Nanosci. and Nanotech. **07**, 2197 (2007)

[18] V.Bressler -Hill, S. Varma, A. Lorke, B.Z. Nosho, P.M. Petroff and W.H. Weinberg, Phys. Rev. Lett. **74**, 3209 (1995) .

[19] S. Varma, C.M. Reaves,V.Bressler -Hill, S. P. DenBaars, and W.H. Weinberg, Surf. Sci. **393**, 24 (1997).

[20] M. Kardar, G. Parisi and Y.C. Zhang, Phys. Rev. Lett, **56**, 889 (1986).

[21] W.M. Mullins, J. Appl. Phys. **28**, 333 (1957).

[22] M.A. Markeev, R. Cuerno, A.L. Barabasi, Nucl. Instr. and Meth B. **197**, 185 (2002).

[23] T.C. Kim, M.H. Jo, Y. Kim, D.Y. Noh, B. Kahng and J.S. Kim Phys. Rev. B. **73** 125425 (2006)

[24] M.Xu and C.Teichert, Jour. Appl. Phys.**96**,2244 (2004).

[25] Eric Erlebacher, M. Aziz, E. Chason, M.B. Sinclair and J. A. Floro Phys. Rev. Lett. **82**, 2330 (1999)

[26] W. Wesch, E. Wendler, T. Bachmann, and O. Herre, Nucl. Instru. Meth. Res. B. **96**, 290 (1995).

[27] Y. Wang, Y. Kang, W. Zhao, S. Yan, P. Zhai and X. Tang, J. Appl. Phys. **83**, 1341 (1998).

Chapter 5

Raman Scattering Characterization and Electron Phonon Coupling Strength for MeV implanted InP(111)

5.1 Introduction

During implantation, a projectile while moving forward produces vacancies and interstitials, loses energy primarily due to electronic encounters and is finally deposited at its range governed by its mass and implant energy [1]. At MeV energies, nuclear energy loss (S_n) processes are expected to be dominantly responsible for the material modifications. Defects and strains can get produced, via S_n, causing the modifications in properties of host material [2, 3, 4, 5]. Formation of defects as well as the presence of impurity atoms can lead to stress in the planes of the single crystal or changes in the force constants. Corresponding shifts in the phonon frequencies are reflected in the Raman spectra. Moreover, the damage produced due to defects can cause phonon confinement leading to a reduced phonon coherence length as k=0 selection rule is relaxed, giving rise to an asymmetric broadening in Raman peak. The Raman spectrum thus contains signature of both: the stress and the reduced phonon coherence length due to disorder in the lattice. Raman Scattering, thus, is a powerful tool for investigating and monitoring the radiation induced lattice modifications during ion implantation. A few studies have investigated the modifications in InP crystals after implantations by Raman scattering technique[6, 7, 8, 9, 10, 11, 12, 13, 14, 15]. However, all these studies investigated the (100) InP where TO mode is forbidden. Katsumata etal. have investigated MeV implantation of Yb ions in InP(100) [16].

For InP, phonon dispersion studies indicate [17, 18] that LO branch is almost as flat as TO branch for the entire Brillouin zone. Moreover, Overlap Valence Shell Model [18] results display two very sharp and well separated features corresponding to second order LO (2LO) and second order TO (2TO) phonon modes with high density of states around TO(Γ) and LO(Γ). Consequently, second order phonon modes of InP can be investigated and some reports indicate that the second order modes may be more sensitive, compared to first order, of lattice disorder, stress and lattice modifications after implantation [7]. However, very few studies have investigated these second order Raman modes [7, 10, 11, 12, 14]. Moreover, all of these studies have investigated InP(100) after keV implantations. There are no studies in literature where second order Raman modes have been investigated after keV or MeV implantation of InP(111) crystals.

At the surface of III-V semiconductor compounds a space charge layer, concentration of high mobility free-electron gas, may exist. If the frequency of this free-electron plasma excitations - plasmons is close to the frequency of LO phonons, the two excitations can interact via their macroscopic electric fields and can form LO phonon-plasmon coupled (LOPC) mode. In n-type InP(100), an intense and well defined L^{-} feature due to LOPC mode has been observed [6]. A few studies have investigated the scattering of light by free carriers in zinc- blende semiconductors [19] and some models have been proposed that analyze the coupling between LO phonons and plasmons. However, there are very few reports for doped InP crystals [6] and none of these studies focus on the evolution of LO-plasmon coupling in InP(111) after implantation.

Electron-phonon coupling is a very important factor in understanding the nonlinear optical properties of the crystalline materials. For polar materials, the dominant coupling is Fröhlich type between the field induced by the vibrational modes and the electronic charge density [20]. Systematic trends in the electron-phonon coupling strengths, with size, have been seen for Quantum Dots of InP by utilizing second order Raman Scattering [21]. However, there are no studies in literature where electron-phonon coupling strengths have been measured after ion implantation.

In this chapter, the first and second order Raman scattering phonon spectra have been utilized to investigate the lattice modifications in InP(111) after implantation with 1.5 MeV Sb^{2+} ions. Studies show that the second order phonon modes better reflect the nature of modifications after implantation. The evolution of both TO and LO modes as a function of ion fluence have been studied. Even at the fluence of 1×10^{11} $ions/cm^2$, modifications in first order as well as second order modes demonstrate the initiation of some damage in InP(111) lattice. Once this occurs, a coexistence of nanocrystalline regions and amorphous zones is observed which leads to the confinement of phonons. An estimation of the phonon coherence length has been done by applying the Phonon Confinement Model (PCM) [22] to the first order Raman peak. Existence of a completely amorphous lattice is noticed for a fluences of $1\times10^{14} ions/cm^2$ and higher. The evolution of LOPC mode, L^-, has also been studied as a function of ion fluence. The effect of implantation on the electron phonon coupling in InP(111) has also been investigated by utilizing the second order Raman modes. It is found that the strength of coupling reduces as the size of nano-crystalline zones, in the implanted lattice, decrease.

5.2 Experimental

A mirror polished (111)-oriented InP single crystal wafer was used in the present study. The samples were implanted at room temperature with a scanned beam of 1.5 MeV Sb^{2+} ions at various fluences ranging from 1×10^{11} to 5×10^{15} $ions/cm^2$. The average Sb flux was 0.02 $\mu A/cm^2$. This current was measured directly on the target after suppressing the secondary electrons by applying a negative bias of 200V to a suppressor assembly around the target. The implantations were performed with the samples oriented 7^o off-normal to the incident beam to avoid channeling effects. Monte Carlo simulations were performed for 1.5 MeV Sb implantation in InP using the SRIM'06 code and the mean projected range of Sb-ion distribution was found to be 400 nm [23].

Raman scattering measurements were performed using a SPEX 1877E Triplemate Spectrometer with a liquid nitrogen cooled, charged coupled device array. The laser power was controlled to avoid laser annealing effect on the sample. Raman experiments were carried out at room temperature using the 514 nm line of an argon ion laser in the backscattering geometry. At this wavelength the penetration depth of the light is estimated to be about 100 nm in InP. All the spectra were acquired in the backscattering geometry.

5.3 Results and Discussion

Figure 5.1 shows the as-implanted first order Raman Spectra from the InP(111) samples implanted at various fluences. The spectrum from a virgin (un-implanted) InP is also shown. The spectra have been shifted vertically for clarity, but the intensity scale is the same for all the spectra. The spectrum of the virgin InP (fig.5.1a) shows the characteristic LO and TO Raman modes of crystalline InP(111) [24]. The features at 305 cm^{-1} and at 347 cm^{-1} are assigned to the TO and the LO phonon modes, respectively. For the virgin InP(111) we also observe an additional L$^-$ mode, near 320 cm^{-1}, as a shoulder near TO mode. This broad phonon feature can be assigned as L$^-$ LO - phonon plasmon coupled (LOPC) mode. It is well known that in polar semiconductors, like InP, free charge couples with LO modes and forms LOPC-like modes [19]. For InP(100) where TO mode is forbidden, L$^-$ mode has been observed as sharp feature near 306 cm^{-1} [13] as well as at 308 cm^{-1} [25]. The sequence of spectra in fig. 5.1 gradually evolve with increasing Sb fluence. The Raman spectrum from a sample implanted with 1×10^{11} $ions/cm^2$ shows broader LO and TO modes (fig. 5.1b) compared to the virgin sample. Both the features now also exhibit decreased intensity and increased asymmetricity. Moreover, both LO and TO modes,

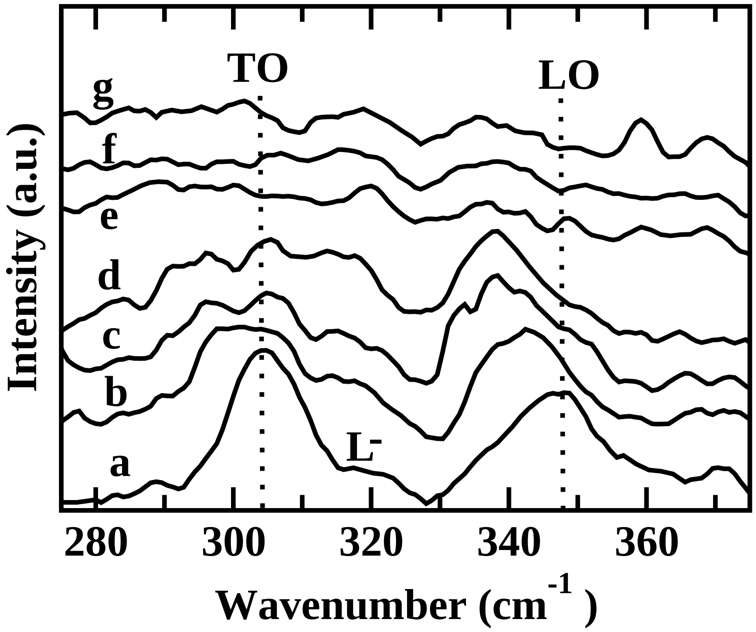

Figure 5.1: First order optical Raman spectra of virgin InP (a) and 1.5 MeV Sb implanted InP at ion fluences of 1×10^{11} $ions/cm^2$ (b), 1×10^{12} $ions/cm^2$ (c), 1×10^{13} $ions/cm^2$ (d), 1×10^{14} $ions/cm^2$ (e), 5×10^{14} $ions/cm^2$ (f) and 1×10^{15} $ions/cm^2$ (g)

after implantation, are shifted towards lower wave numbers compared to the modes in the virgin InP. All these changes reflect the modifications in the InP lattice due to the defects created during implantation. With increasing fluence, we observe a further decrease in intensity of the TO and LO modes.

We observe softening as well as asymmetrical broadening in both LO and TO modes with increasing fluence. Both the modes exhibit shifts towards lower wave numbers. The shifts in the peak positions of Raman spectra can be affected by the residual stress as well as by phonon confinement. The contributions due to the two effects can however be deconvoluted [26]. Spatial Correlation model related to k-vector relaxation induced damage shows [27] that when disorder is introduced into the crystal lattice by implantation, the correlation function of the phonon-vibrational modes become finite due to the induced defects and consequently the momentum $k = 0$ selection rule is relaxed. Consequently, the phonon modes shift qualitatively to lower frequencies and broaden asymmetrically as the ion fluence is increased [2]. The reduction in the intensity, shifts towards lower frequencies as well as the asymmetrical broadening of the features with increasing ion fluence, as observed in fig. 5.1, are due to the residual defects created in InP lattice via implantation. Accordingly, these two features are also referred to as DALO and DATO, respectively, for disorder activated (LO) and (TO) modes. For the fluences of $1{\times}10^{14}$ $ions/cm^2$ and higher, no DALO or DATO modes are observed in fig. 5.1 suggesting that at this stage InP lattice undergoes crystalline/amorphous (c/a) phase transition and becomes amorphized. These results are different than the studies of 150 keV Si^+ [11] or 80 keV Mg [10] implantation in InP(100) where no noticeable changes compared to the virgin were seen upto the fluence of $1{\times}10^{12} ions/cm^2$ and the first signatures of disorder were observed after the fluence of $5{\times}10^{12} ions/cm^2$. In contrast to results seen in the present study as well earlier studies [10, 11], c/a transition at very low fluence of $1{\times}10^{13} ions/cm^2$ was seen after keV implantation of Zn in InP(100) [12]. For 3 keV Ar ion irradiation of InP(111), (discussed in chapter-3), c/a transition is observed at 24×10^{15} $ions/cm^2$. For 2 MeV Se implantation in InP(100), some damage after $1{\times}10^{12} ions/cm^2$ has been reported using channeling experiments[28]. The overall Raman scattering, after implantation, is influenced by the presence of the damaged/amorphised zones that get formed in the crystalline lattice. With increasing fluence, the crystalline regions reduce in size whereas the amorphous and damaged zones grow bigger. The disorder is usually a consequence of damage zones that form due to the point defects and/or dislocations created after MeV implantations. With increasing fluence the damaged zones in the lattice begin to overlap and finally at sufficiently high fluences c/a phase transition may occur leading to a completely amorphised lattice [29].

Figure 5.2 displays the quantitative variations, as a function of ion fluence, in intensity, linewidth and position of first order Raman modes of InP(111) after Sb implantation. In fig. 5.2a the Raman intensity for TO and LO modes, normalized with respect to the intensity from the virgin sample, are shown. For both the modes, we observe a decrease in intensity for increasing fluence. For TO mode, however, the decrease is larger and faster. The Full Width at the Half Maximum (FWHM) for both the modes are shown in fig 5.2b. We observe an increase in the linewidths for

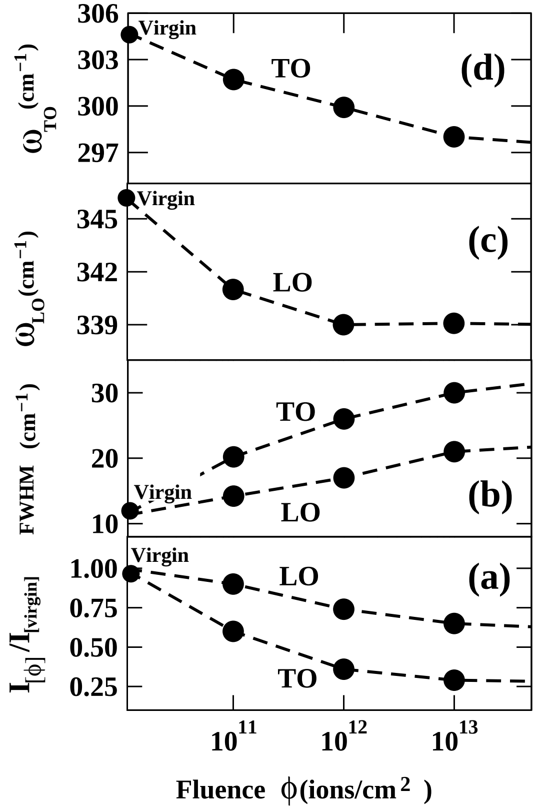

Figure 5.2: Evolution of first order LO and TO modes: The intensity of both LO and TO modes normalized with respect to virgin (a), FWHM of both LO and TO modes (b) the shift in position (ω) of LO mode (c) and shift in position (ω) of TO mode (d) are shown as a function of ion fluence. Data for the virgin sample are also shown.

both the modes as the fluence is increased. Again, the increase is more pronounced in TO mode. The widths of TO and LO modes, after the fluence of 1×10^{13} $ions/cm^2$, are 30 and 20 cm^{-1}, respectively. In contrast, much smaller and same linewidths for LO and TO modes ($\sim$ 7 cm^{-1}) have been observed after keV implantation at this fluence [8]. The positions of the LO and TO modes are shown in figs. 5.2c and 2d, respectively. Although for the virgin sample the positions for LO and TO modes were 347 and 305 cm^{-1}, respectively, after the fluence of 1×10^{13} $ions/cm^2$ these mode appear at 339 and 298 cm^{-1}, respectively. The overall shift (ω) is larger and increases more rapidly for LO mode. These shifts indicate that the lattice is under stress due to the creation of defects after implantation. Moreover, the shift of LO and TO modes towards the lower wave numbers suggest that the stress is of tensile nature. Surprisingly, although TO mode showed larger variation in intensity and width compared to the LO mode (in fig. 5.2a,b), the overall shift is larger for LO mode (∼8 cm^{-1}). With LO being a more surface sensitive mode, due to the Fröhlich interactions [30], lower intensity and FWHM of LO mode suggest that the lattice has undergone less modifications on the surface than in bulk. This, however, will lead to a larger stress on the surface. Higher shifts in LO mode show that this is indeed happening. Moreover, the shift being towards the lower wavenumbers suggests that the surface is under large tensile stress. Similar large shifts, in LO mode, towards lower wave numbers have also been observed for InP Quantum Dots [21].

Figure 5.3 shows the variations in intensity, width and position of L^- plasmon-phonon coupled (LOPC) mode as a function of ion fluence. The intensity of L^- mode increases upto the fluence of 1×10^{13} $ions/cm^2$. For higher fluences, L^- feature is not visible. As seen in fig. 5.1, the c/a transition occurs in InP(111) lattice at the fluence 1×10^{14} $ions/cm^2$. The disappearance of L^- mode may reflect the capture of free carriers by defects due to the creation of amorphised zones after ion implantation. In fig 5.3b, the FWHM of L^- mode is seen to decrease with increasing fluence. This mode, thus, becomes sharper and more intense with increasing fluence. This is as expected since LOPC can become stronger with increasing carrier density. The position of L^- mode shifts towards lower wave numbers with the increasing fluence. As expected, the frequency of L^- mode asymptotically approaches TO frequency [19]. With L^- occurring at 320 cm^{-1} for the virgin sample and at 316 cm^{-1} after the fluence of 1×10^{13} $ions/cm^2$, an overall shift of about 4 cm^{-1} is observed for this mode.

Figure 5.4 shows the second order Raman spectra of InP(111) after implantation with Sb ions at various fluences. For the virgin InP(111) a distinct triplet at 617, 650 and and 682 cm^{-1} is observed (fig. 5.4a). These features correspond to the 2TO, LO+TO and 2LO modes, respectively. The evolution of all these features, as a function of ion fluence, are displayed in fig. 5.4. It has been shown that the scattering volume for the second-order modes comprises the volume effectively probed by the exciting laser and hence these modes better reflect the nature of lattice modification

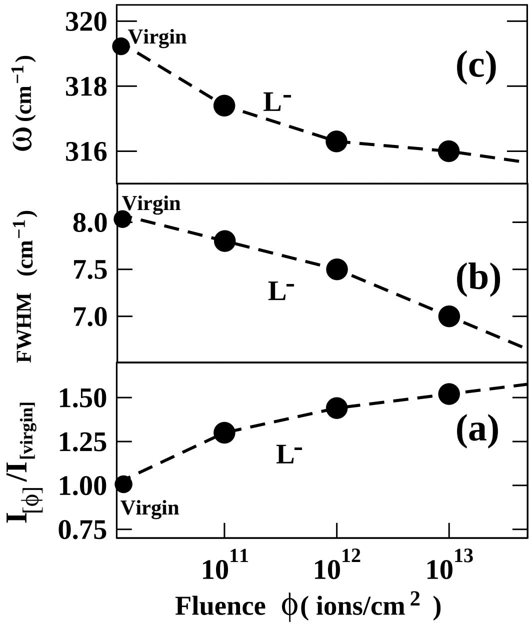

Figure 5.3: Evolution of L$^-$ mode: The intensity of L$^-$ mode normalized with respect to virgin (a), FWHM (b) and the shift (ω) in position (c) are shown as a function of ion fluence. Data for the virgin sample are also shown.

than first order modes in zinc-blende (100) structures [7].

Figure 5.5 shows the variations in the intensity, width and position of second order TO and LO modes, as a function of ion fluence. Figure 5.5a shows the intensity of 2TO and 2LO modes, at various fluences, normalized with respect to the respective intensities from the virgin sample. For both the modes, we observe a reasonable decrease in intensity at the fluence of 1×10^{11} $ions/cm^2$. This result is in contrast to previous studies after keV implantation in InP(100) where no significant modifications in second order Raman modes were observed below the fluence of 5×10^{12} $ions/cm^2$ [10, 11]. For both 2LO and 2TO modes, we also observe a further decrease in the intensity with increasing fluence. The reduction of intensity in fig. 5.5a, like first order, is again larger for the 2TO mode than for 2LO. Although the overall decrease in intensity for LO and 2LO modes is similar, 2TO modes exhibit much less decrease

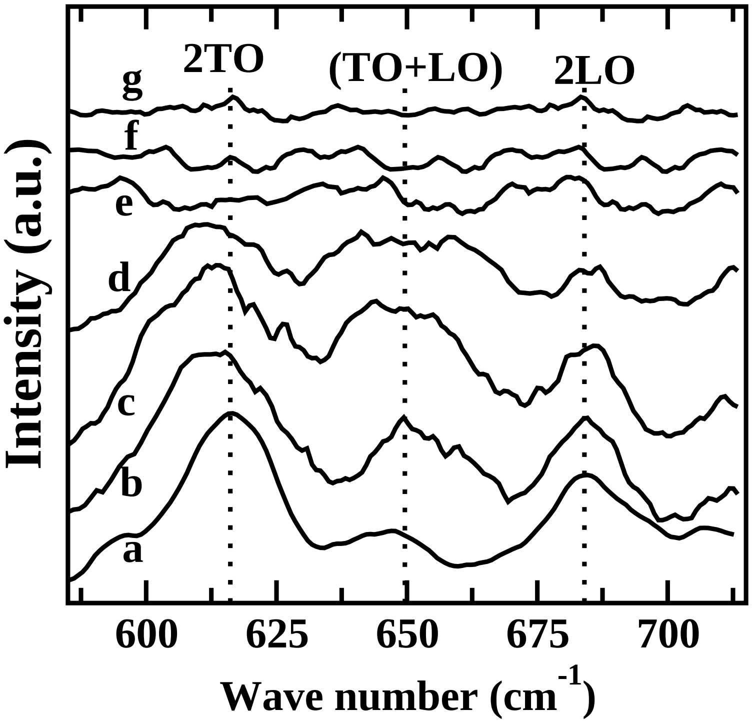

Figure 5.4: Second order optical Raman spectra of virgin InP (a) and 1.5 MeV Sb implanted InP at ion fluences of 1×10^{11} $ions/cm^2$ (b), 1×10^{12} $ions/cm^2$ (c), 1×10^{13} $ions/cm^2$ (d), 1×10^{14} $ions/cm^2$ (e), 5×10^{14} $ions/cm^2$ (f) and 1×10^{15} $ions/cm^2$ (g)

compared to TO mode. At 1×10^{13} $ions/cm^2$, we observe that for TO and 2TO modes the intensities are respectively about 25% and 50% of the intensity from virgin sample. Figure 5.5b shows the widths (FWHM) of 2TO and 2LO features. The widths of 2LO and 2TO modes, for the virgin InP(111), are observed to be 10 and 15 cm^{-1}, respectively. These widths are slightly smaller than those observed for virgin InP(100) where widths for LO and TO modes were found to be 12 and 16 cm^{-1}, respectively [31]. For the virgin InP(111), although 2LO mode is slightly narrower than LO mode, the width of 2TO mode is larger than TO mode. After implantation, the widths of TO and 2TO modes appear similar but the width of 2LO is narrower than LO. Moreover the width of 2LO does not show much variation with fluence after implantation. Similar to first order TO mode, 2TO mode shows larger and more rapid increase in width compared to 2LO mode. The behavior of the shifts in position (ω)

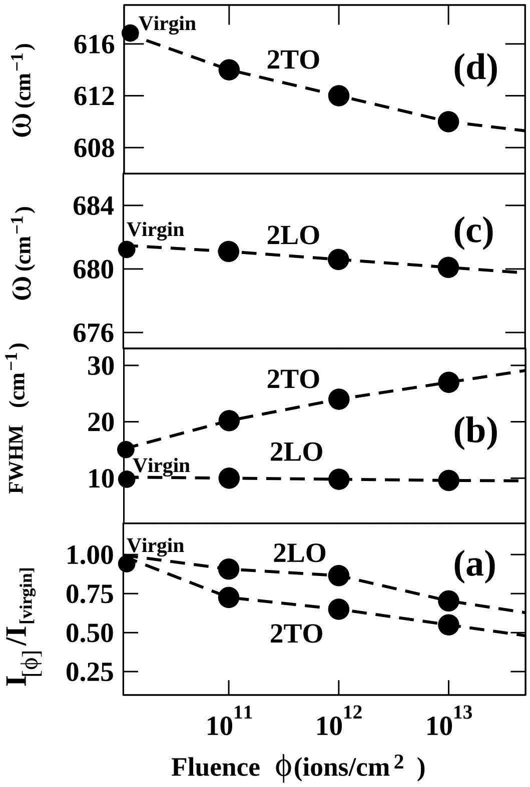

Figure 5.5: Evolution of second order 2LO and 2TO modes: The intensity of both 2LO and 2TO modes normalized with respect to virgin (a), FWHM of both 2LO and 2TO modes (b) the shift in position (ω) of 2LO mode (c) and shift in position (ω) of 2TO mode (d) are shown as a function of ion fluence. Data for the virgin sample are also shown.

of the second order modes is, however, different and unlike first order where LO mode exhibited larger shifts compared to TO mode, 2LO mode shows very little change in its position. Figure 5.5c shows that 2LO mode experiences only a very slight shift (∼2 cm^{-1}) towards the lower wave numbers after the fluence of 1×10^{13} $ions/cm^2$ whereas 2TO mode exhibits a large shift of about 7 cm^{-1} (Fig. 5.5d), similar to those seen for TO mode in fig. 5.2d. The modifications in the second-order Raman modes after implantation, like first-order, are associated with the degradation of the crystalline order in the InP(111) lattice.

The second order optic phonon spectra (in fig. 5.4) also contain a combination

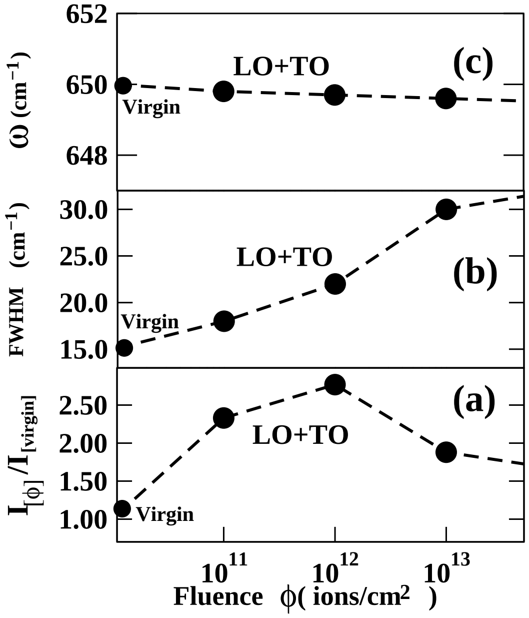

Figure 5.6: Evolution of LO+TO mode: The intensity of LO+TO mode normalized with respect to virgin (a), FWHM (b) and the shift (ω) in position (c) are shown as a function of ion fluence. Data for the virgin sample are also shown.

mode of LO+TO. Figure 5.6 shows the evolution of this combination mode as a function of ion fluence. The overall intensity of the mode initially increases upto the fluence of 1×10^{12} $ions/cm^2$ but decreases for higher fluences. After c/a transition occurring at 1×10^{14} $ions/cm^2$, the combination LO+TO mode is no more visible. The FWHM of the combination mode is 15 cm^{-1} for the virgin InP(111). This width is larger than the linewidth of combination mode (9 cm^{-1}) observed for virgin InP(100) [31]. Surprisingly, though combination mode, seen here, is wider than the previous study [31], the 2LO and 2TO modes are narrower in the present study. The linewidth of the combination mode increases with fluence becoming 30 cm^{-1} after the fluence of 1×10^{13} $ions/cm^2$ (fig. 5.6b). The position (ω) of this mode, however, does not show much shift with increasing ion fluence.

During implantation, the lattice ions are displaced, creating defects and disordered regions in the process. With increasing lattice disorder, the phonon coherence length is reduced and **k**=0 selection rule is relaxed, giving rise to measurable shifts and asymmetric broadening of the Raman peaks [27]. Due to translational symmetry breakdown, PCM developed by Richter et al. [22] can be used to evaluate the phonon confinement length or the average size of the undamaged crystalline regions. Assuming a constant correlation length (L) in the scattering volume, the intensity of the first order Raman band in the scattering volume is given by

$$I(\omega) = \int_0^{2\pi/a_0} \frac{|C(q)|^2 \, 4\pi q^2 dq}{[\omega - \omega(q)]^2 + (\Gamma_0/2)^2} \tag{5.1}$$

where a_0 is the lattice constant of InP (5.586 $\AA$). Γ_0 is the Raman intrinsic line width of the crystalline InP having values of 10.5 and 7.6 cm^{-1} for TO and LO modes, respectively. The weight factor C(q) for the scattering with wave vector q is given by

$$|C(q)|^2 = exp(\frac{-q^2 L^2}{16\pi^2}) \tag{5.2}$$

and the phonon dispersion relation is given by [32]

$$\omega(q) = \omega_A - \omega_B (q/q_0)^2 \tag{5.3}$$

where ω_A is the wave vector of the first order Raman band in the absence of disorder effects and $q_0 = \frac{2\pi}{a_0}$. Neutron scattering data provides ω_B to be 42 and 68 cm^{-1}, respectively, for LO and TO modes [17].

By fitting the experimental LO and TO Raman modes with PCM we have obtained the phonon coherence length, L, of the as implanted samples. Figure 5.7 shows the results of fittings of PCM model to LO mode of Raman spectra, along with respective L values, at various fluences. Raman LO mode from the virgin InP sample is symmetric with an infinite coherence length. A fluence of 1×10^{11} $ions/cm^2$ causes an asymmetricity in the LO mode which can be due to the presence of some disordered or amorphous regions in the InP sample that are large enough for phonon confinement. By utilizing PCM, a phonon coherence length of 66 $\AA$ is obtained, indicating the presence of undamaged InP zones with average crystallite size of this dimension. The shape of Raman LO mode after the fluence of 1×10^{12} $ions/cm^2$ shows a very slight increase in asymmetricity compared to that observed at 1×10^{11} $ions/cm^2$ and displays a coherence length of 56 $\AA$. A highly asymmetric Raman LO mode is observed after the fluence of 1×10^{13} $ions/cm^2$. The phonon coherence length at this

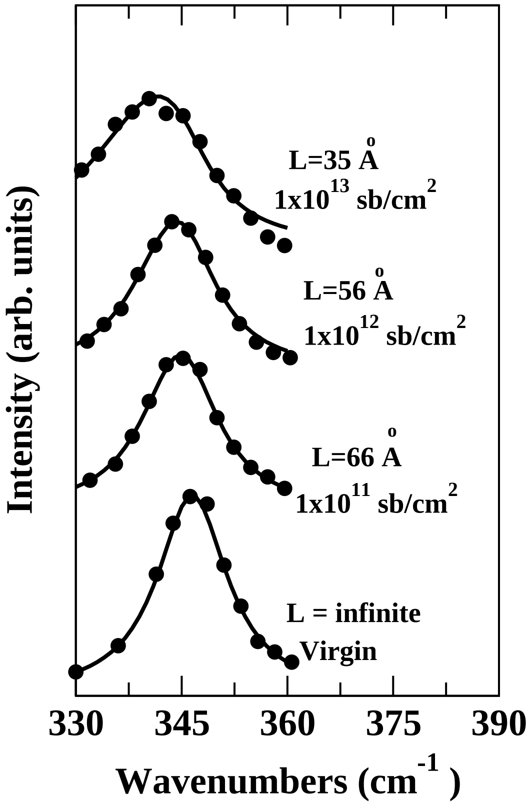

Figure 5.7: Raman spectra of Sb implanted InP(111) at various fluences fitted with PCM; ●: experimental data, –: PCM fit to data. L($\AA$) is the phonon coherence length as determined by the fit to the data. Fitting for the virgin sample is also shown.

stage is only 35 $\AA$. The shifts in the peak positions of Raman spectra can be affected by the residual stress as well as by phonon confinement. The contributions due to the two effects can however be deconvoluted since the stress does not affect the shape of the spectrum whereas the confinement of phonon produces asymmetricity in the raman spectrum. Thus, results after PCM fitting, for the fluences 1×10^{11} $ions/cm^2$ to 1×10^{13} $ions/cm^2$, suggest the presence of nanometer sized undamaged crystalline regions in the as-implanted InP matrix. A coexistence of nanocrystalline structures and amorphous InP matrix takes place at these fluences. For higher fluences, the InP lattice becomes completely amorphous. It is likely that the small amorphous zones inflate in size or some new amorphous zones get created, with increasing fluence, that finally overlap leading to total amorphization of the lattice. In fig. 5.7 we observe a coherence length of 35 Å at 1×10^{13} $ions/cm^2$. At this fluence, LO mode displays an overall shift of 8 cm^{-1} and a width of 20 cm^{-1} (see fig. 5.2). Surprisingly, keV implantation at 1×10^{13} $ions/cm^2$ in InP(100), also leads to a similar coherence length (∼36 Å)[13]. However, shift, in LO mode, was only 1.3 cm^{-1} whereas FWHM was 18 cm^{-1}. For 3 keV Ar ion irradiation of InP(111), (discussed in chapter-3), maximum shift of 2.3 cm^{-1} was observed for LO peak after the fluence of 18×10^{15} $ions/cm^2$. For InP quantum dot (QD) of 35Å, the shifts and FWHM of LO mode are found to be ∼4 cm^{-1} and ∼20 cm^{-1}, respectively [21]. Although the widths of LO mode in the present study as well as for keV implantation [13] or for InP QD [21] are similar, the shifts in all these studies are different (even though the coherence length in all these cases is similar: L∼ 35Å). Varying LO shifts may indicate varying order of associated stresses. After MeV implantation of Sb in Si [2] the coherence length was found to be 330 Å for a fluence of 1×10^{13} $ions/cm^2$. Higher nuclear energy loss, S_n, for Sb in InP (1.9 keV/nm) compared to that in Si (1.2 keV/nm) will be responsible for the smaller nano-crystalline zones in InP at all fluences.

The electron-phonon coupling strength can be estimated by measuring the normalized Raman intensity (I_R) of the 2LO phonon with respect to that of LO phonon. I_R is considered approximately proportional to the electron-LO phonon coupling [20, 33]. We have obtained I_R for virgin InP(111) as well as after implantation at various fluences and have shown them in fig. 5.8. For virgin InP(111) we find I_R of 0.198. The I_R is seen to decrease as the fluence is increased. We observe I_R of 0.175, 0.165 and 0.135 for the fluences of 1×10^{11}, 1×10^{12} and 1×10^{13} $ions/cm^2$, respectively. From the PCM fitting results we had found that the coherence length of the crystalline zones is 66Å at the fluence of 1×10^{11} $ions/cm^2$ (fig. 5.7). It was also observed that as the fluence is increased, the coherence lengths decrease and become 56Å and 35Å for the fluences of 1×10^{12} and 1×10^{13}, respectively. In fig. 5.8 (top axis) we have marked the coherence length, L, as obtained from the fitting results of PCM model (shown in fig. 5.7) at all fluences. Thus, from fig. 5.8 it is observed that the electron- phonon coupling strength of nano-crystalline zones in InP decreases as their coherence length or sizes decrease. This behaviour is similar to the results seen for InP Quantum dots [21]. However, the I_R seen for InP QD were very slightly smaller (0.13 for L=55Å and

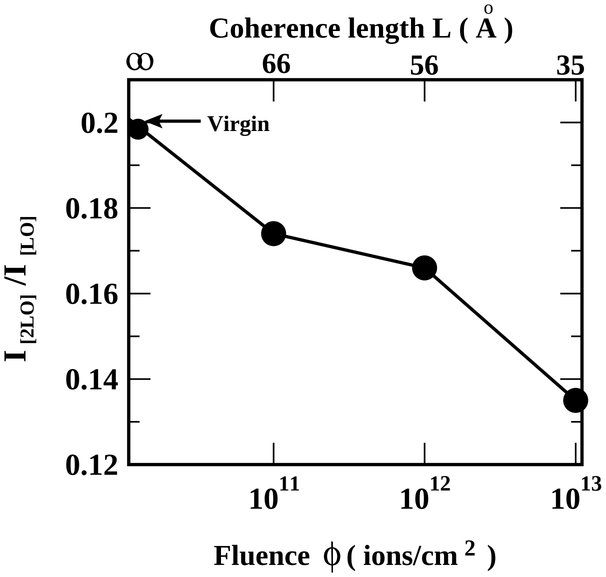

Figure 5.8: Electron Phonon Coupling Strength: Normalized Raman intensity of second-order 2LO phonon with respect to that of first-order LO as a function of ion fluence. Value for the virgin bulk-InP is also shown. The coherence lengths (L), at all fluences, are also marked on the top axis.

0.08 for L=35$\mathring{A}$) than those seen here for nano-crystalline zones created after MeV implantation. In the present study we observe that the electron- phonon coupling, I_R, is largest (=0.2) for the virgin bulk-InP which also has biggest, infinite, coherence length. With the decrease in coherence length, the electron-phonon coupling strength also decreases. The strength of coupling is about 1.5 times weaker in the nano-crystalline zones, of 35$\mathring{A}$ size, than in the bulk -InP. This reduction in coupling is consistent with the increased overlap of electron and hole when there is substantial quantum confinement as also observed for bulk CdSe Quantum dots [20] where a 20 times reduction in coupling strength, compared to bulk solid, was observed for a 45$\mathring{A}$ cluster. Thus, the largest I_R is observed for bulk solid and the lowest I_R for the smallest crystalline zones in the present study after MeV implantation in InP as well as for CdSe clusters[20]. However, surprisingly, for InP quantum dots [21, 33], smallest I_R was observed for the bulk-InP.

5.4 Summary and Conclusion

Structural modifications in InP(111) due to 1.5 MeV implantation of Sb have been characterized using first order and second order Raman spectroscopy. With both Longitudinal Optical (LO) and Transverse Optical (TO) modes allowed for InP(111), we have investigated the evolution of both these modes as a function of fluence. Investigations of both the first and second order Raman modes indicate the presence of tensile stress in the lattice after implantation, which increases with fluence. Results show a coexistence of nano crystalline InP regions and amorphous zones in the lattice. Consequently phonon confinement is observed and Phonon Confinement model (PCM) has been applied here to estimate the coherence length and the size of nano-crystalline zones in InP lattice after implantation. Nano crystalline zones as small as $35\mathring{A}$ have been observed here. A LO phonon-plasmon coupled mode, due to the charge layer in the vicinity of the surface, has also been observed. This coupled mode becomes sharper and more intense with increasing fluence. For high fluences, crystalline to amorphous phase transition has also been observed. First and second order LO modes have been utilized to estimate the the electron-phonon coupling strengths. Electron- Phonon coupling strength in nano-crystalline zones has been estimated and the strength is found to be about 0.135 for the nano- crystalline zones having the coherence length of $35\mathring{A}$. This strength is about 1.5 times smaller than the coupling strength in the bulk-InP. Furthermore, it is observed that the coupling strength reduces as the size of the crystalline regions becomes smaller.

Bibliography

[1] W. K. Chu, J. W. Mayer and M. A. Nicolet, Backscattering Spectrometry (Academic Press, New York, 1978).

[2] S. Dey, C. Roy, A. Pradhan and S. Varma, J. Appl. Phys. **87**, 1110 (2000); S. Dey, G. Kuri, B. Rout and S. Varma, Nucl. Instr. Meth. B **142**, 35 (1998) .

[3] G.K. Mehta, Vacuum **48** (1997) 957.

[4] Dipak Paramanik and Shikha Varma, J. Appl. Phys. **101**, 023528 (2007).

[5] D. Paramanik, A. Pradhan, S. Varma, J. Appl. Phys **99**, 014304 (2006).

[6] L. Artus, R. Cusco, J. Ibanez, N. Blanco, and G.G. Diaz, Phys. Rev. B **60**, 5456 (1999).

[7] L. Artus, R. Cusco, J. Ibanez, J. M. Martin, G. Gonzalez-Diaz, J. Appl. Phys.**82**, 3736 (1997).

[8] I.M. Tiginyanu, A.I. Terletsky, V.V. Ursaki, Solid State Commun. **96**, 789 (1995).

[9] K. Santhakumar, P. Jayavel, R. Kesavamoorthy, P.Magudapathy, K.G.M. Nair, V. Ravichandran, Nucl.Inst. and Meth. B,**194**, 451 (2002).

[10] J. Ibanez, R.Cusco, N. Blanco, G. Gonzalez-Diaz, L. Artus, Nucl.Inst. and Meth. B,**148**, 454 (1999).

[11] R. Cusco, G. Talamas, L. Artus, J. M. Martin, G. Gonzalez-Diaz, J. Appl. Phys.**79**, 3927 (1996).

[12] E. Bedel, G. Landa, R. Carles, J.B. Renucci, J.M. Roquais and P.M. Favennec, J. Appl. Phys. **60**, 1980 (1986).

[13] Soon Jae Yu, Hajime Asahi, Shuichi Emura, Hitoshi Sumida, Shun-ichi Gonda, and Hisao Tanoue, J. Appl. Phys.**66**, 856 (1989).

[14] R. Cusco, J. Ibanez, N. Blanco, and G.G. Diaz, L. Artus, Nucl.Inst. and Meth. B,**132**, 627 (1997).

[15] C.S. Rama Rao, S. Sundaram, R.L. Schmidt, J. Comas, J. Appl. Phys.**54**, 1808 (1983).

[16] Hiroshi Katsumata, Shin-ichiro Uekusa, Hironobu Sai, and Masao Kumagai, Jour. Appl. Phys. **80** (1996) 2383.

[17] P.H. Borcherds, G.F. Alfrey, D.H. Saundersons, and A.D.B. Woods, J. Phys. C: Solid State Phys. **8**, 2022 (1975).

[18] P.H. Borcherds, K. Kune, J. Phys.C: Solid State Phys.**11**, 4145 (1978).

[19] G. Abstreiter, M. Cardona, A. Pinczuk, in *Light Scattering in Solids IV* edited by M. Cardona and G. Guntherodt, Topics in Applied Physics, Vol. 54 (Springer, Verlag Berlin, 1984) and references therein.

[20] A.P. Alivisatos, T.D. Harris, P.J. Carroll, M.L. Steigerwald and L.E. Brus, J. Chem Phys. **90** 3463 (1989).

[21] M.J. Seong, O.I. Micic, A.J. Nozik and A. Mascarenhas, and H.M. Cheong, Appl. Phys. Lett. **82**, 185 (2003).

[22] H.Richter, Z.P.Wang and L.Ley, Solid State Commun. **39**, 625 (1981).

[23] J. P. Biersack and L. G. Haggmark, Nucl. Instr. and Meth. **B174**, 257 (1980). We have used the version SRIM 03.

[24] A. Pinczuk, A.A. Ballman, R.E. Nahory, M.A. Pollack, and J.M. Worlock, J. Vac. Sci. Technol., **16** 1168 (1979).

[25] S.K. Mohanta, R.K. Soni. S. Tripathy and S.J. Chua, Appl. Phys. Lett. **88** 043101 (2006).

[26] X.Huang, F.Ninio, L.J.Brown and S.Prawer, J. Appl. Phys. **77**, 5910 (1995).

[27] K.K. Tiong, P.M. Amirtharaj, F.H. Pollak and D.E. Aspnes, Appl. Phys. Lett. **44**, 122 (1984).

[28] W. Wesch, E. Wendler, T. Bachmann, and O. Herre, Nucl. Instru. Meth. Res. B. **96**, 290 (1995).

[29] H.Wemple, J.C. North, and J.M. Dishman, J. Appl. Phys.**45**, 1578 (1974).

[30] K.J. Nash and M.S. Skolnick, Phys. Rev. Lett.**60**, 863 (1988).

[31] L. Artus, R. Cusco,J.M. Martin, G. Gonzalez-Diaz, Phys. Rev. B.**50**, 11552 (1994).

[32] Z. Sui, P.P. Leong, I.P. Herman, G.S. Higashi, and H. Temkin, Appl. Phys. Lett.**60**, 2086 (1992).

[33] J.J. Shiang, R.H. Risbud and A.P. Alivisatos, J. Chem Phys. **98**, 8432 (1993).

Chapter 6

Summary and Conclusion

The studies presented here have shown that ion irradiation is a powerful technique to modify the InP surfaces. After low energy (3 keV) irradiations, InP surfaces display nano dots on the surface. These self assembled structures are a result of competition between the curvature dependent erosion and diffusion mediated smoothening phenomenon undergoing on the surface during irradiation. Surface behavior thus becomes complex with surface roughness and surface stress varying with fluence, erosion and diffusion of atoms. The MeV implantation also leads to the formation of nanostructures on the InP surfaces. These structures are, however, defect zones created by high energy irradiation.

An introduction to basic concepts on the nano pattern formation and the ion solid interactions is presented in **chapter-1**. Ion beam irradiation facilities and various characterization techniques used in the present studies are described in **chapter-2**.

Chapter-3 presents the formation of nano-patterns on InP(111) surfaces, as a function of ion fluence, after 3 keV Ar ion irradiation. The surface with cloudlike patches, seen after 5 min, transforms into a morphology where isolated and self assembled nano dots, generated by the interplay between the ion induced erosion and the surface relaxation, are seen after 10 min. The size and height distributions of these nano dots depend on the sputtering time. A critical time, t_c, is found. At t_c the size and height of the nano dots become maximum. The amplification of the random amplitudes by the negative surface tension compete with the smoothening processes such as surface diffusion and viscous flow and lead to the formation of nano-dot patterns. During this process the size of dots increases and their size distributions becomes broader leading to an increased roughness of the surface. The dots once formed, coarsen and agglomerate, becoming largest at 40 min. To understand the nature of the surface modifications and to compare these observations with the existing theoretical models, roughness exponent (α) and the growth exponent (β) have been measured using SPM images. Raman scattering results show that surface also experiences a tensile stress which increases with sputtering time but relaxes at t_c, where the surface-amorphization is first observed. This results in the inverse ripening and fragmentation of dots along with the smoothening of InP surface for longer sputtering durations. XPS results demonstrate that keV irradiation leads to an excess of In atoms on the surface that promotes the nucleation of nano dots leading to their self assembled growth. Decrease in In concentration, for longer sputtering durations, causes the breaking of nano dots into smaller structures.

Chapter-4 describes the investigations of the surface modifications and nanoscale structure formation on InP(111) surfaces after 1.5 MeV Sb ion irradiation. The size, height and density of the nano-structure have been studied for various ion fluences ranging from 1×10^{11} - 1×10^{15} $ions/cm^2$. Several nanostructures of sizes smaller than 100 nm and lower than 4 nm have been observed. The surface roughness initially increases up to the Sb fluence of 1×10^{14} $ions/cm^2$. For higher fluences, a decrease in the surface roughness is observed. Power Spectral Density study suggests that diffusion processes are crucially determining the evolution of InP(111) surfaces after MeV implantations. Random distribution of nanostructures for 1×10^{11} $ions/cm^2$ but a non-uniform distribution at higher fluences is observed from the Radial Separation Distribution studies. The scaling exponents: roughness(α) and growth(β) exponents have been determined. For early times, i.e. for fluences lower than 1×10^{14} $ions/cm^2$ a $\beta = 0.25$ has been obtained. For fluences higher than the critical fluence ($1\times10^{14} ions/cm^2$), $\alpha = 0.84$ is obtained. It is further observed that wavelength of the patterns evolves as $\lambda \sim t^{-0.58}$.

Structural modifications in InP(111) due to 1.5 MeV implantation of Sb have been characterized using first order and second order Raman spectroscopy in **chapter-5**. Investigations of both the first and second order Raman modes (TO and LO) indicate the presence of tensile stress in the lattice as well as on the surface after implantation, which increases with fluence up to the critical fluence 1×10^{14} $ions/cm^2$. However, beyond 1×10^{14} $ions/cm^2$ the lattice gets amorphized and the stress gets relaxed. The study shows a coexistence of nano crystalline InP regions and amorphous zones in the lattice at lower fluences. Consequently phonon confinement is observed and phonon confinement model has been applied here to estimate the coherence length and the size of nano-crystalline zones in InP lattice after implantation. Nano crystalline zones as small as $35\AA$ have been observed here. First and second order LO modes have been utilized to estimate the electron-phonon coupling strengths. Electron- Phonon coupling strength in nano-crystalline zones has been estimated and the strength is found to be about 0.135 for the nano- crystalline zones having the coherence length of $35\AA$. This strength is about 1.5 times smaller than the coupling strength in the bulk-InP. Furthermore, it is observed that the coupling strength reduces as the size of the crystalline regions becomes smaller.

In conclusion, the surface morphology that develops, after ion irradiation, strongly depends on the energy of the irradiation. However, although the self assembled structures and their distributions vary with energy, as has been observed in the present study, some salient features are common. For both the low (keV) and the high energy (MeV) irradiations, the surface initially roughens but then smoothens beyond a critical fluence. The critical fluence ($24 \times 10^{15} ions/cm^2$) seen after 3 keV irradiation in the present study, is higher than that seen here after 1.5 MeV irradiation ($1 \times 10^{14} ions/cm^2$). This is expected since the small contribution of S_n at 3 keV, compared to that at 1.5 MeV, will require a higher fluence for the surface amorphization. At the critical fluence, for both the irradiation energies, the surface undergoes c/a transition. This amorphization leads to relaxations and smoothening of the surfaces via decreased strains. The theoretical model based on linear BH equation show that the characteristic wavelength (λ) is independent of fluence. However, both the keV and MeV irradiated surfaces display that this wavelength depends on the ion fluence. The results, thus, suggest that BH model does not describe the surface morphology, seen in the present experiments, completely and the inclusion of non-linear terms, as in the KS theory, may be essential for describing the observed surface evolution. The scaling parameters have been measured for keV and MeV ion irradiated surfaces. The roughness (α) and growth (β) exponents are found to be 0.77 and 0.82, respectively, after keV; and 0.84 and 0.25, respectively, after MeV irradiations. For non-equilibrium film growth, KPZ model suggests α=0.38 and β=0.25. Although the β seen after MeV irradiation is similar to that for thin film growth, values of α, after both keV and MeV irradiations, and value of β after keV irradiations, are much higher that that seen for thin film growth. Moreover the surface roughness, for both the irradiation energies studied here, displays two regions: one below the critical fluence with positive β, and another for larger fluences with the negative β. The theoretical models for non-equilibrium thin film growth or for ion irradiated surfaces, even K-S formalism considering non linear terms, do not show the presence of negative β. These results, thus, suggest that non-linear terms of higher order, than in KS description, may be required to explain the smoothening behavior (i.e. $\beta < 0$) seen for fluences higher than critical fluence, beyond the c/a transition, for the keV and MeV ion irradiated surfaces studied here.